Available online at www.sciencedirect.com
ScienceDirect
Comput. Methods Appl. Mech. Engrg. 294 (2015) 384–427
Computer methods in applied mechanics and engineering
www.elsevier.com/locate/cma

Continuum approach to computational multiscale modeling of propagating fracture

J. Oliver[a,b,*], M. Caicedo[b], E. Roubin[b], A.E. Huespe[b,c], J.A. Hernández[a,b]

[a] E.T.S. d'Enginyers de Camins, Canals i Ports, Technical University of Catalonia (BarcelonaTech), Spain
[b] Centre Internacional de Metodes Numerics en Enyinyeria (CIMNE), Campus Nord UPC, Edifici C-1, c/Jordi Girona 1-3, 08034 Barcelona, Spain
[c] CIMEC-UNL-CONICET, Güemes 3450, Santa Fe, Argentina

Available online 9 July 2015

Abstract

A new approach to two-scale modeling of propagating fracture, based on computational homogenization (FE^2), is presented. The specific features of the approach are: (a) a continuum setting for representation of the fracture at both scales based on the Continuum Strong Discontinuity Approach (CSDA), and (b) the use, for the considered non-smooth (discontinuous) problem, of the same computational homogenization framework than for classical smooth cases. As a key issue, the approach retrieves a characteristic length computed at the lower scale, which is exported to the upper one and used therein as a regularization parameter for a propagating strong discontinuity kinematics. This guarantees the correct transfer of fracture energy between scales and the proper dissipation at the upper scale. Representative simulations show that the resulting formulation provides consistent results, which are objective with respect to size and bias of the upper-scale mesh, and with respect to the size of the lower-scale RVE/failure cell, as well as the capability to model propagating cracks at the upper scale, in combination with crack-path-field and strain injection techniques. The continuum character of the approach confers to the formulation a minimal intrusive character, with respect to standard procedures for multi-scale computational homogenization.

Keywords: Multi-scale; Fracture; Propagating failure; Continuum Strong Discontinuity Approach (CSDA)

1. Introduction

Multi-scale computational modeling of solids, aiming at improving the predictive capabilities of mechanical models accounting for the description of the material at several scales, is a subject of increasing interest. A number of analytical and computational strategies have been developed in the past considering the description of the constitutive material at different scales, [1–14]. In most of them, multiscale description of the material itself

* Corresponding author at: E.T.S. d'Enginyers de Camins, Canals i Ports, Technical University of Catalonia (BarcelonaTech), Spain.
E-mail addresses: xavier.oliver@upc.edu (J. Oliver), mcaicedo@cimne.upc.edu (M. Caicedo), eroubin@cimne.upc.edu (E. Roubin), ahuespe@intec.unl.edu.ar (A.E. Huespe), jhortega@cimne.upc.edu (J.A. Hernández).

http://dx.doi.org/10.1016/j.cma.2015.05.012
0045-7825/

(e.g. computational material homogenization) and consequences and implications, on the overall modeling of the solid, of this specific description (computational multiscale modeling), are not generally considered in an integrated setting. In the context of a two scale (macro scale–micro/meso-scale) problem, computational homogenization of materials (FE^2) is generally regarded as a way of replacing, at the structural-scale, standard stress–strain phenomenological constitutive models equipped with internal variables, accounting for the micro/mesoscopic material morphology, by point wise overall stress–strain evaluations. The overall stresses are then obtained after solving an auxiliary problem, *the homogenization problem*, at the micro/meso-scale, in a manifold, the Representative Volume Element (RVE), endowed with a geometrical description of the material morphology. In turn, this RVE problem relies on some well-established paradigms, typically the classical Hill–Mandel principle [1,14,15] and the strain and stress homogenization concepts. More specifically: in this work we consider as starting point the modern *variational approach to multiscale homogenization* [16,17]. After this, the structural modeling proceeds at the macro/structural scale in a standard manner, with no further modifications.

This weak coupling makes sense for problems involving smooth – linear or nonlinear – material behavior, but the issue seems not to be so clear for non-smooth responses, like *material failure*, – typically fracture, de-cohesion, shear banding etc. – where the involved entities (strains, stresses, displacements) can be non-smooth or even unbounded [18]. For these non-smooth problems, two options emerge:

(a) Use the same homogenization paradigms than for smooth problems, with no specific modification. This approach has been strongly objected: even the existence of the RVE can be questioned, arguing that for fracture cases the material loses the statistical homogeneity [19], or, from another point of view, that the homogenized constitutive model lacks an internal length [20]. A crucial consequence of this issue is the lack of objectivity of the results with respect to the size of the RVE.

(b) Modify the homogenization paradigm towards a specific one for non-smooth problems. Selective RVE domain homogenization methods [21–25] or specific new homogenization paradigms [26,27] are possible ways to retrieve RVE-size objectivity of the results. However, sometimes this is done at the cost of a much higher complexity and intrusion in existing codes and loss of generality of the approach.

In this context, this work presents a new approach for computational multiscale analysis in non-smooth problems with the following features:

1. Extends the homogenization paradigms for smooth problems – typically the Hill–Mandel principle and the stress–strain homogenization procedures – to non-smooth problems, with no fundamental changes.
2. In both scales, a continuum (stress–strain) constitutive relationship is considered, instead of the most common discrete traction/separation-law, this contributing to provide a unified setting for smooth and non-smooth problems. This is achieved by resorting to the well-established Continuum Strong Discontinuity Approach (CSDA) to material failure [28,29,18].
3. As for the multiscale modeling issue, it involves a crucial additional entity: *a characteristic length*, which is point wise obtained from the geometrical features of the failure mechanism developed at the low scale. Introduction of a characteristic length in material homogenization schemes has been claimed as an ineluctable requirement for physical consistency [20], and some approaches to this subject can be found in recent works [30]. As a specific feature of the presented approach, for the non-smooth case this characteristic length is exported, in addition to the homogenized stresses and the tangent constitutive operator, to the macro-scale, and *considered the bandwidth of a propagating strain localization band, at that scale*.
4. Consistently with this characteristic length, a specific computational procedure, based on the *crack-path-field and strain injection techniques*, recently developed by the authors [31], is then used for modeling the onset and propagation of this localization band, at the macro-scale. This ensures the macro-scale mesh-size and micro-scale RVE-size objectivity of the results, and the proper energy dissipation at both scales.

In the remaining of this work a detailed description of the mechanical and computational elements of the proposed approach is presented. In Section 2, the multi-scale framework and the corresponding homogenization procedure, are described, whereas in Section 3 material failure propagation issues are addressed. Section 4 is devoted to present some representative numerical simulations to assess the performance of the proposed approach, and finally, in Section 5, some concluding remarks are stated.

Not to distract the reader's attention on issues that, though being crucial for the completeness of the work and the reproducibility of the results, are not in the core of the proposed approach, some appendices are added at the end of the

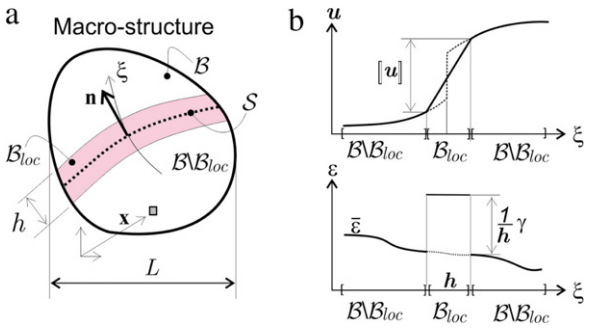

Fig. 1. Macroscopic (structural scale) body $\mathcal{B}$: (a) subdivision in a non-smooth domain, $\mathcal{B}_{loc}(t)$, and a smooth domain $\mathcal{B}\setminus\mathcal{B}_{loc}(t)$, (b) h-regularized, displacement and strain, discontinuity kinematics.

work. Appendix A, details a very simple technique for removing possible spurious unstable modes of the failure cell. Appendix B, refers to the extension to multi-scale problems of the *crack-path-field and strain injection techniques*, developed by the authors in previous works [31] for the purposes of modeling the intra-elemental propagation of strong discontinuities in mono-scale problems.

2. Multi-scale modeling setting

2.1. Macroscopic scale

Let us considered the body, $\mathcal{B}$, at the macroscopic (structural) scale (see Fig. 1). It is assumed that material points, $\mathbf{x}$, of the body belong, at the current time t, to either of the two different subdomains (see Fig. 1):

- Domain $\mathcal{B}\setminus\mathcal{B}_{loc}(t)$: the set of points at the macroscale, exhibiting smooth behavior at the current time. The infinitesimal strain field $\varepsilon(\mathbf{x},t)$ is described, in rate form, as

$$\dot{\boldsymbol{\varepsilon}}(\mathbf{x},t) = (\nabla_{\mathbf{x}}\otimes\dot{\mathbf{u}}(\mathbf{x},t))^{S} \equiv \nabla^{S}\dot{\mathbf{u}}(\mathbf{x},t) \quad \forall\mathbf{x}\in\mathcal{B}\setminus\mathcal{B}_{loc}(t) \tag{1}$$

where $\mathbf{u}(\mathbf{x},t)$ is the macroscale displacement field, t stands for the time or pseudo-time parameter and $(\cdot)^{S}$ stands for the symmetric counterpart of $(\cdot)$.

- Domain $\mathcal{B}_{loc}(t)$: the set of points exhibiting material failure and, therefore, some type of non-smooth behavior at the current time. The strain field at these points is assumed to be captured by a h-regularized strong/weak discontinuity kinematics, h being the width of the corresponding strain localization band (see Fig. 1(b)):

$$\dot{\boldsymbol{\varepsilon}}(\mathbf{x},t) = \dot{\bar{\boldsymbol{\varepsilon}}}(\mathbf{x},t) + \frac{\kappa_{\mathcal{B}_{loc}}(\mathbf{x})}{h}\dot{\boldsymbol{\gamma}}(\mathbf{x},t) = \dot{\bar{\boldsymbol{\varepsilon}}}(\mathbf{x},t) + \delta^{h}_{\mathcal{S}}(\mathbf{x})\dot{\boldsymbol{\gamma}}(\mathbf{x},t) \quad \forall\mathbf{x}\in\mathcal{B}_{loc}(t) \tag{2}$$

where $\bar{\boldsymbol{\varepsilon}}(\mathbf{x},t)$ stands for regular (smooth) counterpart of the strain, $\kappa_{\mathcal{B}_{loc}}$ is a colocation (characteristic) function on $\mathcal{B}_{loc}$ ($\kappa_{\mathcal{B}_{loc}}(\mathbf{x}) = 1\ \forall\mathbf{x}\in\mathcal{B}_{loc}$; $\kappa_{\mathcal{B}_{loc}}(\mathbf{x}) = 0\ \forall\mathbf{x}\notin\mathcal{B}_{loc}$), so that the term $\delta^{h}_{\mathcal{S}}(\mathbf{x})$ becomes a h-regularized Dirac's delta function shifted to the center-line, $\mathcal{S}(t)$ (the macroscopic discontinuity-path at the current time), of band $\mathcal{B}_{loc}(t)$ (see Fig. 1(a)). Thus, in Eq. (2), the term $\delta^{h}_{\mathcal{S}}(\mathbf{x})\dot{\boldsymbol{\gamma}}(\mathbf{x}_{\mathcal{S}},t)$ is the non-smooth (discontinuous and h-regularized) localized counterpart of the strains; a space-discontinuous symmetric, second order tensor for the *weak-discontinuity case*. For the *strong-discontinuity case* – $\boldsymbol{\varepsilon}(\mathbf{x},t)$ stemming from a discontinuous displacement field – it takes the following specific format of a *rank-one tensor*, in terms of the macroscopic displacement jump at $\mathcal{S}(t)$, $\boldsymbol{\beta}(\mathbf{x}_{\mathcal{S}},t)$, and the normal to the discontinuity path, $\mathbf{n}(\mathbf{x}_{\mathcal{S}})$:

$$\begin{cases} \dot{\gamma}(\mathbf{x}_{\mathcal{S}},t) = (\underbrace{\dot{\boldsymbol{\beta}}(\mathbf{x}_{\mathcal{S}},t)}_{\dot{\xi}\mathbf{m}}\otimes\mathbf{n}(\mathbf{x}_{\mathcal{S}}))^{S} = \dot{\xi}(\mathbf{x},t)(\mathbf{m}\otimes\mathbf{n})^{S} \\ \|\mathbf{m}\| = \|\mathbf{n}\| = 1; \quad \left\|\dot{\boldsymbol{\beta}}\right\| = \dot{\xi} \end{cases} \tag{3}$$
$$\Rightarrow \dot{\boldsymbol{\varepsilon}}(\mathbf{x},t) = \dot{\bar{\boldsymbol{\varepsilon}}}(\mathbf{x},t) + \delta^{h}_{\mathcal{S}}(\mathbf{x})\dot{\xi}(\mathbf{x},t)(\mathbf{m}\otimes\mathbf{n})^{S}$$

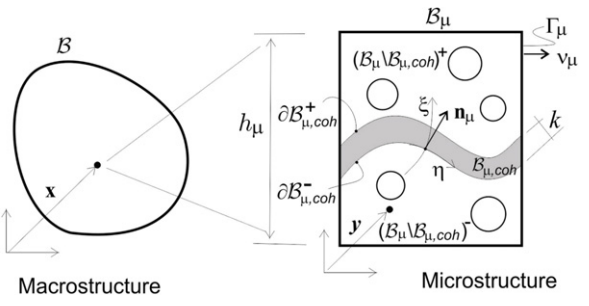

Fig. 2. Multiscale model: failure-cell with cohesive bands.

where notation $(\mathbf{m}\otimes\mathbf{n})^S \equiv \mathbf{m}\otimes^S\mathbf{n} = \frac{1}{2}(\mathbf{m}\otimes\mathbf{n}+\mathbf{n}\otimes\mathbf{m})$ is used to denote the symmetric part of the tensor product $\mathbf{m}\otimes\mathbf{n}$. Transition, for a given material point, $\mathbf{x}$, from the weak discontinuity kinematics, in Eq. (2), to the strong discontinuity kinematics, in Eq. (3), is explained in detail in Section 2.5.

2.2. Microscopic scale

Let us now assume that the non-smooth behavior at the structural scale is produced, in turn, by a non-smooth behavior at the microscale level arising from some type of material failure at this lower scale. Therefore, the next issue is to endow the low-scale model with mechanisms to capture the onset and propagation of this material failure: typically discontinuous micro-displacement fields. For the sake of simplicity, and without prejudice to introduce further, more complex, options, it is considered that the microstructure is able to capture some dominant failure mechanisms of the material. For this purpose, a micro-failure-cell,[1] $\mathcal{B}_\mu(\mathbf{x})$, of typical size h_μ, is considered to exist at every material point $\mathbf{x}\in\mathcal{B}$ (see Fig. 2). It accounts for the material morphology at the lower scale (voids, inclusions etc.) as in regular homogenization procedures, but in addition, it is endowed with a *set of cohesive bands*, $\mathcal{B}_{\mu,coh}\subset\mathcal{B}_\mu$, of very small bandwidth ($k\ll h_\mu$), whose position and other geometric properties (typically the normal $\mathbf{n}_\mu$, see Fig. 2) are predefined. Activation (de-cohesion) at the current time, t, of a number of those bands, defines the current *subset of active bands*, $\mathcal{B}_{\mu,act}(t)\subset\mathcal{B}_{\mu,coh}\subset\mathcal{B}_\mu$ which constitutes the *activated microscopic failure mechanism*, at the current time and for the considered point $\mathbf{x}\in\mathcal{B}$ at the macro-scale.

Remark 2.1. In principle, there is no intrinsic limitation on the number of the cohesive bands at the failure cell. On one hand, their number and spatial position have to be sufficient to capture the dominant material failure mechanisms at the macro-scale, and, on the other hand, the associated computational cost clearly sets a limitation on the number of such bands. Therefore, an appropriated balance of both aspects has to be achieved. In the examples in Section 4, results obtained with relatively crude representations of the material morphology and failure mechanisms at the micro-scale provide a first approach to this issue.

In consequence, the following domains at the microscale are considered (see Fig. 2):

- Domain $\mathcal{B}_\mu\setminus\mathcal{B}_{\mu,coh}$: the set of points, $\mathbf{y}$, out of the cohesive bands. They are imposed to exhibit a smooth behavior described by a *continuum elastic model*, typically:

$$\boldsymbol{\sigma}_\mu(\mathbf{x},\mathbf{y},t) = \boldsymbol{\Sigma}^{elastic}(\boldsymbol{\varepsilon}_\mu) \equiv \boldsymbol{C}_\mu(\mathbf{y}) : \boldsymbol{\varepsilon}_\mu(\mathbf{x},\mathbf{y},t) \quad \forall\mathbf{x}\in\mathcal{B};\ \forall\mathbf{y}\in\mathcal{B}_\mu\setminus\mathcal{B}_{\mu,coh} \tag{4}$$

  where $\boldsymbol{\sigma}_\mu$ and $\boldsymbol{\varepsilon}_\mu$ stand, respectively, for the micro-stresses and micro-strains at the micro-scale point, $\mathbf{y}$, of the failure cell corresponding to the macro-scale point, $\mathbf{x}$, and $\boldsymbol{C}_\mu(\mathbf{y})$ is the micro elastic constitutive tensor.
- Domain $\mathcal{B}_{\mu,coh}$: the set of microscale cohesive bands. As for the material behavior, in this case one has to make a distinction of two cases:
  (a) The failure cell, $\mathcal{B}_\mu(\mathbf{x})$, is associated to a *non-smooth* material point at the macro-scale ($\mathbf{x}\in\mathcal{B}_{loc}(t)$). Without prejudice of using any other inelastic constitutive model, in the remaining of this work an *isotropic continuum*

[1] From now on, sub-index $(\cdot)_\mu$ will denote entities associated to the micro-scale.

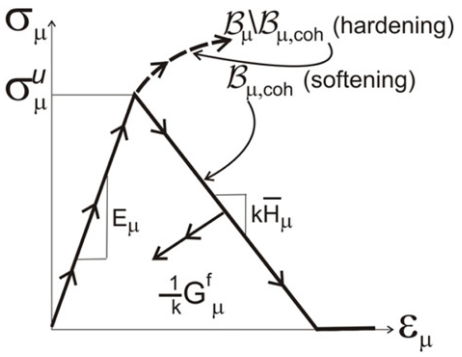

Fig. 3. Isotropic continuum damage model at the microscale (uniaxial version).

Box 2.1.
Isotropic continuum tensile-damage model with strain-softening

$$\boldsymbol{\sigma}_\mu = (1-d_\mu)\boldsymbol{C}_\mu : \boldsymbol{\varepsilon}_\mu = \frac{q_\mu}{r_\mu}\underbrace{\boldsymbol{C}_\mu : \boldsymbol{\varepsilon}_\mu}_{\overline{\boldsymbol{\sigma}}_\mu};$$

$$d_\mu(r_\mu) = 1 - (q_\mu(r_\mu)/r_\mu) \geq 0;$$

$$\dot{r}_\mu = \lambda; \qquad r_\mu|_{t=0} = r_0 = \sigma_\mu^u/\sqrt{E_\mu};$$

$$\begin{cases} \dot{q}_\mu = k\overline{H}(r_\mu)\dot{r}_\mu; & q_\mu \geq 0; \quad q|_{t=0} = r_0 \\ k = \textit{regularization parameter (bandwidth of localized strains)} \end{cases}$$

$$\underbrace{\overline{H}(r_\mu)}_{\substack{\textit{internal}\\ \textit{softening}\\ \textit{modulus}}} = \begin{cases} -\dfrac{r_0^2}{2G_\mu^f}; & \textit{bilinear softening} \\ -r_0^2/G_\mu^f \exp\left(\dfrac{kr_0}{G_\mu^f}(r_\mu - r_0)\right); & \textit{exponential softening} \end{cases}$$

$$\begin{cases} g(\boldsymbol{\varepsilon}_\mu, r_\mu) \equiv \sqrt{\overline{\boldsymbol{\sigma}}_\mu^+ : \boldsymbol{\varepsilon}_\mu} - r_\mu; \qquad \overline{\boldsymbol{\sigma}}_\mu^+ = \displaystyle\sum_{i=1}^{3} \langle \overline{\sigma}_{\mu,i} \rangle \, \mathbf{e}_i \otimes \mathbf{e}_i \\ \overline{\sigma}_{\mu,i} \rightarrow \textit{principal stress ``i''} \\ \mathbf{e}_i \rightarrow \textit{principal direction ``i''} \end{cases}$$

$$\dot{\lambda} \geq 0; \quad g \leq 0; \quad \dot{\lambda} g = 0; \quad \begin{matrix} \textit{Karush–Kuhn–Tucker} \\ \textit{(loading/unloading) conditions} \end{matrix}$$

Material parameters: ultimate stress: σ_μ^u; Young's modulus E_μ, Poisson ratio, ν_μ, fracture energy: G_μ^f.
$\overline{\boldsymbol{\sigma}}_\mu^+$ is the positive part of the microscopic effective stress, d_μ is the damage variable and r_μ and q_μ are, respectively, the strain-like and stress-like internal variables.

damage model, exhibiting k-*regularized strain softening inelasticity* only for tensile stresses – *tensile-damage continuum damage model* [32] – will be considered (see also references [33] and [34]). It reads:

$$\boldsymbol{\sigma}_\mu(\mathbf{x},\mathbf{y},t) = \boldsymbol{\Sigma}^{inelastic}(\boldsymbol{\varepsilon}_\mu, r_\mu) \equiv (1 - d_\mu(r_\mu(\mathbf{y},t)))\, \boldsymbol{C}_\mu : \boldsymbol{\varepsilon}_\mu(\mathbf{x},\mathbf{y},t)$$
$$\mathbf{x} \in \mathcal{B}_{loc}(t), \forall \mathbf{y} \in \mathcal{B}_{\mu,coh} \tag{5}$$

where $d_\mu \in [0,1]$ is the, scalar, damage variable whose evolution is described in terms of the internal variable r_μ. More details about the model are given in Box 2.1 (see Fig. 3).

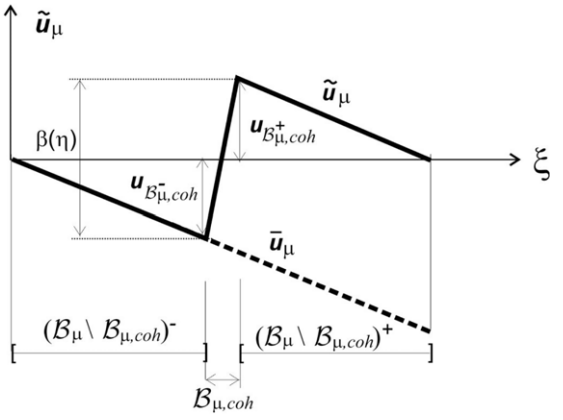

Fig. 4. Micro-displacement fluctuation fields.

(b) The failure cell, $\mathcal{B}_\mu(\mathbf{x})$, is associated to a *smooth* material point at the macro-scale, $(\mathbf{x} \in \mathcal{B} \setminus \mathcal{B}_{loc}(t))$. In this case, the inelastic model, in Eq. (5) is enforced to behave instantaneously elastically at the cohesive bands domain, $\mathcal{B}_{\mu,coh}$, i.e.:

$$\begin{aligned} &\boldsymbol{\sigma}_\mu(\mathbf{x},\mathbf{y},t) = \Sigma^{elastic}_{inst}(\boldsymbol{\varepsilon}_\mu) = \boldsymbol{C}^{elastic}_{inst} : \boldsymbol{\varepsilon}_\mu(\mathbf{x},\mathbf{y},t) \\ &\boldsymbol{C}^{elastic}_{inst} = (1-d_\mu)\,\boldsymbol{C}_\mu \quad \text{with } \dot{d}_\mu = 0 \\ &\forall \mathbf{x} \in \mathcal{B} \setminus \mathcal{B}_{loc}(t); \quad \forall \mathbf{y} \in \mathcal{B}_{\mu,coh}. \end{aligned} \tag{6}$$

Remark 2.2. Notice that, according to the previous setting, *the same RVE morphology is considered at all* $\mathcal{B}_\mu(\mathbf{x})$, both for $\mathbf{x} \in \mathcal{B}_{loc}(t)$ (failure cell) or $\mathbf{x} \in \mathcal{B} \setminus \mathcal{B}_{loc}(t)$, the only difference being the considered constitutive behavior at the cohesive bands, $\mathcal{B}_{\mu,coh}$, defined in Eqs. (5) and (6).

Let us now consider the micro displacement field, $\mathbf{u}_\mu$, at the cell described as

$$\mathbf{u}_\mu(\mathbf{x},\mathbf{y},t) = \mathbf{u}(\mathbf{x},t) + \boldsymbol{\varepsilon}(\mathbf{x},t)\cdot\mathbf{y} + \tilde{\mathbf{u}}_\mu(\mathbf{y},t) \tag{7}$$

where $\mathbf{u}(\mathbf{x},t)$ and $\boldsymbol{\varepsilon}(\mathbf{x},t)$ are, respectively, the macroscale displacement and strain fields at point $\mathbf{x}$ and $\tilde{\mathbf{u}}_\mu$ the microscale displacement fluctuations. Considering a local coordinate system (ξ,η) aligned with the domain $\mathcal{B}_{\mu,coh}$ (see Fig. 2), the *smooth* part of the micro-fluctuation field, $\bar{\mathbf{u}}_\mu$, is defined as:

$$\bar{\mathbf{u}}_\mu(\xi,\eta,t) = \tilde{\mathbf{u}}_\mu(\xi,\eta,t) - \mathcal{H}_{\mathcal{B}_{\mu,coh}}(\xi)\,\boldsymbol{\beta}_\mu(\eta,t) \qquad \text{(a)}$$

$$\mathcal{H}_{\mathcal{B}_{\mu,coh}}(\xi) = \begin{cases} 0 & \forall \mathbf{y} \in (\mathcal{B} \setminus \mathcal{B}_{\mu,coh})^- \\ \dfrac{\xi}{k} & \forall \mathbf{y} \in \mathcal{B}_{\mu,coh} \\ 1 & \forall \mathbf{y} \in (\mathcal{B} \setminus \mathcal{B}_{\mu,coh})^+ \end{cases} \qquad \text{(b)} \tag{8}$$

$$\boldsymbol{\beta}_\mu(\eta(\mathbf{y}),t)\big|_{\mathbf{y}\in\mathcal{B}_{\mu,coh}} \equiv [\![\tilde{\mathbf{u}}_\mu(\xi,\eta,t)]\!]^+_- \qquad \text{(c)}$$

where $\mathcal{H}_{\mathcal{B}_{\mu,coh}}(\xi)$ is the k-regularized Heaviside function shifted to $\mathcal{B}_{\mu,coh}$, and $\boldsymbol{\beta}_\mu(\xi,\eta)$ is a (smooth) function arbitrarily defined excepting for the restriction in Eq. (8)(c).

Notation. $[\![(\cdot)(\xi,\eta)]\!]^+_- \equiv (\cdot)(\xi,\eta)|_{\xi=k} - (\cdot)(\xi,\eta)|_{\xi=0}$ stands for the *apparent jump* of $(\cdot)(\xi,\eta)$ between both sides of the cohesive band. From Eqs. (8) it turns out,

$$[\![\bar{\mathbf{u}}_\mu]\!]^+_- = [\![\tilde{\mathbf{u}}_\mu]\!]^+_- - \underbrace{[\![\mathcal{H}_{\mathcal{B}_{\mu,coh}}]\!]^+_-}_{=1}[\![\tilde{\mathbf{u}}_\mu]\!]^+_- = \mathbf{0} \tag{9}$$

and, therefore, function $\bar{\mathbf{u}}_\mu$ in Eq. (8) is smooth. Finally, from Eq. (8)(a),

$$\tilde{\mathbf{u}}_\mu(\mathbf{y},t) = \underbrace{\bar{\mathbf{u}}_\mu(\mathbf{y},t)}_{smooth} + \mathcal{H}_{\mathcal{B}_{\mu,k}}(\mathbf{y})\,\boldsymbol{\beta}_\mu(\mathbf{y},t) \tag{10}$$

(See a sketch in Fig. 4.) Eq. (10) constitutes the displacement counterpart of a k-regularized strong discontinuity kinematics [28], and proves that the cohesive bands-approach, herein proposed for the description of material failure at the microstructure, is consistent with consideration of a k-regularized strong discontinuity at the cohesive domain $\mathcal{B}_{\mu,coh}$.

In this context, one can resort to the well-established connection of the continuum modeling of material failure – based on stress–strain constitutive equations equipped with strain softening – and the discrete cohesive fracture mechanics, established in the Continuum Strong Discontinuity Approach (CSDA) to material failure [35]. *This states the equivalence, in the limit $k \to 0$, of the proposed approach and the one based on cohesive lines endowed with traction–separation laws* [36].
From Eq. (10) one obtains,

$$\begin{aligned} \boldsymbol{\nabla}^S \tilde{\mathbf{u}}_\mu(\mathbf{y},t) &= \boldsymbol{\nabla}^S \bar{\mathbf{u}}_\mu(\mathbf{y},t) + \mathcal{H}_{\mathcal{B}_{\mu,k}}\, \boldsymbol{\nabla}^S \boldsymbol{\beta}_\mu(\mathbf{y},t) + \delta^k_{\mathcal{S}_\mu}(\boldsymbol{\beta}_\mu \otimes \mathbf{n}_\mu)^S(\mathbf{y}_{\mathcal{S}_\mu},t) \\ &= \underbrace{\bar{\boldsymbol{\varepsilon}}_\mu(\mathbf{y},t)}_{(bounded)} + \underbrace{\delta^k_{\mathcal{S}_\mu}(\mathbf{y},t)\,(\boldsymbol{\beta}_\mu \otimes \mathbf{n}_\mu)^S(\mathbf{y}_{\mathcal{S}_\mu},t)}_{(unbounded)} \qquad (a) \end{aligned} \tag{11}$$

$$\bar{\boldsymbol{\varepsilon}}_\mu(\mathbf{y},t) = \boldsymbol{\nabla}^S \bar{\mathbf{u}}_\mu(\mathbf{y},t) + \mathcal{H}_{\mathcal{B}_{\mu,k}}\, \boldsymbol{\nabla}^S \boldsymbol{\beta}_\mu(\mathbf{y},t) \qquad (b)$$

$$\delta^k_{\mathcal{S}_\mu}(\mathbf{y},t) = \frac{1}{k}\, \kappa_{\mathcal{B}_{\mu,coh}}(\mathbf{y},t) \qquad (c)$$

where $\kappa_{\mathcal{B}_{\mu,coh}}(\mathbf{y})$ is the characteristic (colocation) function in Eq. (2) so that $\delta^k_{\mathcal{S}_\mu}(\mathbf{y},t)$ becomes a k-regularized Dirac's delta function placed at the center line, $\mathcal{S}_\mu$, of $\mathcal{B}_{\mu,coh}$. From Eqs. (7) and (11), the micro-strains $\boldsymbol{\varepsilon}_\mu$ can be written in terms of the macro-strains, $\boldsymbol{\varepsilon}(\mathbf{x},t)$, and the micro-fluctuations, $\tilde{\mathbf{u}}_\mu(\mathbf{y},t)$, as follows[2]:

$$\boldsymbol{\varepsilon}_\mu(\mathbf{x},\mathbf{y}) = \boldsymbol{\varepsilon}(\mathbf{x}) + \nabla^s \tilde{\mathbf{u}}_\mu(\mathbf{y}) = \underbrace{\boldsymbol{\varepsilon}(\mathbf{x}) + \bar{\boldsymbol{\varepsilon}}_\mu(\mathbf{y})}_{(bounded)} + \underbrace{\delta^k_{\mathcal{S}_\mu}\,(\boldsymbol{\beta}_\mu \otimes \mathbf{n}_\mu)^S(\mathbf{y})}_{(unbounded)}\,. \tag{12}$$

Eq. (12) displays the classical format of a strain field in a k-regularized strong discontinuity kinematics, where the second term at the right-hand side becomes unbounded in the limit $k \to 0$.

2.3. Homogenization approach

At this point, the RVE/failure-cell homogenization setting is tackled. It has to be emphasized that, in the proposed approach, *the homogenization setting is the same for smooth, $\mathbf{x} \in \mathcal{B} \setminus \mathcal{B}_{loc}(t)$, and non-smooth, $\mathbf{x} \in \mathcal{B}_{loc}(t)$*, material points of the macroscale and it *coincides with the one considered in the variational homogenization approach in smooth settings* [16]. Therefore, it relies on the following paradigms:

1. *Micro-strain homogenization.*
   According to this, the average value, over $\mathcal{B}_\mu$, of the micro-strains, $\boldsymbol{\varepsilon}_\mu(\mathbf{x},\mathbf{y})$, in Eq. (12) has to be equal to the macro strains, $\boldsymbol{\varepsilon}(\mathbf{x})$ i.e.

$$\boldsymbol{\varepsilon}(\mathbf{x}) = \frac{1}{\Omega_\mu} \int_{\mathcal{B}_\mu(\mathbf{x})} \boldsymbol{\varepsilon}_\mu(\mathbf{x},\mathbf{y})\, d\mathcal{B} \tag{13}$$

   were $\Omega_\mu = meas(\mathcal{B}_\mu)$ stands for the area/volume of the failure cell. Replacing Eq. (12) into (13) results in:

$$\boldsymbol{\varepsilon}(\mathbf{x}) = \boldsymbol{\varepsilon}(\mathbf{x}) + \frac{1}{\Omega_\mu} \int_{\mathcal{B}_\mu(\mathbf{x})} \nabla^s \tilde{\mathbf{u}}_\mu(\mathbf{y})\, d\mathcal{B} \tag{14}$$

   which is satisfied if:

$$\int_{\mathcal{B}_\mu(\mathbf{x})} \nabla^s \tilde{\mathbf{u}}_\mu(\mathbf{y})\, d\mathcal{B} = \int_{\Gamma_\mu(\mathbf{x})} (\tilde{\mathbf{u}}_\mu(\mathbf{y}) \otimes \boldsymbol{\nu}_\mu(\mathbf{y}))^S\, d\Gamma = \mathbf{0} \tag{15}$$

[2] From now on, dependence on time, t, will be omitted excepting when strictly necessary.

where $\mathbf{v}_\mu(\mathbf{y})$ stands for the outward normal to the failure cell, and $\Gamma_\mu \equiv \partial\mathcal{B}_\mu$ is its boundary (see Fig. 2). Thus, we define *the space, $\mathcal{V}_\mu$, of kinematically admissible micro-displacement fluctuations*, as

$$\mathcal{V}_\mu = \left\{ \tilde{\mathbf{u}}_\mu \,\middle|\, \int_{\Gamma_\mu} (\tilde{\mathbf{u}}_\mu \otimes \mathbf{v}_\mu)^S d\Gamma = \mathbf{0} \right\}. \tag{16}$$

Notice that the boundary conditions in Eq. (16) *coincide* exactly, for the proposed non-smooth setting, *with the ones considered in the variational homogenization approach* [16] in smooth settings, and termed *minimal kinematic constraint conditions*.

2. *Hill–Mandel variational principle*.

The balance of the macroscopic and microscopic stress power reads

$$\begin{aligned} \boldsymbol{\sigma}(\mathbf{x}) : \dot{\boldsymbol{\varepsilon}}(\mathbf{x}) &= \frac{1}{\Omega_\mu} \int_{\mathcal{B}_\mu(\mathbf{x})} \boldsymbol{\sigma}_\mu(\mathbf{x},\mathbf{y}) : \dot{\boldsymbol{\varepsilon}}_\mu(\mathbf{x},\mathbf{y}) d\mathcal{B} = \\ &= \frac{1}{\Omega_\mu} \int_{\mathcal{B}_\mu(\mathbf{x})} \boldsymbol{\sigma}_\mu : (\dot{\boldsymbol{\varepsilon}}(\mathbf{x}) + \boldsymbol{\nabla}^S \dot{\tilde{\mathbf{u}}}_\mu(\mathbf{y})) d\mathcal{B}; \quad \forall \dot{\boldsymbol{\varepsilon}},\ \dot{\tilde{\mathbf{u}}}_\mu \in \mathcal{V}_\mu \end{aligned} \tag{17}$$

which, for arbitrary variations $\dot{\boldsymbol{\varepsilon}} \neq \mathbf{0};\ \dot{\tilde{\mathbf{u}}}_\mu \equiv \mathbf{0}$ yields

$$\boldsymbol{\sigma}(\mathbf{x}) = \frac{1}{\Omega_\mu} \int_{\mathcal{B}_\mu(\mathbf{x})} \boldsymbol{\sigma}_\mu(\mathbf{x},\mathbf{y}) d\mathcal{B} \tag{18}$$

and, for arbitrary variations of $\dot{\boldsymbol{\varepsilon}} \equiv \mathbf{0};\ \dot{\tilde{\mathbf{u}}}_\mu \neq \mathbf{0}$, leads to the self-equilibrated stress equation in variational form:

$$\int_{\mathcal{B}_\mu} \boldsymbol{\nabla}^S \delta\tilde{\mathbf{u}}_\mu : \boldsymbol{\sigma}_\mu(\boldsymbol{\varepsilon} + \boldsymbol{\nabla}^S \tilde{\mathbf{u}}_\mu) d\mathcal{B} = \mathbf{0}; \quad \forall\, \delta\tilde{\mathbf{u}}_\mu \in \mathcal{V}_\mu. \tag{19}$$

In the context of a finite element approximation, Eq. (16) is solved as

$$\int_{\mathcal{B}_\mu} \mathbf{B}^T \boldsymbol{\sigma}_\mu(\boldsymbol{\varepsilon} + \mathbf{B}\tilde{\mathbf{d}}_\mu) d\mathcal{B} = \mathbf{0} \tag{20}$$

where $\mathbf{B}(\mathbf{y})$ is the classical deformation matrix [37] and $\tilde{\mathbf{d}}_\mu$ are the nodal values of the fluctuations, compatible with the boundary condition in Eq. (16).

Again, it should be noticed that Eqs. (18)–(20) *have the same format than for purely smooth cases*.

2.4. Theoretical "a priori" analysis of the resulting homogenized constitutive model at the macroscale

Let us now perform a theoretical analysis by examining the consequences of applying the *homogenization procedures*, based on the Hill–Mandel principle, to the totality of the failure cell, $\mathcal{B}_\mu$ (see Eqs. (13)–(19), when regularized strong discontinuities are present at the micro-scale being captured by the cohesive bands $\mathcal{B}_{\mu,coh}$, as displayed in Eqs. (12)). It is precisely in this feature (application of the homogenization in the complete domain of the failure cell) that the proposed approach differs from other approaches, as the one in [38].

Let us consider the failure cell displayed in Fig. 5. For the sake of generality, we will consider the cell composed of a matrix and inclusions (or voids), in addition to a number of cohesive bands defining the set $\mathcal{B}_{\mu,coh}$. Among them, there are n_{active} cohesive bands $\mathcal{B}^{(i)}_{\mu,act};\ i = 1 \ldots n_{active}$, which are in an inelastic softening state, defining a specific failure mode, $\mathcal{B}_{\mu,act} \subset \mathcal{B}_{\mu,coh}$, at the micro-cell.[3] Let us also denote by $\mathcal{S}^{(i)}_\mu$ the midline in the cohesive band i (see Fig. 5).

Therefore, it is fulfilled

$$\mathcal{B}_{\mu,act} = \bigcup_{i=1}^{i=n_{active}} \mathcal{B}^{(i)}_{\mu,act}; \qquad \mathcal{S}_\mu = \bigcup_{i=1}^{i=n_{active}} \mathcal{S}^{(i)}_\mu \tag{21}$$

[3] The remaining cohesive bands are discarded for the purposes of this analysis.

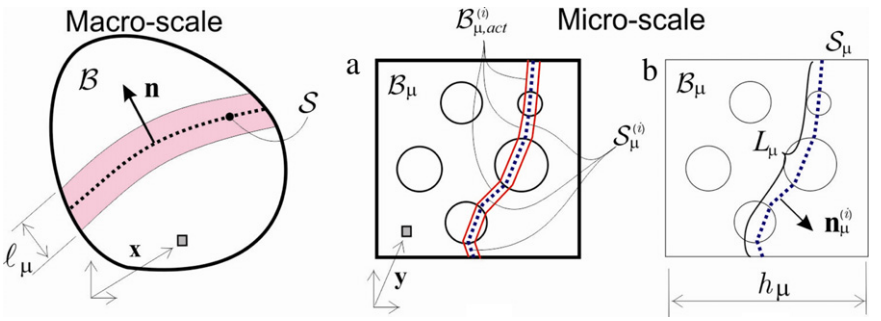

Fig. 5. Multiscale model: (a) failure cell with inclusions and cohesive bands; (b) geometrical characterization of the failure mode at the microscale.

where $\mathcal{S}_\mu$ can be regarded as the active failure/crack path at the micro-scale. From Eqs. (10) and (11), one can write

$$\tilde{\mathbf{u}}_\mu(\mathbf{y}) = \underbrace{\bar{\mathbf{u}}_\mu(\mathbf{y})}_{smooth} + \mathcal{H}_{\mathcal{B}_{\mu,k}}(\mathbf{y})\,\boldsymbol{\beta}_\mu(\mathbf{y}) \qquad (a)$$

$$\nabla^s \tilde{\mathbf{u}}_\mu(\mathbf{y}) = \underbrace{\bar{\boldsymbol{\varepsilon}}_\mu(\mathbf{y})}_{(bounded)} + \underbrace{\delta^k_{\mathcal{S}_\mu}(\boldsymbol{\beta}_\mu \otimes \mathbf{n}_\mu)^S(\mathbf{y})}_{(unbounded)}. \qquad (b) \tag{22}$$

In this context, the following lemma can be stated:

Lemma.

$$\int_{\mathcal{B}_\mu} \bar{\boldsymbol{\varepsilon}}_\mu(\mathbf{x},\mathbf{y})\,d\mathcal{B}_\mu = -\int_{\mathcal{S}_\mu} (\boldsymbol{\beta}_\mu \otimes \mathbf{n}_\mu)^S(\mathbf{y})\,d\mathcal{S}. \tag{23}$$

Proof. Replacement of Eq. (22) into Eq. (15) yields,

$$\int_{\mathcal{B}_\mu} \nabla^s \tilde{\mathbf{u}}_\mu(\mathbf{y})\,d\mathcal{B} = \mathbf{0}$$

$$\Rightarrow \int_{\mathcal{B}_\mu} \bar{\boldsymbol{\varepsilon}}_\mu(\mathbf{y})\,d\mathcal{B} + \int_{\mathcal{B}_\mu} \delta^k_{\mathcal{S}_\mu}(\boldsymbol{\beta}_\mu \otimes \mathbf{n}_\mu)^S(\mathbf{y})\,d\mathcal{B} =$$

$$= \int_{\mathcal{B}_\mu} \bar{\boldsymbol{\varepsilon}}_\mu(\mathbf{y})\,d\mathcal{B} + \int_{\mathcal{S}_\mu} (\boldsymbol{\beta}_\mu \otimes \mathbf{n}_\mu)^S(\mathbf{y})\,d\mathcal{S} = \mathbf{0} \tag{24}$$

where condition, in the limit ($k \to 0$),

$$\int_{\mathcal{B}_{\mu,coh}} \delta^k_{\mathcal{S}_\mu}(\cdot)(\mathbf{y})\,d\mathcal{B} \approx \int_{\mathcal{S}_\mu} (\cdot)(\mathbf{y})\,d\mathcal{S} \tag{25}$$

for sufficient regular functions, $(\cdot)(\mathbf{y})$ [39], has been considered. Eq. (24) proofs trivially Lemma (23).

Let us now compute the rate of homogenized stresses in Eq. (18), in the limit $k \to 0$ as

$$\dot{\boldsymbol{\sigma}}(\mathbf{x}) = \frac{1}{\Omega_\mu}\int_{\mathcal{B}_\mu} \dot{\boldsymbol{\sigma}}_\mu d\mathcal{B} = \frac{1}{\Omega_\mu}\left[\int_{\mathcal{B}_\mu \setminus \mathcal{B}_{\mu,coh}} \dot{\boldsymbol{\sigma}}_\mu d\mathcal{B} + \underbrace{\int_{\mathcal{B}_{\mu,coh}} \dot{\boldsymbol{\sigma}}_\mu d\mathcal{B}}_{=0 \text{ as } k\to 0}\right]$$

$$= \frac{1}{\Omega_\mu}\int_{\mathcal{B}_\mu \setminus \mathcal{B}_{\mu,coh}} \boldsymbol{C}_\mu : \dot{\boldsymbol{\varepsilon}}_\mu d\mathcal{B}. \tag{26}$$

In Eq. (26), the integral on the domain $\mathcal{B}_{\mu,coh}$ is neglected since its kernel, $\dot{\boldsymbol{\sigma}}_\mu$, is bounded whereas the measure of the integration domain tends to zero as $k \to 0$ (see Fig. 2). In addition, the elastic constitutive model in $\mathcal{B}_\mu \setminus \mathcal{B}_{\mu,coh}$ (see Eq. (4)) has been considered.

Now inserting Eq. (12), for $\mathbf{y} \in \mathcal{B}_\mu \setminus \mathcal{B}_{\mu,coh}$, into Eq. (26) yields

$$\dot{\boldsymbol{\sigma}}(\mathbf{x},t) \simeq \frac{1}{\Omega_\mu}\int_{\mathcal{B}_\mu\setminus\mathcal{B}_{\mu,coh}} \underbrace{\boldsymbol{C}_\mu : (\dot{\boldsymbol{\varepsilon}} + \dot{\tilde{\boldsymbol{\varepsilon}}}_\mu)}_{bounded}\, d\mathcal{B} \overset{k\to 0}{\simeq} \frac{1}{\Omega_\mu}\int_{\mathcal{B}_\mu} \boldsymbol{C}_\mu(\mathbf{y}) : (\dot{\boldsymbol{\varepsilon}}(\mathbf{x}) + \dot{\tilde{\boldsymbol{\varepsilon}}}_\mu(\mathbf{x},\mathbf{y}))d\mathcal{B} \tag{27}$$

where, again, the smooth character of the smooth strains $\dot{\boldsymbol{\varepsilon}}$ and $\dot{\tilde{\boldsymbol{\varepsilon}}}$ has been considered. Eq. (27) can be rephrased in terms of the *average value of the micro-elastic constitutive tensor*, $\overline{\boldsymbol{\mathcal{C}}}$, as:

$$\begin{aligned}
\dot{\boldsymbol{\sigma}}(\mathbf{x},t) &= \underbrace{\frac{1}{\Omega_\mu}\int_{\mathcal{B}_\mu} \boldsymbol{C}_\mu(\mathbf{y})d\mathcal{B}}_{\overline{\boldsymbol{\mathcal{C}}}} : \dot{\boldsymbol{\varepsilon}}(\mathbf{x}) + \frac{1}{\Omega_\mu}\int_{\mathcal{B}_\mu} \boldsymbol{C}_\mu(\mathbf{y}) : \dot{\tilde{\boldsymbol{\varepsilon}}}_\mu(\mathbf{x},\mathbf{y})\, d\mathcal{B} \\
&= \overline{\boldsymbol{\mathcal{C}}} : \dot{\boldsymbol{\varepsilon}} + \frac{1}{\Omega_\mu}\int_{\mathcal{B}_\mu} \overline{\boldsymbol{\mathcal{C}}} : \dot{\tilde{\boldsymbol{\varepsilon}}}_\mu d\mathcal{B} + \frac{1}{\Omega_\mu}\int_{\mathcal{B}_\mu} (\boldsymbol{C}_\mu - \overline{\boldsymbol{\mathcal{C}}}) : \dot{\tilde{\boldsymbol{\varepsilon}}}_\mu\, d\mathcal{B} \qquad \text{(a)} \\
\overline{\boldsymbol{\mathcal{C}}} &\equiv \frac{1}{\Omega_\mu}\int_{\mathcal{B}_\mu} \boldsymbol{C}_\mu(\mathbf{y})d\mathcal{B}. \qquad \text{(b)}
\end{aligned} \tag{28}$$

Now, replacing Eq. (23) into Eq. (28) yields,

$$\dot{\boldsymbol{\sigma}}(\mathbf{x},t) = \overline{\boldsymbol{\mathcal{C}}} : \dot{\boldsymbol{\varepsilon}} - \overline{\boldsymbol{\mathcal{C}}} : \underbrace{\frac{1}{\Omega_\mu}\int_{\mathcal{S}_\mu} (\dot{\boldsymbol{\beta}}_\mu \otimes \mathbf{n}_\mu)^S\, d\mathcal{S}}_{=L_\mu(\overline{\dot{\boldsymbol{\beta}}_\mu \otimes^s \mathbf{n}_\mu})_{\mathcal{S}_\mu}} + \underbrace{\frac{1}{\Omega_\mu}\int_{\mathcal{B}_\mu} (\boldsymbol{C}_\mu - \overline{\boldsymbol{\mathcal{C}}}) : \dot{\tilde{\boldsymbol{\varepsilon}}}_\mu d\mathcal{B}}_{\equiv \overline{\boldsymbol{\mathcal{C}}}:\dot{\boldsymbol{\chi}}(\mathbf{x},t)} \tag{29}$$

where $L_\mu = |\mathcal{S}_\mu|$ is the measure (length in 2D, area in 3D) of $\mathcal{S}_\mu$ and $\overline{(\cdot)}_{\mathcal{S}_\mu}$ stands for the average value of $(\cdot)$ in the activated macroscopic failure mechanism along the crack path $\mathcal{S}_\mu$.
Then, Eq. (29) can be rephrased giving rise to the homogenized constitutive model in Box 2.2.

Box 2.2.
Homogenized constitutive model at the macro-scale

$$\begin{cases} \text{homogenized} \\ \text{constitutive} \\ \text{equation (rate form)} \end{cases} \rightarrow \begin{cases} \dot{\boldsymbol{\sigma}}(\mathbf{x},t) = \overline{\boldsymbol{\mathcal{C}}} : \dot{\boldsymbol{\varepsilon}}(\mathbf{x},t) + \overline{\boldsymbol{\mathcal{C}}} : \dot{\boldsymbol{\chi}}(\mathbf{x},t) \\ \quad = \boldsymbol{\mathcal{C}}^{tang}_{hom}(\boldsymbol{\varepsilon}) : \dot{\boldsymbol{\varepsilon}}(\mathbf{x},t) \end{cases} \qquad \text{(a)}$$

$$\begin{cases} \text{averaged elastic} \\ \text{constitutive} \\ \text{tensor} \end{cases} \rightarrow \quad \overline{\boldsymbol{\mathcal{C}}} \equiv \frac{1}{\Omega_\mu}\int_{\mathcal{B}_\mu} \boldsymbol{C}_\mu(\mathbf{y})d\mathcal{B} \qquad \text{(b)}$$

$$\text{smooth internal strain} \rightarrow \begin{cases} \dot{\boldsymbol{\chi}}(\mathbf{x},t) = \dfrac{1}{\Omega_\mu}\displaystyle\int_{\mathcal{B}_\mu} (\overline{\boldsymbol{\mathcal{C}}}^{-1} : \boldsymbol{C}_\mu - \mathbf{I}) : \underbrace{\dot{\tilde{\boldsymbol{\varepsilon}}}_\mu(\tilde{\mathbf{u}}_\mu)}_{=\mathcal{A}(\mathbf{y},\boldsymbol{\varepsilon}):\dot{\boldsymbol{\varepsilon}}}\, d\mathcal{B} \\ = \underbrace{\dfrac{1}{\Omega_\mu}\displaystyle\int_{\mathcal{B}_\mu} (\overline{\boldsymbol{\mathcal{C}}}^{-1} : \boldsymbol{C}_\mu - \mathbf{I}) : \mathcal{A}(\mathbf{y},\boldsymbol{\varepsilon}(\mathbf{x},t))d\mathcal{B}}_{=\boldsymbol{\mathcal{M}}(\boldsymbol{\varepsilon}(\mathbf{x},t))} : \dot{\boldsymbol{\varepsilon}}(\mathbf{x},t) \qquad \text{(c)} \\ = \boldsymbol{\mathcal{M}}(\boldsymbol{\varepsilon}(\mathbf{x},t)) : \dot{\boldsymbol{\varepsilon}}(\mathbf{x},t) \end{cases} \tag{30}$$

$$\begin{cases} \text{non-smooth} \\ \text{(localized)} \\ \text{internal strain} \end{cases} \rightarrow \begin{cases} \dot{\boldsymbol{\varepsilon}}^{(i)}(\mathbf{x},t) = \dfrac{1}{\ell_\mu}(\overline{\dot{\boldsymbol{\beta}}_\mu \otimes^s \mathbf{n}_\mu})_{\mathcal{S}_\mu} \\ \ell_\mu(\mathbf{x},t) \equiv \dfrac{\Omega_\mu}{L_\mu} \rightarrow \text{internal/characteristic length} \end{cases} \qquad \text{(d)}$$

In Eq. (30)(a), $\boldsymbol{\mathcal{C}}^{tang}_{hom}$, stands for the macroscale homogenized tangent constitutive operator, which can be pointwise obtained from a standard homogenization procedure, see [16]. In Eq. (30)(c) $\mathbf{I}$ is the fourth order symmetric unit tensor and $\mathcal{A}(\mathbf{y},\boldsymbol{\varepsilon})$ is a strain-concentration like tensor stemming from a standard homogenization of the constitutive behavior at the domain $\mathcal{B}_\mu$.

Equations in Box 2.2 display, in an incremental (rate) format, the macroscopic constitutive model inherited by the macro-scale from the homogenization procedure at the micro-scale. Although that model will not be used for computational purposes,[4] it supplies relevant insights on the properties of the resulting homogenized constitutive model and crucial requirements on the numerical model for the propagating material failure at the macro-scale, i.e.:

- Eq. (30)(a) corresponds to an inelastic constitutive equation in terms of the average elastic constitutive tensor, $\overline{\boldsymbol{\mathcal{C}}}$, at the microscale, see Eq. (30)(b), and some inelastic strains, $\dot{\boldsymbol{\chi}}(\mathbf{x},t)$ and $\boldsymbol{\varepsilon}^{(i)}(\mathbf{x},t)$, which would play the role of internal variables in phenomenological models. The evolution equations for those internal variables are given by Eqs. (30)(c) and (30)(d). Unlike in phenomenological models, their evolution is determined, at every macroscopic sampling point, $\mathbf{x}$, by homogenized values of entities at the corresponding micro-scale failure cell, $\mathcal{B}_\mu(\mathbf{x})$: i.e. $\overline{\boldsymbol{\varepsilon}}_\mu(\tilde{\mathbf{u}}_\mu(\mathbf{y},t),\boldsymbol{\beta}_\mu(\mathbf{y},t))$, the elastic properties at the micro-scale, $\boldsymbol{C}_\mu(\mathbf{y})$ and the specific failure mechanism activated at the micro-scale, $\mathcal{S}_\mu(\mathbf{x})$. This extends to non-smooth problems, some theoretical results already derived for smooth problems, see for instance [40,41].
- A characteristic length $\ell_\mu(\mathbf{x},t)$ emerges naturally in Eq. (30)(d). If $n_{\dim}\in\{2,3\}$ is the dimension of the problem then, ℓ_μ is the ratio of the measure of the failure cell, $\left|\mathcal{B}_\mu\right| = \Omega_\mu = \mathcal{O}(h_\mu^{n_{\dim}})$, and the measure (length/surface) of the activated micro-failure mechanism, $L_\mu = \left|\mathcal{S}_\mu\right| = \mathcal{O}(h_\mu^{(n_{\dim}-1)})$. In consequence ℓ_μ is of the order of the failure-cell size i.e.: $\ell_\mu = \mathcal{O}(h_\mu)$. If we assume scale separation, $h_\mu \ll L$ (see Fig. 1), then ℓ_μ is a very small number in the upper scale $\ell_\mu(\mathbf{x},t) \ll L$ (see Figs. 1 and 5).
- Eqs. (30) can be specified for the domains $\mathcal{B}_{loc}(t)$ and $\mathcal{B}\setminus\mathcal{B}_{loc}(t)$ at the macro scale as:

(1) *Smooth domain* $\mathcal{B}\setminus\mathcal{B}_{loc}(t)$:

The microscale behavior is instantaneously elastic (see Eqs. (4) and (6)) and, therefore, $\dot{\boldsymbol{\beta}}_\mu(\mathbf{y},t) = \mathbf{0}\ \forall\mathbf{y}$. Then, in Eq. (30)(d), $\dot{\boldsymbol{\varepsilon}}^{(i)}(\mathbf{x},t)=\mathbf{0}$ and Eqs. (30)(a) and (30)(c) read

$$\begin{aligned}\dot{\boldsymbol{\sigma}}(\mathbf{x},t) &= \overline{\boldsymbol{\mathcal{C}}} : [\dot{\boldsymbol{\varepsilon}}(\mathbf{x},t) + \dot{\boldsymbol{\chi}}(\mathbf{x},t)] \qquad \text{(a)}\\ \dot{\boldsymbol{\chi}}(\mathbf{x},t) &= \boldsymbol{\mathcal{M}} : \dot{\boldsymbol{\varepsilon}}(\mathbf{x},t) \qquad \text{(b)}\end{aligned} \tag{31}$$

and, therefore,

$$\dot{\boldsymbol{\sigma}}(\mathbf{x},t) = \underbrace{\overline{\boldsymbol{\mathcal{C}}} : (\mathbf{I}+\boldsymbol{\mathcal{M}})}_{\overline{\boldsymbol{\mathcal{C}}}^{elas}_{hom}} : \dot{\boldsymbol{\varepsilon}}(\mathbf{x},t) = \overline{\boldsymbol{\mathcal{C}}}^{elas}_{hom} : \dot{\boldsymbol{\varepsilon}}(\mathbf{x},t) \tag{32}$$

where $\overline{\boldsymbol{\mathcal{C}}}^{elas}_{hom}$ stands for the *homogenized elastic constitutive operator* at the failure cell $\mathcal{B}_\mu$.

Notice, from Eq. (31)(a), that a bounded strain, $\dot{\bar{\boldsymbol{\varepsilon}}}(\mathbf{x},t) = \dot{\boldsymbol{\varepsilon}}(\mathbf{x},t)$ is recovered at $\mathcal{B}\setminus\mathcal{B}_{loc}(t)$ as,

$$\dot{\boldsymbol{\varepsilon}}(\mathbf{x},t) = \underbrace{\overline{\boldsymbol{\mathcal{C}}}^{-1} : \dot{\boldsymbol{\sigma}}(\mathbf{x},t) - \dot{\boldsymbol{\chi}}(\mathbf{x},t)}_{\equiv\dot{\bar{\boldsymbol{\varepsilon}}}(\mathbf{x},t)\ (bounded)} = \dot{\bar{\boldsymbol{\varepsilon}}}(\mathbf{x},t) \quad \forall\mathbf{x}\in\mathcal{B}\setminus\mathcal{B}_{loc}(t). \tag{33}$$

(2) *Non-smooth domain* $\mathcal{B}_{loc}(t)$:

Material micro-structure displays some failure mechanism by triggering inelasticity (see Eqs. (5)) at the set of activated cohesive bands, $\mathcal{B}_{\mu,act}(\mathbf{x})$.

Therefore, $\dot{\boldsymbol{\beta}}_\mu(\mathbf{y},t)\neq\mathbf{0}\ \forall\mathbf{y}\in\mathcal{B}_{\mu,act}(\mathbf{x})$ and, from Eqs. (30)(a) and (30)(d),

$$\begin{aligned}\dot{\boldsymbol{\varepsilon}}(\mathbf{x},t) &= \underbrace{\overline{\boldsymbol{\mathcal{C}}}^{-1} : \dot{\boldsymbol{\sigma}}(\mathbf{x},t) - \dot{\boldsymbol{\chi}}(\mathbf{x},t)}_{\equiv\dot{\bar{\boldsymbol{\varepsilon}}}(\mathbf{x},t)\ (bounded)} + \frac{1}{\ell_\mu}\overline{(\dot{\boldsymbol{\beta}}_\mu\otimes^s\mathbf{n}_\mu)}_{\mathcal{S}_\mu}\\ &= \dot{\bar{\boldsymbol{\varepsilon}}}(\mathbf{x},t) + \frac{1}{\ell_\mu}\overline{(\dot{\boldsymbol{\beta}}_\mu\otimes^s\mathbf{n}_\mu)}_{\mathcal{S}_\mu} \quad \forall\mathbf{x}\in\mathcal{B}_{loc}.\end{aligned} \tag{34}$$

Eqs. (33) and (34) can be summarized for the complete domain $\mathcal{B}$ as:

$$\begin{aligned}\dot{\boldsymbol{\varepsilon}}(\mathbf{x},t) &= \underbrace{\overline{\boldsymbol{\mathcal{C}}}^{-1} : \dot{\boldsymbol{\sigma}}(\mathbf{x},t) - \dot{\boldsymbol{\chi}}(\mathbf{x},t)}_{\equiv\dot{\bar{\boldsymbol{\varepsilon}}}(\mathbf{x},t)\ (smooth)} + \frac{\kappa_{\mathcal{B}_{loc}}}{\ell_\mu}\overline{(\dot{\boldsymbol{\beta}}_\mu\otimes^s\mathbf{n}_\mu)}_{\mathcal{S}_\mu}\\ &= \dot{\bar{\boldsymbol{\varepsilon}}}(\mathbf{x},t) + \frac{\kappa_{\mathcal{B}_{loc}}}{\ell_\mu}\overline{(\dot{\boldsymbol{\beta}}_\mu\otimes^s\mathbf{n}_\mu)}_{\mathcal{S}_\mu} = \dot{\bar{\boldsymbol{\varepsilon}}}(\mathbf{x},t) + \delta_{\mathcal{S}}^{\ell_\mu}\overline{(\dot{\boldsymbol{\beta}}_\mu\otimes^s\mathbf{n}_\mu)}_{\mathcal{S}_\mu}.\end{aligned} \tag{35}$$

[4] Instead, the homogenized value of the stresses in Eq. (18) is point-wise used to evaluate the current macro-stresses in terms of the corresponding macro-strains.

Remark 2.3. Comparing Eq. (35) with Eq. (2), one realizes that the former defines a ℓ_μ-*regularized discontinuity kinematics of bandwidth* $h = \ell_\mu$. This is a fact of crucial importance for a proper and meaningful modeling of the material failure propagation at the upper scale. In fact, Eq. (35) suggests that the numerical approach for capturing this propagation has to be consistent with the aforementioned kinematics of regularized strong discontinuity and, more specifically, regularized with the characteristic length ℓ_μ.

Remark 2.4. The role of the characteristic length, ℓ_μ, is not only computational, but it has also other relevant physical and mechanical implications. Consideration of such a characteristic length for multi-scale based approaches has been claimed from the materials mechanics community [20] and introduced in a heuristic way in some previous approaches [30].

Remarkably, in the proposed approach, this length, ℓ_μ, is *naturally derived* from the homogenization setting; it depends on both specific data of the problem and local results of the analysis. For instance: (a) the considered macro-scale material point, $\mathbf{x}$, (b) the microscale failure-cell size, h_μ, (c) the morphology at the micro-scale (d) the activated failure mechanism at the failure-cell, $\mathcal{S}_\mu$, which, in turn, depends on (d) the history and evolution of the mechanical variables at the micro-scale.

Remark 2.5. It is emphasized that all the results in this section are *a priori results*, i.e. not specifically imposed neither in the algorithmic nor in the numerical implementation of the resulting model. They stem because of using the *standard continuum computational homogenization procedure* in Section 2.3, on a failure cell in the micro-scale, exhibiting strong discontinuities (see Fig. 2). Therefore, these results are going to be considered *assessment conditions*, not specifically imposed in the simulations, whose fulfillment is going to be checked in the numerical simulation results in Section 4 as a proof of the consistency of those results.

2.5. Time evolution of material failure at the macroscale. Transition from weak to strong discontinuity

Eq. (35) corresponds to a specific format of the weak discontinuity kinematics in Eq. (2) with

$$\dot{\gamma}(\mathbf{x},t) := \overline{(\dot{\boldsymbol{\beta}}_\mu \otimes^s \mathbf{n}_\mu)}_{\mathcal{S}_\mu} = \frac{1}{L_\mu}\int_{\mathcal{S}_\mu} (\dot{\boldsymbol{\beta}}_\mu \otimes \mathbf{n}_\mu)^S d\mathcal{S}. \tag{36}$$

Since $\overline{(\dot{\boldsymbol{\beta}}_\mu \otimes^s \mathbf{n}_\mu)}_{\mathcal{S}_\mu}$ is not necessarily a rank-one tensor,[5] it does not match necessarily the strong discontinuity kinematics in Eq. (3) corresponding to a propagating displacement discontinuity, but it evolves towards this situation along time. The time of the analysis, at which Eq. (36) takes the format

$$\begin{aligned} &\dot{\gamma}(\mathbf{x},t_B) = \overline{(\dot{\boldsymbol{\beta}}_\mu(\mathbf{y},t_B)\otimes^s \mathbf{n}_\mu(\mathbf{y}))}_{\mathcal{S}_\mu} = (\dot{\boldsymbol{\beta}}(\mathbf{x},t_B)\otimes \mathbf{n}(\mathbf{x}))^S = \dot{\xi}(\mathbf{m}\otimes\mathbf{n})^S \neq \mathbf{0} \\ &\dot{\boldsymbol{\beta}} = \dot{\xi}\mathbf{m}; \quad \|\mathbf{m}\| = \|\mathbf{n}\| = 1 \end{aligned} \tag{37}$$

will determine the *bifurcation time* $t_B(\mathbf{x})$. In other words, t_B is the time at which material failure, displaying localized strains in a weak discontinuity format (see Eq. (2)), starts propagating, as a strong discontinuity, at the considered macro-scale point, $\mathbf{x}$. Determination of this time, and the so-called polarization directions $\mathbf{n}(\mathbf{x})$ and $\mathbf{m}(\mathbf{x})$,[6] is done in the context of the well-known discontinuous bifurcation analysis [42,43] by solving the problem:

Problem.

$$\begin{aligned} &\textit{GIVEN } \mathbf{Q}_t(\mathbf{x},\mathbf{n}) = \mathbf{n}\cdot\boldsymbol{\mathcal{C}}^{tang}_{hom}(\mathbf{x},t)\cdot\mathbf{n}; \quad \mathbf{x}\in\mathcal{S};\ t\in[0,T] \\ &\textit{FIND } \text{the first } t\equiv t_B(\mathbf{x})\in[0,T] \quad \text{and all} \quad \mathbf{n}\in\mathbb{I} := \{\boldsymbol{\nu}\in\mathbb{R}^{n_{\dim}} \mid \|\boldsymbol{\nu}\| = 1\} \\ &\textit{FULFILLING}: \quad \mathbf{Q}_{t_B}(\mathbf{x},\mathbf{n})\cdot\mathbf{m} = \mathbf{0} \quad \text{for some } \mathbf{m}\in\mathbb{I} \end{aligned} \tag{38}$$

where $\boldsymbol{\mathcal{C}}^{tang}_{hom}$ is the macroscale (homogenized) tangent constitutive (see Eq. (30)(a)), $[0,T]$ is the time interval of interest and $\mathbf{Q}_t(\mathbf{x},\mathbf{n})$ is the localization tensor.

[5] Since the sum (integral) of rank-one tensors is not a rank-one tensor.

[6] For symmetric $\boldsymbol{\mathcal{C}}^{tang}_{hom}$ the problem is indifferent to the order of the couple $(\mathbf{n},\mathbf{m})$.

A general numerical procedure for solving this problem can be found in [44]. In general Eq. (38) provides the bifurcation time, $t_B(\mathbf{x})$, and two solutions for the normal to the discontinuity path $\mathcal{S}$ (see Fig. 1) i.e.: $\mathbf{n}_1(\mathbf{x}) \equiv \mathbf{n}$, $\mathbf{n}_2(\mathbf{x}) \equiv \mathbf{m}$.

Now, examining Eq. (37), one realizes that the equality is fulfilled under the following circumstances:

(1) The fluctuations jump at the microscale, $\dot{\beta}_\mu$, is *spatially constant* at the failure-cell:

$$\begin{aligned} &\dot{\beta}_\mu(\mathbf{x},\mathbf{y},t) = \dot{\boldsymbol{\beta}}_\mu(\mathbf{x},t) \quad \forall \mathbf{y} \in \mathcal{B}_\mu \\ &\Rightarrow \begin{cases} \overline{(\dot{\boldsymbol{\beta}}_\mu \otimes^s \mathbf{n}_\mu)}_{\mathcal{S}_\mu} = (\dot{\boldsymbol{\beta}}_\mu(\mathbf{x},t) \otimes \overline{\mathbf{n}_\mu(\mathbf{x},\mathbf{y})}_{\mathcal{S}_\mu})^S = \zeta(\dot{\boldsymbol{\beta}}_\mu(\mathbf{x},t) \otimes \mathbf{a}(\mathbf{x}))^S \\ \mathbf{a}(\mathbf{x}) = \dfrac{1}{\zeta}\overline{\mathbf{n}_\mu(\mathbf{x},\mathbf{y})}_{\mathcal{S}_\mu}; \quad \|\mathbf{a}\| = 1; \quad \zeta(\mathbf{x}) = \left\|\overline{\mathbf{n}_\mu(\mathbf{x},\mathbf{y})}_{\mathcal{S}_\mu}\right\| = \zeta(\mathbf{n}_\mu) \end{cases} \end{aligned} \tag{39}$$

where factor $\zeta(\mathbf{x})$ is a measure of the *tortuosity* of the activated micro-scale failure path $\mathcal{S}_\mu$ (for instance, for $\mathcal{S}_\mu$ being a straight line then $\zeta = 1$). A similar expression for this tortuosity can be found in [45].

Replacing Eq. (39) into Eq. (37) yields:

$$\zeta(\dot{\boldsymbol{\beta}}_\mu(\mathbf{x},t) \otimes \mathbf{a}(\mathbf{x}))^S = (\dot{\boldsymbol{\beta}}(\mathbf{x},t) \otimes \mathbf{n}(\mathbf{x}))^S \Rightarrow \begin{cases} \dot{\boldsymbol{\beta}}(\mathbf{x},t) = \zeta(\mathbf{n}_\mu)\dot{\boldsymbol{\beta}}_\mu(\mathbf{x},t) = \mathcal{F}(\mathbf{n}_\mu, \dot{\boldsymbol{\beta}}_\mu) \\ \mathbf{n}(\mathbf{x}) = \mathbf{a}(\mathbf{x}) = \dfrac{1}{\zeta(\mathbf{n}_\mu)}\overline{(\mathbf{n}_\mu)}_{\mathcal{S}_\mu} = \mathcal{G}(\mathbf{n}_\mu). \end{cases} \tag{40}$$

(2) The activated failure path at the micro-scale, $\mathcal{S}_\mu$, is a straight line (or a plain surface), with spatially constant normal $\mathbf{n}_\mu$:

$$\begin{aligned} &\mathbf{n}_\mu(\mathbf{x},\mathbf{y}) = \mathbf{n}_\mu(\mathbf{x}) \\ &\Rightarrow \mathbf{n}(\mathbf{x}) = \mathbf{n}_\mu(\mathbf{x}); \qquad \dot{\boldsymbol{\beta}}(\mathbf{x},t) = \overline{\dot{\boldsymbol{\beta}}_\mu(\mathbf{x},\mathbf{y},t)}. \end{aligned} \tag{41}$$

This is an academic case, since it corresponds to a non-realistic microstructural morphology of the failure-cell ($\mathcal{B}_{\mu,coh}$ defines a straight/plane band). Therefore, it will be discarded because of its lack of physical significance and practical interest.

Remark 2.6. The previous analysis leads to the following statements:

1. The (rate of the) micro-scale displacement-jump function (after bifurcation) is constant across the failure-cell ($\dot{\boldsymbol{\beta}}_\mu(\mathbf{x},\mathbf{y},t) = \dot{\boldsymbol{\beta}}_\mu(\mathbf{x},t), \forall \mathbf{y} \in \mathcal{B}_\mu(\mathbf{x})$) in Eq. (39).
2. The (rate of the) macro-scale displacement-jump function, $\dot{\boldsymbol{\beta}}(\mathbf{x},t)$, (after bifurcation) equals the micro-fluctuation jump, $\dot{\boldsymbol{\beta}}_\mu(\mathbf{x},t)$, corrected by the (scalar) tortuosity factor ($\dot{\boldsymbol{\beta}}(\mathbf{x},t) = \zeta(\mathbf{x})\dot{\boldsymbol{\beta}}_\mu(\mathbf{x},t)$ in Eq. (40)(a)).
3. After bifurcation, the macroscale normal to the crack-path $\mathbf{n}(\mathbf{x})$ equals the (normalized) average of the normal to the corresponding microscopic failure mechanism $\mathbf{a}(\mathbf{x}) = \frac{1}{\zeta}\overline{\mathbf{n}_\mu(\mathbf{x},\mathbf{y})}_{\mathcal{S}_\mu}$ in Eq. (40)(b).
4. It should also be noticed another subtle aspect of statements 2 and 3 above. In fact, inspection of Eqs. (37) and (39) reveals that the symmetric operator $(\mathbf{n} \otimes \mathbf{m})^S$ makes the results insensitive with respect to an interchange of vectors $\mathbf{n} \rightleftarrows \mathbf{m}$. Therefore, besides the solutions in Eq. (40), solutions

$$\begin{aligned} &\dot{\boldsymbol{\beta}}^*(\mathbf{x}) = \left\|\dot{\boldsymbol{\beta}}_\mu(\mathbf{x})\right\| \mathbf{a}(\mathbf{x}) = \left\|\dot{\boldsymbol{\beta}}_\mu(\mathbf{x})\right\| \frac{\overline{(\mathbf{n}_\mu)}_{\mathcal{S}_\mu}}{\zeta(\mathbf{n}_\mu)} = \mathcal{F}^*(\dot{\boldsymbol{\beta}}_\mu, \mathbf{n}_\mu) \\ &\mathbf{n}^*(\mathbf{x}) = \frac{1}{\left\|\dot{\boldsymbol{\beta}}_\mu(\mathbf{x})\right\|}\dot{\boldsymbol{\beta}}_\mu(\mathbf{x}) = \mathcal{G}^*(\dot{\boldsymbol{\beta}}_\mu) \end{aligned} \tag{42}$$

fulfilling

$$(\dot{\boldsymbol{\beta}}^* \otimes \mathbf{n}^*)^S = (\underbrace{\dot{\boldsymbol{\beta}}_\mu(\mathbf{x})}_{=\dot{\boldsymbol{\beta}}} \otimes \underbrace{\frac{\overline{(\mathbf{n}_\mu)}_{\mathcal{S}_\mu}}{\zeta(\mathbf{n}_\mu)}}_{=\mathbf{n}})^S = (\dot{\boldsymbol{\beta}} \otimes \mathbf{n})^S \tag{43}$$

are also admissible. In other words, what is relevant for the resulting macroscopic homogenized constitutive model is not the couple $(\mathbf{n}, \dot{\boldsymbol{\beta}})$ but its symmetric tensor product.

This *indifference*, with respect to vector swap in $(\mathbf{n}\otimes\mathbf{m})^S$, motivates that *a given microscopic failure mechanism* $\{\mathbf{n}_\mu, \dot{\boldsymbol{\beta}}_\mu\}$ *gives rise to two possible combinations* of the macro-scale displacement jump and normal:

$$\begin{aligned}&\{\dot{\boldsymbol{\beta}}, \mathbf{n}\} \equiv \{\mathcal{F}(\mathbf{n}_\mu, \dot{\boldsymbol{\beta}}_\mu), \mathcal{G}(\mathbf{n}_\mu)\}\\ &\{\dot{\boldsymbol{\beta}}^*, \mathbf{n}^*\} \equiv \{\mathcal{F}^*(\dot{\boldsymbol{\beta}}_\mu, \mathbf{n}_\mu), \mathcal{G}^*(\dot{\boldsymbol{\beta}}_\mu)\}\end{aligned} \tag{44}$$

as in Eqs. (40) and (42). This enriches the modeling capabilities of the approach for propagation directions in the macroscale. Indeed, even with a relatively poor description of the failure mechanisms at the microscopic scale (restricted set of $\mathbf{n}_\mu$'s but unrestricted set of $\dot{\boldsymbol{\beta}}_\mu$'s) a much wider set of propagation directions ($\{\mathbf{n} \mid \mathbf{n} = \mathcal{G}(\mathbf{n}_\mu)\} \bigcup \{\mathbf{n}^* \mid \mathbf{n}^* = \mathcal{G}^*(\dot{\boldsymbol{\beta}}_\mu)\}$) can be captured at the macro-scale.

These are *a priori* results, not explicitly imposed in the approach, which shall be corroborated by the numerical simulations in Section 4.

2.6. Energy dissipation. Fracture energy issues

The material failure at the micro-cell $\mathcal{B}_\mu$, translates into propagating failure at the macro-scale, which, in turn, is captured through the regularized strain localization band, $\mathcal{B}_{loc}(t)$ (see Fig. 5). The proposed approach enforces this *bandwidth to be precisely the characteristic length,* $\ell_\mu(\mathbf{x})$ in Eq. (30)(d).

Let us consider the fracture energy, $G^f_\mu(\mathbf{y})$, corresponding to points $\mathbf{y} \in \mathcal{B}_{\mu,act}$ at the microscale, understood as a material property that can be different for every material compound at the microstructure, and the macro-scale fracture energy, $G^f(\mathbf{x})$, obtained *as an output* from the homogenization procedure. According to their definition (expended power per unity of mid-surface of the localization band) those fracture energies can be, respectively computed, in terms of the fracture energy densities[7] (per unit of volume) $g^f(\mathbf{x})$ and $g^f_\mu(\mathbf{x})$:

$$\begin{aligned}&g^f(\mathbf{x}) = \frac{G^f(\mathbf{x})}{\ell_\mu(\mathbf{x})} = \int_0^\infty \boldsymbol{\sigma}(\mathbf{x},t) : \dot{\boldsymbol{\varepsilon}}(\mathbf{x},t)dt \quad \forall \mathbf{x} \in \mathcal{B}_{loc} \qquad \text{(a)}\\ &g^f_\mu(\mathbf{y}) = \frac{G^f_\mu(\mathbf{y})}{k} = \int_0^\infty \boldsymbol{\sigma}_\mu(\mathbf{y},t) : \dot{\boldsymbol{\varepsilon}}_\mu(\mathbf{y},t)dt \quad \forall \mathbf{y} \in \mathcal{B}_{\mu,coh}. \quad \text{(b)}\end{aligned} \tag{45}$$

In this setting, the following lemma holds:

Lemma. *The macroscopic fracture energy,* $G^f(\mathbf{x})$, is the average of the microscopic fracture energy $G^f_\mu(\mathbf{y})$, *along the activated failure mechanism path at the micro-scale,* $\mathcal{S}_\mu(\mathbf{x})$ *(see Fig. 5):*

$$G^f(\mathbf{x}) = \frac{1}{L_\mu(\mathbf{x})} \int_{\mathcal{S}_\mu(\mathbf{x})} G^f_\mu(\mathbf{y})\, d\mathcal{S}_\mu = \overline{G^f_\mu(\mathbf{y})}_{\mathcal{S}_\mu}. \tag{46}$$

Proof. Considering the Hill–Mandel principle in Eq. (17), Eq. (45)(a) reads,

$$\begin{aligned}\frac{G^f(\mathbf{x})}{\ell_\mu(\mathbf{x})} &= \int_0^\infty \boldsymbol{\sigma}(\mathbf{x},t) : \dot{\boldsymbol{\varepsilon}}(\mathbf{x},t)dt = \int_0^\infty \left[\frac{1}{\Omega_\mu}\int_{\mathcal{B}_\mu} \boldsymbol{\sigma}_\mu(\mathbf{x},\mathbf{y},t) : \dot{\boldsymbol{\varepsilon}}_\mu(\mathbf{x},\mathbf{y},t) d\mathcal{B}_\mu\right] dt\\ &= \int_0^\infty \left[\frac{1}{\Omega_\mu}\int_{\mathcal{B}_{\mu,act}} \boldsymbol{\sigma}_\mu(\mathbf{x},\mathbf{y},t) : \dot{\boldsymbol{\varepsilon}}_\mu(\mathbf{x},\mathbf{y},t) \underbrace{d\mathcal{B}_{\mu,act}}_{=k\cdot d\mathcal{S}_\mu}\right] dt\\ &= \int_{\mathcal{S}_\mu} \left[\frac{k}{\Omega_\mu}\int_{t_B}^\infty \boldsymbol{\sigma}_\mu(\mathbf{x},\mathbf{y},t) : \dot{\boldsymbol{\varepsilon}}_\mu(\mathbf{x},\mathbf{y},t)dt\right] d\mathcal{S}_\mu\end{aligned} \tag{47}$$

[7] Strictly speaking, the integration of the macroscopic specific fracture energy, $g^f(\mathbf{x})$ in Eq. (45)(a) should be evaluated along the interval $[t_B, \infty]$, where $t_B(\mathbf{x})$ stands for the macroscopic bifurcation time in Eq. (38). Nevertheless, here the pre-bifurcation dissipated energy at the macro-scale is considered negligible, so that it is integrated along the interval $[0, \infty]$.

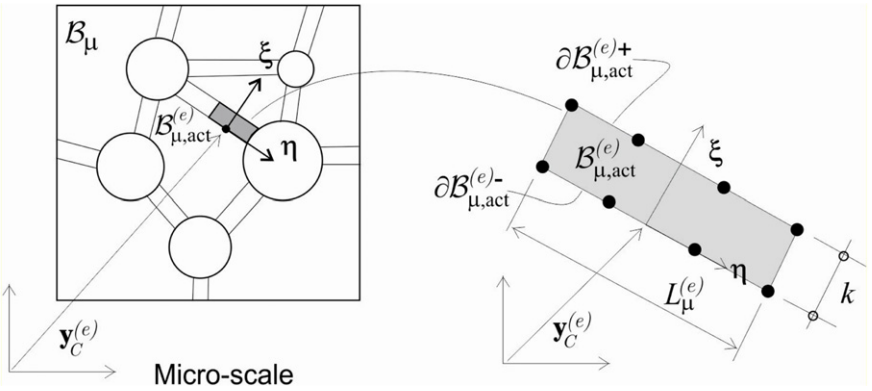

Fig. 6. Multiscale model: finite element discretization at the micro-scale.

where the fact that, in the domain outside the active bands $\mathcal{B}_\mu \setminus \mathcal{B}_{\mu,act}$, the material is elastic (with no dissipation), has been taken into account. Now, inserting Eq. (45)(b) into Eq. (47), and considering the definition of the characteristic length, ℓ_μ in Eq. (30)(d), yields

$$\frac{G^f(\mathbf{x})}{\ell_\mu(\mathbf{x})} = \frac{1}{\Omega_\mu}\int_{\mathcal{S}_\mu} \underbrace{\left[k\int_0^\infty \boldsymbol{\sigma}_\mu(\mathbf{x},\mathbf{y},t) : \dot{\boldsymbol{\varepsilon}}_\mu(\mathbf{x},\mathbf{y},t)dt\right]}_{G^f_\mu(\mathbf{y})} d\mathcal{S}_\mu = \frac{1}{\Omega_\mu}\int_{\mathcal{S}_\mu(\mathbf{x})} G^f_\mu(\mathbf{y})\, d\mathcal{S}_\mu$$
$$= \underbrace{\frac{L_\mu}{\Omega_\mu}}_{\frac{1}{\ell_\mu(\mathbf{x})}} \frac{1}{L_\mu}\int_{\mathcal{S}_\mu(\mathbf{x})} G^f_\mu(\mathbf{y})\, d\mathcal{S}_\mu = \frac{1}{\ell_\mu(\mathbf{x})}\overline{G^f_\mu(\mathbf{y})_{\mathcal{S}_\mu}} \tag{48}$$

which proves the Lemma.

Remark 2.7. For homogeneous fracture energy at the active cohesive bands ($G^f_\mu(\mathbf{y}) = G^f_\mu \; \forall \mathbf{y} \in \mathcal{B}_{\mu,act}$) the lemma, consistently, translates into *conservation of the fracture energy along the scales* i.e.:

$$G^f(\mathbf{x}) = G^f_\mu. \tag{49}$$

The previous results rely crucially on the ability to induce a localization band of bandwidth $\ell_\mu(\mathbf{x})$ at the macro-scale. This issue is tackled in Appendix B.

3. Propagation of material failure

3.1. Propagation of material failure at the micro-scale. Failure cell finite element model

A standard finite element model is adopted for the numerical simulation of the RVE/failure-cell response. One, quadrilateral,[8] finite element is used across the thickness of the cohesive bands $\mathcal{B}_{\mu,coh}$, as shown in Fig. 6. The interpolation order along the coordinate η may be arbitrary. However, it must be linear along the coordinate ξ in order to capture the function $\mathcal{H}_{\mathcal{B}_{\mu,k}}(\eta)$ defined in Eq. (8)(b).

Propagation of material failure along the cohesive bands takes place, in a natural fashion, as inelasticity is triggered in one element, $\mathcal{B}^{(e)}_{\mu,coh}$, and it propagates across other elements of $\mathcal{B}_{\mu,coh}$. The set of all elements, e, of the cohesive bands experiencing inelastic loading at the center point $\mathbf{y}^{(e)}_C$ of the element, see Fig. 6, determines, at every time, t, the failure mechanism at the micro-scale, i.e.:

$$\mathcal{B}_{\mu,act}(t) := \left\{\bigcup \mathcal{B}^{(e)}_{\mu,coh};\; \dot{r}_\mu(\mathbf{y}^{(e)}_C, t) > 0\right\} \tag{50}$$

[8] However, there is no intrinsic restriction for using other options, like triangular elements.

where the instantaneous inelasticity status (de-cohesion) is evaluated in terms of a positive evolution of the internal variable $\dot{r}_\mu > 0$ (see Box 2.1).
From Eq. (50), one can determine the measure (length/surface) of the activated failure mechanism in Eq. (30)(d) and the corresponding characteristic length as

$$\begin{cases} L_\mu(\mathbf{x},t) = \displaystyle\sum_{\forall \mathcal{B}^{(e)}_{\mu,act} \subset \mathcal{B}_{\mu,act}(\mathbf{x},t)} L^{(e)}_\mu & \text{(a)} \\ \ell_\mu(\mathbf{x},t) \equiv \dfrac{\Omega_\mu}{L_\mu(\mathbf{x},t)} < h^{(e)}(\mathbf{x}) & \text{(b)} \end{cases} \tag{51}$$

where $L^{(e)}_\mu$ stands for the individual length of the active element, $\mathcal{B}^{(e)}_{\mu,act}$, in the set of active cohesive bands $\mathcal{B}_{\mu,act}(t)$.

Remark 3.1. In practice, dependence on pseudo-time, t, of entities $\mathcal{B}_{\mu,act}(t)$, $L_\mu(\mathbf{x},t)$ and $\ell_\mu(\mathbf{x},t)$ in Eq. (51) only holds for the time interval $[t_Y(\mathbf{x}), t_B(\mathbf{x})]$, where $t_Y(\mathbf{x})$ stands for the time where material inelasticity starts at the failure cell, and $t_B(\mathbf{x})$ is the macroscopic bifurcation time in Eq. (38). At time $t_B(\mathbf{x})$, the failure mechanism at the cell is assumed fully consolidated and $\ell_\mu(\mathbf{x},t)$ in Eq. (51)(b) is made constant in time and redefined as:

$$\ell_\mu(\mathbf{x},t) := \ell_\mu(\mathbf{x}) = \ell_\mu(\mathbf{x}, t_B(\mathbf{x})) \quad \forall t \geq t_B(\mathbf{x}). \tag{52}$$

Remark 3.2. In Eq. (51)(b), limitation $\ell_\mu(\mathbf{x},t) < h^{(e)}(\mathbf{x})$ resolves, the singularity for the case that no damage occurs at the micro-scale (i.e. $L_\mu = 0 \rightarrow \ell_\mu = \infty$ in the elastic case, when ℓ_μ does not play any role). On the other hand, it ensures a positive value for the integration weights in the numerical integration procedure involved in the strain injection method described in Appendix B (see Table 3). In any case, this limitation, which can be removed if other crack-propagation techniques are used at the macro-scale, is not a strong one since, roughly speaking, it establishes that the failure-cell size, h_μ, has to be smaller than the macro-scale finite element size ($h_\mu(\mathbf{x}) \simeq \ell_\mu(\mathbf{x},t) < h^{(e)}(\mathbf{x})$). This restriction is, normally, largely exceeded by the scale separation requirement.

3.1.1. Unstable failure modes. Imposition of constant fluctuation jumps at cohesive bands

Inspection of equations in Box 2.2 reveals that the model might exhibit some instability. Indeed, the structure of the inelastic strain in Eq. (30)(c), allows situations displaying:

$$\begin{aligned} &\dot{\boldsymbol{\beta}}_\mu(\mathbf{y}) \neq \mathbf{0} \quad \text{for some } \mathbf{y} \in \mathcal{S}_\mu && \text{(a)} \\ &\dot{\boldsymbol{\varepsilon}}^{(i)}(\mathbf{x},t) = \frac{1}{\ell_\mu}(\overline{\dot{\boldsymbol{\beta}}_\mu(\mathbf{x},\mathbf{y}) \otimes^s \mathbf{n}_\mu(\mathbf{x},\mathbf{y})})_{\mathcal{S}_\mu} = \mathbf{0} && \text{(b)} \end{aligned} \tag{53}$$

which can give rise to some instabilities in the microscopic failure mechanisms. In Appendix A, this issue is studied and a remedy to preclude this instabilities, based on imposing an internal restriction in the fluctuations on same of the cohesive bands, is presented.

3.2. Propagation of material-failure at the macroscale. Crack-path-field and strain injection techniques in multi-scale problems

A difficult issue in computational modeling of material failure is the appropriate capture of its onset and propagation. Material failure propagation algorithms aim at answering the following two questions: (1) *when* does failure trigger at a given material point?, and, (2) *how* does it propagates?

As commented in Section 3.1, at the lower scale (failure-cell) where the morphology and position of candidate propagation mechanisms (set $\mathcal{B}_{\mu,coh}$) are predefined, this is a minor issue; both questions are automatically answered in terms of when and what cohesive-band elements enter into the softening regime according to Eq. (50). However, at the upper scale, there is no predefinition of the failure path and, in principle, any material point may fail and propagate in any direction.

To answer the above questions, in this work we have extended, to the multiscale case, a procedure for modeling onset and propagation of discontinuities recently developed by the authors for one-scale problems [31]. The proposed methodology is based on the use of two specific techniques:

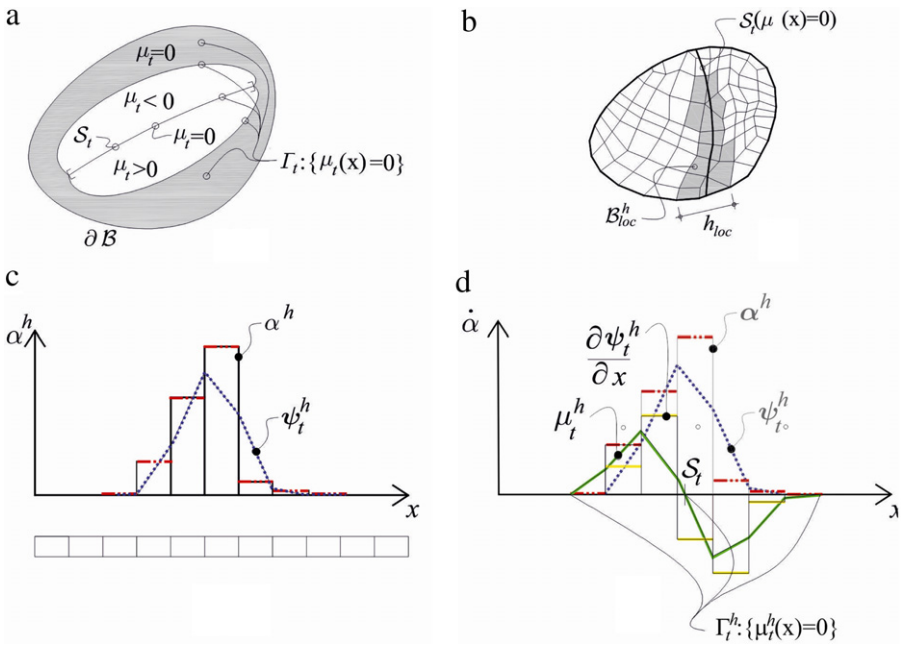

Fig. 7. Crack-path-field technique. (a) and (b) evolving crack-path, $\mathcal{S}_t$, (c) and (d) 1D sketch of the algorithm to obtain the crack path field from the smooth derivative of the localized variable α (see also Box 3.1).

(1) *Crack-path-field techniques*, consisting of the identification of the trace, during time and across the domain $\mathcal{B}$, of an evolving strong discontinuity represented by a strain localized field, in the subset $\mathcal{B}_{sd} \subset \mathcal{B}$. The so-called crack path field, $\mu(\mathbf{x}, t)$, is obtained from a selected localized scalar variable, $\alpha(\mathbf{x}, t)$, and its zero level set identifies, at every time t of the analysis, the domain, Γ_t, that contains the crack-path, $\mathcal{S}_t$. It is computed as:

$$\mathcal{S}_t \subset \Gamma_t := \left\{ \mathbf{x} \in \mathcal{B}_{loc};\ \mu(\mathbf{x}, t) = \frac{\partial \alpha}{\partial e} \equiv \nabla \alpha \cdot \hat{\mathbf{e}}(\mathbf{x}, t) = 0 \right\} \tag{54}$$

which identifies the crack path as the locus of the e-directional maximum of the field $\alpha(\mathbf{x}, t)$ (see Fig. 7). The optimum value for the directional unit vector, $\hat{\mathbf{e}}(\mathbf{x}, t)$, in Eq. (54) should be the one orthogonal to the crack path, Γ_t, which, in turn is the unknown of the problem. From the authors' experience, a convenient, approximate, value for $\hat{\mathbf{e}}(\mathbf{x}, t)$, is extracted from the gradient of a displacement field scalar measure,[9] $a(\mathbf{x}, t)$, i.e.:

$$\begin{aligned} \mathbf{e}(\mathbf{x}, t) &= \boldsymbol{\nabla} a(\mathbf{x}, t) \\ a(\mathbf{x}, t) &= \sum_{i=1}^{n_{\text{dim}}} \boldsymbol{\nabla} u_i(\mathbf{x}, t); \quad u_i(\mathbf{x}, t) = \mathbf{u}(\mathbf{x}, t) \cdot \hat{\mathbf{e}}_i \\ \hat{\mathbf{e}}(\mathbf{x}, t) &= \frac{\mathbf{e}(\mathbf{x}, t)}{\|\mathbf{e}(\mathbf{x}, t)\|}. \end{aligned} \tag{55}$$

For the present multiscale approach, the localized variable $\alpha(\mathbf{x}, t)$ in Eq. (54) has to be specifically imported from the microstructure. Here, it is proposed the following definition in terms of the damage variable at the microscale, r_μ in Box 2.1, i.e.:

$$\begin{cases} \dot{\alpha}(\mathbf{x}, t) = \ell_\mu(\mathbf{x}, t) \dfrac{1}{\Omega_\mu} \displaystyle\int_{\Omega_\mu} \dot{r}_\mu(\mathbf{x}, \mathbf{y}, t)\, d\Omega = \frac{1}{L_\mu(\mathbf{x}, t)} \int_{\Omega_\mu} \dot{r}_\mu(\mathbf{x}, \mathbf{y}, t)\, d\Omega & \text{(a)} \\ \alpha(\mathbf{x}, 0) = 0 & \text{(b)} \end{cases} \tag{56}$$

where ℓ_μ is the characteristic length, defined in Eq. (51)(b).

[9] This approximately identifies $\mathbf{e}(\mathbf{x}, t)$ as the direction orthogonal the localization propagation.

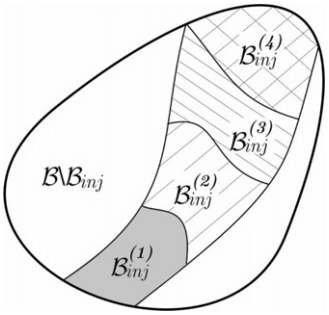

Fig. 8. Strain injection: the injection domains, $\mathcal{B}_{inj}^{(i)}(t)$, are injected an assumed (rate of) strain, $\dot{\varepsilon}_{inj}^{(i)}(\mathbf{x},t)$, in the specific time interval $[]_{inj}^{(i)} \subset [0,T]$.

Box 3.1.
Crack-path-field problem

Problem.

GIVEN:

$$\alpha(\mathbf{x},t) : \mathcal{B}\times[0,T] \to \mathbb{R}^+$$

$$\hat{\mathbf{e}}(\mathbf{x},t) : \mathcal{B}\times[0,T] \to \mathbb{I} := \{\mathbf{v}\in\mathbb{R}^{n_{\dim}} |\ \|\mathbf{v}\| = 1\}$$

$$\mathcal{V} := \left\{ \eta(\mathbf{x}) = \sum_{1}^{n_{node}} N_i(\mathbf{x})\eta_i;\ \eta \in H^1(\mathcal{B}) \right\}$$

$$\mathcal{V}_0 := \left\{ \eta(\mathbf{x}) = \sum_{1}^{n_{node}} N_i(\mathbf{x})\,\eta_i; \eta \in H^1(\mathcal{B});\ \eta|_{\partial\mathcal{B}} = 0 \right\}$$

FIND:

$$\text{(a) } \psi_t(\mathbf{x}) \in \mathcal{V} \textit{ fulfilling } \int_{\mathcal{B}^h} \overline{\psi}(\psi_t - \alpha(\mathbf{x},t))d\mathcal{B} = 0 \quad \forall\overline{\psi}\in\mathcal{V}_0$$

$$\text{(b) } \mu_t(\mathbf{x}) \in \mathcal{V} \textit{ fulfilling } \int_{\mathcal{B}^h} \overline{\mu}\left(\mu_t - \underbrace{\frac{\partial\psi_t}{\partial e}}_{\nabla\psi_t\cdot\hat{\mathbf{e}}}\right) d\mathcal{B} = 0 \quad \forall\overline{\mu}\in\mathcal{V}_0 \tag{57}$$

$$\text{(c) } \Gamma_t := \{\mathbf{x}\in\mathcal{B};\ \mu_t(\mathbf{x}) = 0\} \to \textit{zero level set of } \mu_t(\mathbf{x})$$

The corresponding algorithm, based on smoothing the variables $\alpha(\mathbf{x},t)$ and $\frac{\partial\alpha}{\partial e}$ in Eqs. (54) and (56), is presented in Box 3.1.

(2) *Strain injection techniques*: consisting of the insertion in specific, time-dependent, sub-domains $\mathcal{B}_{inj}^{(i)}(t) \subset \mathcal{B}$, $\mathcal{B}_{inj}(t) = \bigcup_{i=1}^{n_{inj}} \mathcal{B}_{inj}^{(i)}(t)$ (see Fig. 8), of goal-oriented strain fields. By using strain injection techniques a number of different strain rate patterns, $\dot{\boldsymbol{\varepsilon}}(\mathbf{x},t) \equiv \dot{\boldsymbol{\varepsilon}}_t(\mathbf{x})$, can be inserted at the specific domains, $\mathcal{B}_{inj}^{(i)}(t)$, using classical two-field, $\dot{\boldsymbol{\varepsilon}}_t(\mathbf{x})/\boldsymbol{\nabla}^s\dot{\boldsymbol{u}}_t(\mathbf{x})$ mixed finite element strategies [37]. The format of the considered problem in terms of rates (see Box 3.2), allows keeping the resulting time-varying problem smooth in time, in spite of the, possible, sudden changes of the injected rate-of-strain formats. More details on the technique can be found in a work of the authors [31].

Box 3.2.
General strain-injection variational problem (in rate form)

Problem.

$$
\begin{aligned}
&\textit{GIVEN}:\\
&\mathcal{V}_t := \{\boldsymbol{\eta}(\mathbf{x},t) \in H^1(\mathcal{B}) \times [0,T];\ \boldsymbol{\eta}(\mathbf{x},t)|_{\partial_u \mathcal{B}} = \dot{\mathbf{u}}^*(\mathbf{x},t)\}\\
&\mathcal{V}_0 := \{\boldsymbol{\eta}(\mathbf{x}) \in H^1(\mathcal{B});\ \boldsymbol{\eta}(\mathbf{x})|_{\partial_u \mathcal{B}} = \mathbf{0}\}\\
&\mathcal{E} := \{\boldsymbol{\mu}(\mathbf{x},t) \in L^2(\mathcal{B})^{n_{\text{dim}} \times n_{\text{dim}}} \times [0,T]\}\\
&\textit{FIND}:\\
&\dot{\mathbf{u}}_t(\mathbf{x}) \equiv \dot{\mathbf{u}}(\mathbf{x},t) : \mathcal{B} \times [0,T] \to \mathbb{R}^{n_{\text{dim}}}; \qquad \dot{\mathbf{u}}_t \in \mathcal{V}_t\\
&\dot{\boldsymbol{\varepsilon}}_t(\mathbf{x}) \equiv \dot{\boldsymbol{\varepsilon}}(\mathbf{x},t) : \mathcal{B} \times [0,T] \to S^{n_{\text{dim}} \times n_{\text{dim}}}; \quad \dot{\boldsymbol{\varepsilon}}_t \in \mathcal{E}
\end{aligned}
\tag{58}
$$

where

$$
\dot{\boldsymbol{\varepsilon}}_t(\mathbf{x}) = \begin{cases} \dot{\boldsymbol{\varepsilon}}_{inj}^{(i)}(\mathbf{x},t) & \forall \mathbf{x} \in \mathcal{B}_{inj}^{(i)}(t), i \in \{1,\ldots,n_{inj}\}\ t \in []_{inj}^{(i)} \\ \boldsymbol{\nabla}^s \dot{\mathbf{u}}_t(\mathbf{x}) & \forall \mathbf{x} \in \mathcal{B} \setminus \mathcal{B}_{inj}(t) \end{cases}
\tag{59}
$$

FULFILLING:

$$
\begin{aligned}
&\int_{\mathcal{B}} \boldsymbol{\nabla}^s \boldsymbol{\eta} : \dot{\boldsymbol{\Sigma}}(\dot{\boldsymbol{\varepsilon}}_t)\, d\mathcal{B} - W^{ext}(\boldsymbol{\eta}, \dot{\mathbf{b}}, \dot{\mathbf{t}}^*) = 0 \qquad \text{(a)}\\
&\int_{\mathcal{B}} \boldsymbol{\mu} : (\dot{\boldsymbol{\varepsilon}}_t - \boldsymbol{\nabla}^s \dot{\mathbf{u}}_t)\, d\mathcal{B} = 0 \qquad \text{(b)}\\
&\forall \boldsymbol{\eta} \in \mathcal{V}_0 \quad \forall \boldsymbol{\mu} \in \mathcal{E}
\end{aligned}
\tag{60}
$$

where, in Eq. (59) $[]_{inj}^{(i)}$ stands for the time interval during which the ith injection is done.

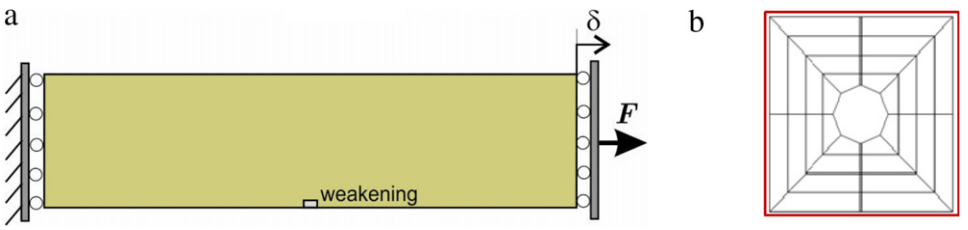

Fig. 9. (DNS) vs. (FE^2) analysis. Tensile stretched strip. (a) Structural scale description. (b) Unit-cell with a central void, enriched with a single vertical cohesive band at the center and discretized by quadrilateral elements.

For the purposes of this work, two different injections are carried out: (a) *weak discontinuity* injection and (b) *strong discontinuity* injection. Their essential features for the present multiscale approach are described in detail in Appendix B.

Remark 3.3. In the context of the strain-injection technique, the localization domain, denoted as $\mathcal{B}_{loc}$ in the proposed multi-scale approach (see Section 2.1 and Fig. 1), becomes the strain-injection domain, $\mathcal{B}_{inj} \equiv \mathcal{B}_{loc}$ (see Fig. 8).

4. Representative simulations

4.1. Consistency of the proposed approach: direct numerical simulation (DNS) versus multi-scale (FE^2) analyses

For the purposes of comparing, the ability of the proposed multi-scale approach to reproduce direct numerical simulation results, the following problems are considered.

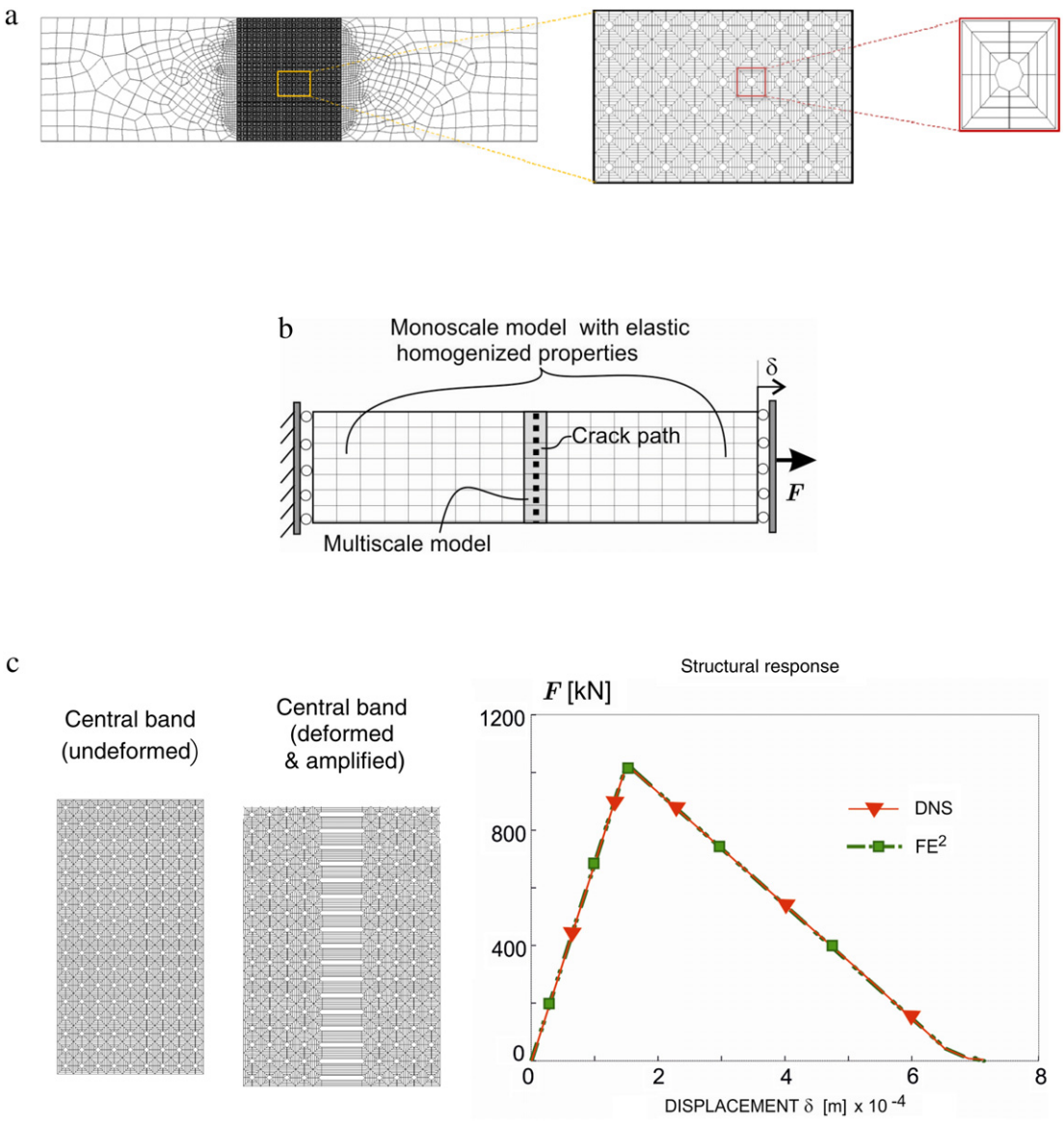

Fig. 10. DNS vs. FE^2 analysis in the tensile stretched strip. (a) Finite element discretization for the DNS analysis. (b) Finite element discretization for the FE^2 analysis and (c) qualitative and quantitative results in both analyzes.

4.1.1. Strip under uniaxial stretching

Let us consider the 2D strip under uniaxial tensile stretching (in plane strain) depicted in Fig. 9(a), loaded by imposing a horizontal homogeneous displacement, δ, at the right edge, while the left edge stays fixed. The length and height of the specimen are, respectively 2 m and 0.5 m.

The material is assumed to exhibit a simple mesostructure consisting of a periodic distribution of voids embedded into a homogeneous elastic matrix. The failure mechanism is represented by vertical cohesive bands connecting the voids. The unit cell of this mesostructure is shown in Fig. 9(b).

The considered material properties are given in Table 1. In order to break the homogeneity of the specimen, that vertical cohesive band placed at the central-lower part of the specimen is weakened to trigger the failure at that point.

In Fig. 10 the considered finite element mesh for the DNS (made of bi-linear quadrilaterals) is shown. A central band of the specimen is finely discretized to capture the considered microstructure. The remaining of the specimen is discretized in a much coarser mesh, whose elements are considered elastic along the whole analysis, so they are

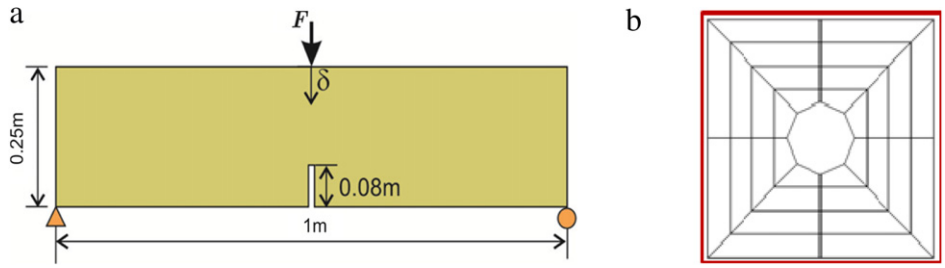

Fig. 11. (DNS) vs. (FE^2) analysis. Three-point bending test. (a) Structural (macroscale) description of the problem. (b) RVE/failure-cell with a central opening enriched with a vertical cohesive band and discretized by quadrilateral elements.

Table 1
Material properties for the matrix and cohesive bands at the micro-scale.

	Young's modulus (GPa)	Poisson ratio	Yield stress (MPa)	Fracture energy (N/m)
Matrix	30	0.15	Elastic	–
Cohesive bands	30	0.15	3	1000

equipped with the homogenized elastic properties stemming from the homogenization of the RVE in Fig. 10(a). For the FE^2 analysis the coarse mesh of quadrilaterals in Fig. 10(b), is used. Again, only the central row of elements are amenable to become inelastic, through a multiscale modeling, whereas the remaining elements are considered elastic with homogenized elastic properties.

The theoretical solution of this problem consists of a central vertical crack, which opens homogeneously (constant crack opening), starting from the weakened point, and resulting in the classical two-branch structural response (see Fig. 10(c)). That solution was exactly captured by both the DNS and the FE^2 solutions, assessing the proposed approach in this case.

4.1.2. Three-point beam bending test

In order to check the ability of the proposed approach to reproduce multi-scale fracture problems with a *propagating crack* at the macro-scale, the classical three point beam bending test, with a central notch, is now considered for a DNS vs. FE^2 comparison.

The considered structural problem and the mesoscale morphology (the same than in the previous case) are displayed in Fig. 11. The considered material properties are the ones displayed in Table 1.

Again, the finite element mesh for the DNS analysis, the discretization for the FE^2 analysis and the comparisons for the structural responses are presented in Fig. 12. It can be noticed the ability of the proposed multi-scale approach to pass DNS vs. FE^2 benchmarks, also in cases of non-homogeneous (variable crack opening) propagating fracture.

4.2. Objectivity analysis of the proposed multiscale model

Objectivity is here understood as the insensitivity of the numerical solutions with respect to: (a) changes in size and bias of the macroscale finite element mesh and, (b) changes of the size and shape of the failure-cell adopted for representing the material micro/mesostructure.

4.2.1. Objectivity with respect to the macroscale mesh size and bias

For the strip under uniaxial stretching in Section 4.1.1, now solved in the multi-scale context, the three meshes depicted in Fig. 13 are considered. For computational saving reasons, the meshes are only modified at the central zone of the strip, i.e. the region where the crack propagates. Meshes (a), (b) and (c) have quadrilateral elements with sizes: $h^e \simeq 0.065\ \mathrm{m}$, $0.035\ \mathrm{m}$ and $0.024\ \mathrm{m}$ respectively. In addition, multiscale modeling is restricted to the central zone, so that the remaining of the specimen is modeled with the one-scale (elastic) homogenized material.

The mesostructure is assumed composed of a matrix, in plane strain state, with voids of circular shape with arbitrary diameter and space distributions. In Fig. 13(a), the adopted failure cell is displayed.

In order to trigger the crack initiation in the central zone of the strip, one element in every mesh is perturbed (in red in Fig. 13), by decreasing in 25% the ultimate stress at the corresponding microscale cohesive bands.

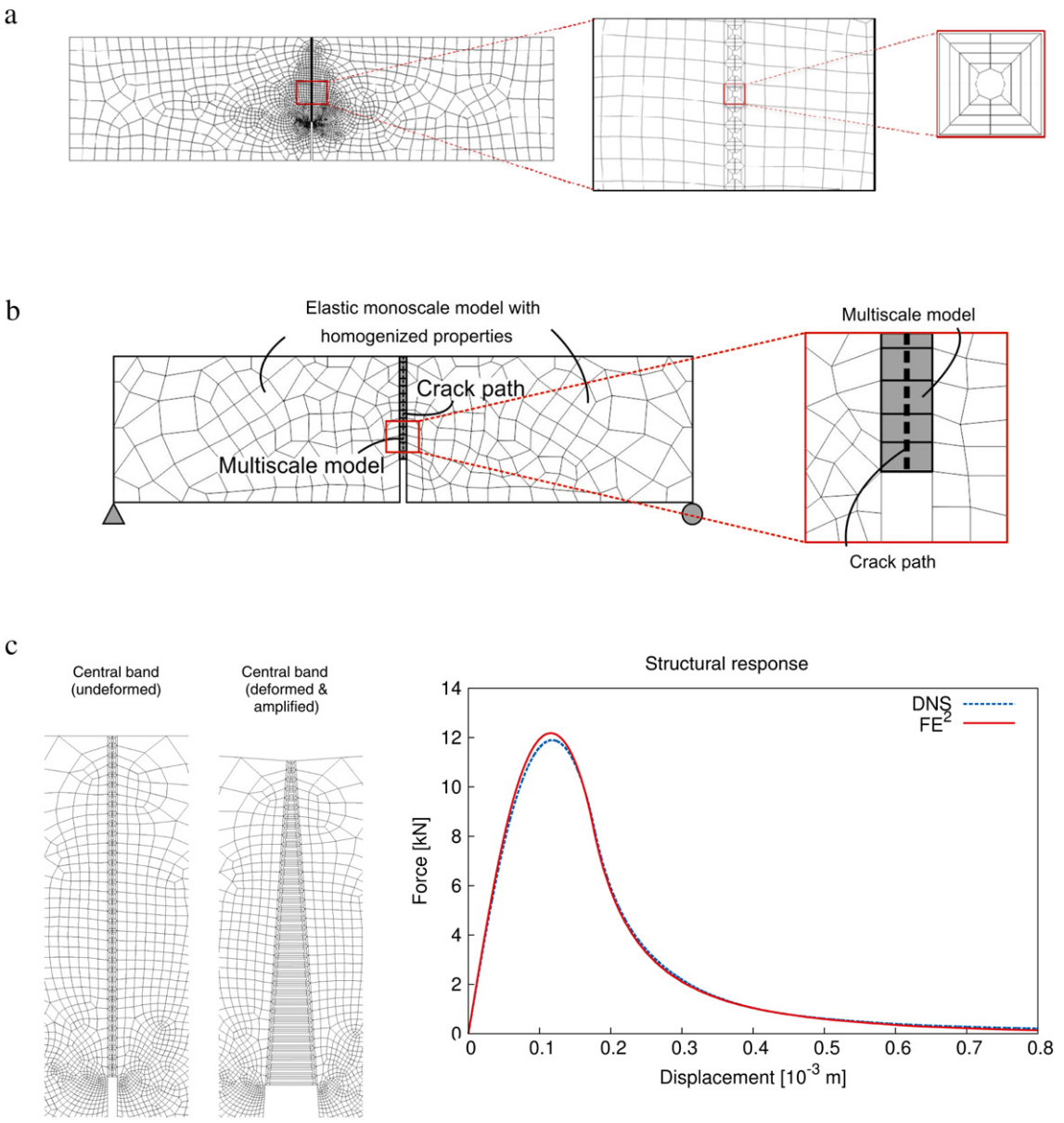

Fig. 12. DNS vs. FE^2 analysis for the three-point bending test. (a) Finite element discretization for the DNS analysis. (b) Macro-scale finite element discretization for the FE^2 analysis (central part) and (c) qualitative and quantitative results for both analyzes.

In Fig. 14 the obtained numerical results are displayed. Fig. 14(a) plots the total load $\boldsymbol{F}$ vs. the horizontal displacement δ for the three meshes. Fig. 14(b) displays the resulting crack path at the end of the analysis for every mesh.

The insensitivity of the structural responses in Fig. 14(a), with respect to meshes of different size and bias, proves the mesh objectivity of the model.

4.2.2. Objectivity with respect to shape and size of the failure-cell

A basic issue in multiscale material modeling is that the response, displayed by cells representing the microscopic morphology of the material, should be independent of changes in shape and size of these cells, provided they are large enough to characterize the material statistically.

In order to check this specific issue using the proposed approach, the test sketched in Fig. 15 is done. A set of different cells is adopted for characterizing the material response. They are constructed from the repetition, in the horizontal and vertical directions, of a basic cell (see Fig. 15(b)).

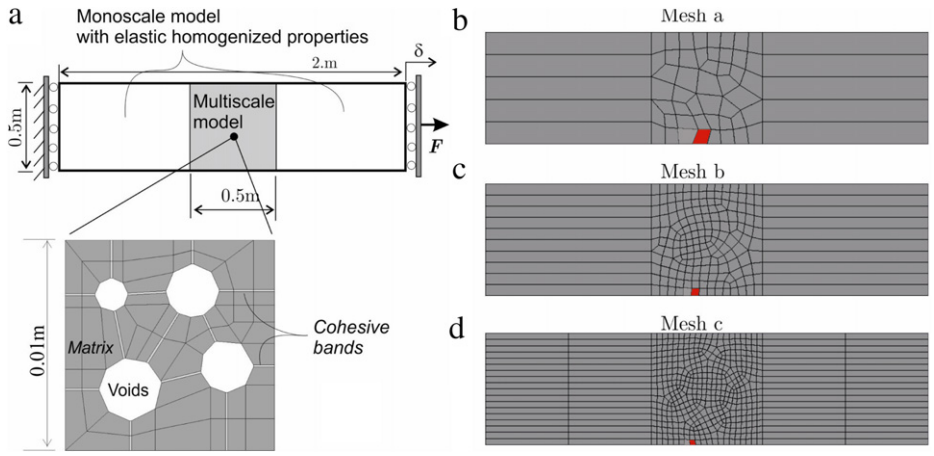

Fig. 13. Objectivity with respect to changes of the finite element mesh at the macro-scale. (a) Multiscale model and failure-cell; (b) coarse discretization (58FE, $h^e \simeq 0.065$ m); (c) medium discretization (192FE, $h^e \simeq 0.035$ m); (d) fine discretization (504 FE, $h^e \simeq 0.024$ m). (For interpretation of the references to color in this figure, the reader is referred to the web version of this article.)

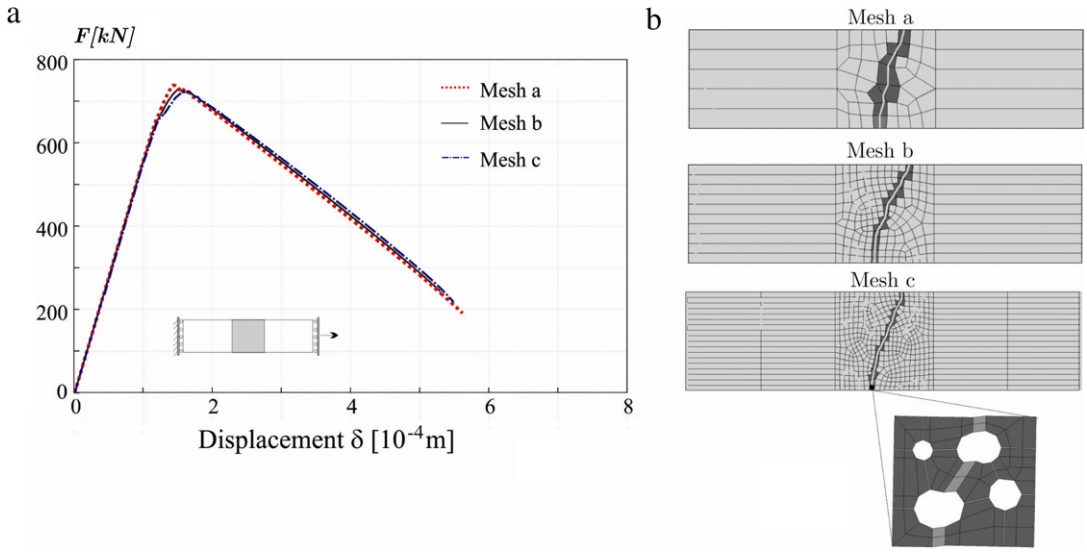

Fig. 14. Objectivity with respect to changes of the finite element mesh at the macro-scale: (a) reaction force vs. end-displacement; (b) crack path (for meshes (a), (b) and (c)) and deformed mesoscopic cell displaying the macroscopic failure mechanisms (activated cohesive bands).

The macroscale structural problem and the material properties are the same than in Section 4.2.1: a strip undergoing tensile loading with multiscale modeling restricted to the central zone (see Fig. 15(a)).

The mesostructure consists of a matrix with a periodic array of cylindrical voids, arranged in a squared pattern of size $h = 0.001$ m, see Fig. 15(a). In order to represent this mesostructure, the unit mesoscopic cell, depicted in Fig. 15(b) and denoted (1×1), is used first. Then, two alternative cells, obtained by repeating cell (1×1) in the horizontal and vertical directions, denoted as (2×1) and (2×2) respectively in Fig. 15(a), are additionally used for the multiscale analysis. Under the chosen loading conditions and microstructure failure cell, the microscale failure mode consists, in the three cases, of the activation of a single vertical column of cohesive bands (see Fig. 15(b)), which translates in a macroscale vertical crack at the central part of the strip (see Fig. 15(a)).

Fig. 15(c) displays the structural response obtained with the three considered mesoscopic cells, (1×1), (2×1) and (2×2), in terms of the load vs. horizontal displacement response. The almost indistinguishable results for the three cases assess the objectivity of the response. In the achievement of these results, it is again emphasized the key role played by the regularization of the kinematics in Eq. (35), in terms of the microscopic characteristic length ℓ_μ (in

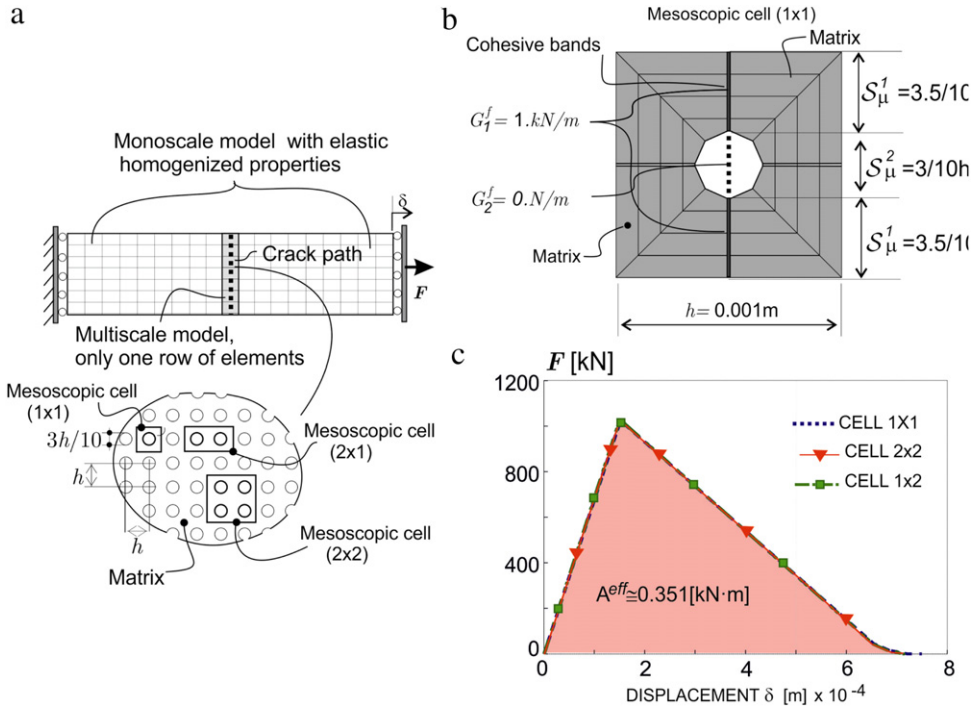

Fig. 15. Objectivity with respect to changes in the failure-cell. (a) Test description; (b) microcell (1 × 1); (c) Structural responses (load vs. horizontal displacement curves) for mesoscopic failure cells: 1 × 1, 2 × 1 and 2 × 2.

Eq. (51)(b)). Indeed, this length takes different values in each case, i.e.: $\ell_\mu = h$ for microcell (1 × 1), and $\ell_\mu = 2h$ for microcells (2 × 1) and (2 × 2).

4.2.3. Fracture energy

Next, the value of the macroscale fracture energy, $G^f(\mathbf{x})$, obtained from the analyzes, is compared with the theoretical (analytical) one in Eq. (46). In order to induce a straight macroscale crack-path with an exactly measurable length, the strip is solved with a vertical structured mesh. As shown in Fig. 15(a), only one row of elements at the central zone of the strip is endowed with a multiscale model. Micro-cell (1 × 1) is taken and a vertical macroscopic crack develops. The material parameters are the same than in the previous case.

Taking into account that the inner void in the failure cell can be considered as a cohesive band with a null fracture energy and length $meas(\mathcal{S}^{void}_{\mu,coh}) = 3/10h$, the *average value of the cohesive fracture energy along the developed microscopic failure mechanism* is evaluated (see Eq. (46) and Fig. 15(b)) as:

$$G^f_{analytical} \equiv \overline{G^f_\mu(\mathbf{y})}_{\mathcal{S}_\mu} = \frac{7/10h}{h} G^f_\mu = 700\ \mathrm{N/m} \tag{61}$$

this supplying the analytical value of the overall (macroscopic) fracture energy, $G^f_{analytical}$. In addition, the numerically obtained value of the overall fracture energy, $G^f_{numerical}$, can be extracted from the area, A^{eff}, under the structural force–displacement curve in Fig. 15(c) i.e.:

$$G^f_{numerical} = \frac{A^{eff}}{length(\mathcal{S}) \times thickness} = \frac{351\ \mathrm{N\ m}}{0.5\ \mathrm{m} \times 1\ \mathrm{m}} = 702\ \mathrm{N/m} \tag{62}$$

which matches the theoretical value in Eq. (61).

4.3. Multiscale model assessment: Nooru-Mohamed test

The experimental test on concrete specimens reported by Nooru-Mohamed [46], and sketched in Fig. 16, is now used to assess the ability of the proposed approach to model *propagating material failure at two scales*. The adopted

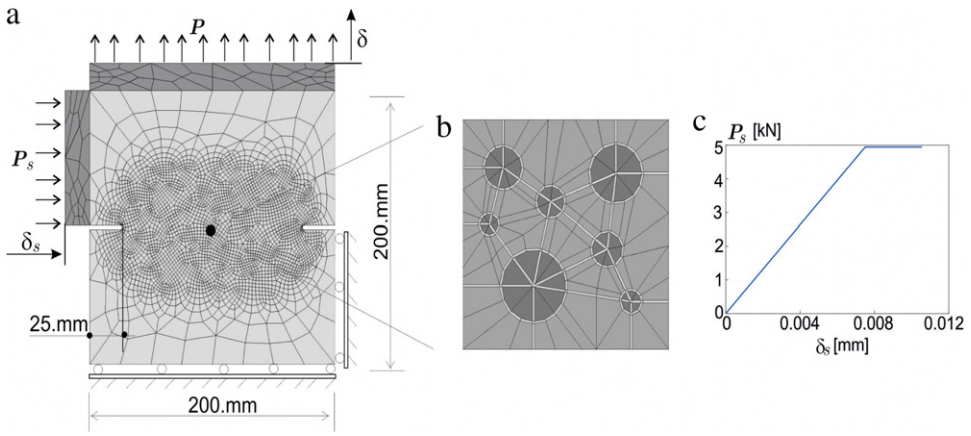

Fig. 16. Nooru-Mohamed test (a) mesh of the specimen with 3464 quadrilateral finite elements; (b) mesoscopic cell and (c) applied shear force, $\boldsymbol{P}_S$, history as a function of the horizontal displacement of the left edge of the specimen δ_s.

Table 2
Nooru-Mohamed test. Material properties.

	Young's modulus (GPa)	Poisson ratio	Ultimate stress (MPa)	Fracture energy (N/m)
Matrix	21	0.15	Elastic	–
Cohesive bands	21	0.15	3	20
Aggregates	100	0.15	Elastic	–

failure cell is presented in Fig. 16(b). For computational cost reasons, the cell crudely represents the morphology of concrete as a matrix (mortar) with some inclusions (aggregates) of different sizes. Therefore, no attempt has been done to represent the statistically distribution of heterogeneities and failure characteristics, at the mesoscopic level, observed in standard concretes. The interest is restricted to assess the ability of the numerical model to simulate a rather complex structural behavior, involving propagating material failure in two scales, and to compare the results with the wide set of experiences available for this benchmark using *single scale phenomenological approaches*.

4.3.1. Geometrical features and loading paths

The specimen, of size 200 mm $\times$ 200 mm and 50 mm of thickness, with two notches (25 mm depth and 0.125 depth/with ratio) is depicted in light gray in Fig. 16(a). The dark gray part of the structure is made of steel. It is considered infinitely rigid and used to apply the different loads in a distributed form.

Loading consists of a shear force applied in a nearly elastic regime, until reaching the value $\boldsymbol{P}_S = 5\ (\mathrm{kN})$ and remaining constant afterwards. Subsequently, an increasing vertical uniformly distributed load $\boldsymbol{P}$ is superposed (see Fig. 15(a)–(c)). During the first loading stage (shear force application), the left and top steel parts are constrained to remain vertical and horizontal, respectively.

4.3.2. Material properties description

The mesoscopic failure cell, depicted in Fig. 16(b), crudely represents a concrete-like material at the mesoscale (matrix/aggregates). Light gray regions represent cohesive/failure bands, medium gray zone stands for the cement-like matrix and dark gray regions represents aggregates (the cohesive bands into the aggregates are inhibited to failure). Material properties of the cell are summarized in Table 2.

4.3.3. Crack propagation result

In order to analyze the ability of the proposed approach for capturing the crack evolution, attention is first focused on the macroscopic scale. In Fig. 17, the iso-displacement contours at the end of the simulation depict highly localized strain zones representing two evolving cracks, which initiate at the notch roots. A slight crack curvature can be observed at the bottom crack, and roughly, both cracks can be viewed as straight surfaces with an inclination of about 10°. In spite of the commented crude representation of the microstructure, the obtained macroscale crack pattern fairly coincides with the results reported in the experiment [46].

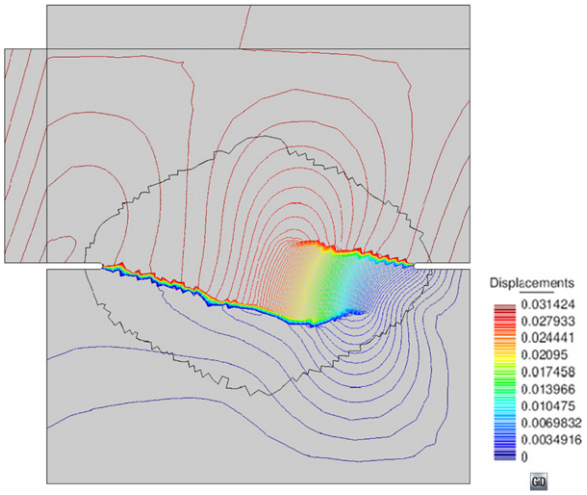

Fig. 17. Nooru-Mohamed test. Iso-lines of the macroscopic vertical displacements. Grouping of iso-lines indicates a jump in the displacement field and, therefore, signals the crack path.

The series of snapshots in Fig. 18 show the evolution of the strain injected embedded weak discontinuity region (finite elements in dark gray), and the finite elements with injected embedded strong discontinuities (in red). The weak discontinuity region spreads across a wide zone, forming a bulb-like zone at the tip of each crack endowed with highly flexible elements, suitable to capture localized strains and their propagation. On this basis, the crack-path-field technique in Box 3.1, supplies the crack-path, as the zero level set of the crack path field μ_t, which, in turn, defines the proper position (in every Γ_t-crossed element) of the injected strong discontinuity mode.

Fig. 19 displays additional results of the numerical solution. The crack path obtained at the end of analysis is shown in Fig. 19(a), which is compared with the experimental one. The structural response in terms of vertical loads vs. vertical displacement of the top specimen is shown in Fig. 19(b).

Classical effects of a propagating crack on the structural response are displayed by the softening character of the structural response curve in spite of the very crude representation of the material through the failure cell.

Next, attention is focused on the behavior of the mesoscopic cell at the singular Gauss point, $\mathbf{x}_{sing}^{(e)}$ (the one capturing the mesoscopic failure, see Fig. 27, and Table 3 in Appendix B) for different elements at the micro-scale. Fig. 20 depicts a zoom of the left notch, showing the crack-path (line in blue) and the normal vector, $\mathbf{n}^{(e)}$, used for embedding the strong discontinuity kinematics in each finite element (see Fig. 29, in Appendix B). A number of elements have been selected to analyze the mesoscopic results. For every selected element, the corresponding deformed failure cell, at the end of analysis, is shown. There, it can be checked that those elements crossed by the crack path display a clear mesoscopic failure mode characterized by a (regularized) displacement jump, in a set of cohesive elements, which is constant for all of them as predicted by the theoretical results (see Remark 2.6). The one down-left the notch, though nearby the crack path, is not crossed by it and, as expected, displays a smooth deformation mode.

4.3.4. Macro-/meso-scale relationship

The effects of distribution and richness of possible failure mechanisms at the mesoscopic cell, and their effects, on the crack patterns at the macro-scale and on the structural response, are now examined.

For this purpose, the original cell in Fig. 16(b) is considered, together with two additional failure cells (see Fig. 21). They keep the original material morphology, in terms of matrix and inclusions, but considerably reduce the number of possible failure mechanisms (by locking the inelastic behavior of appropriated cohesive bands).

In case of Fig. 21(b) the only possible failure mechanism is almost horizontal, whereas in Fig. 21(c), it is oblique.

Fig. 22 displays the macroscopic crack pattern obtained with each of these cells.

Fig. 23 displays the structural responses in terms of load vs. vertical displacement, provided by the three cells in Fig. 21. As it can be expected, locking of failure modes due to removal of cohesive bands at the mesoscopic scale leads to the following response: the poorer is the mesoscopic cell description the higher is the structural strength.

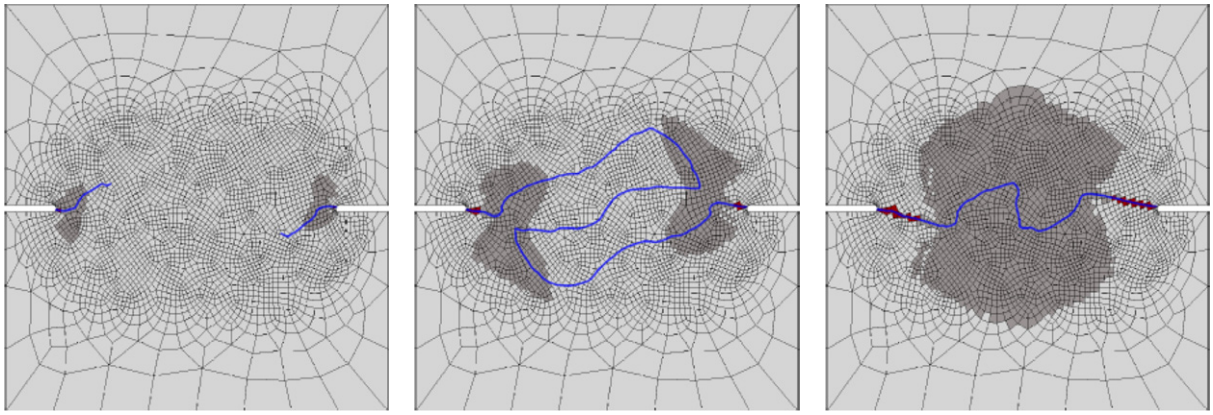

(a) $\delta = 0.011$ mm. (b) $\delta = 0.014$ mm. (c) $\delta = 0.018$ mm.

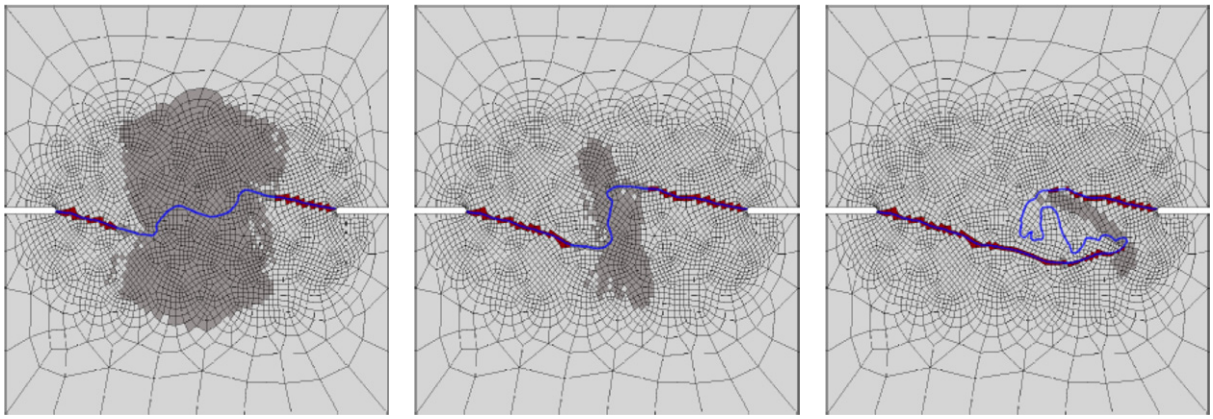

(d) $\delta = 0.019$ mm. (e) $\delta = 0.020$ mm. (f) $\delta = 0.025$ mm.

Fig. 18. Nooru-Mohamed test. Evolution of injected weak discontinuity region (in dark gray), zero-level set of the crack path field (lines in blue) and finite elements injected with strong discontinuity (in red). (For interpretation of the references to color in this figure legend, the reader is referred to the web version of this article.)

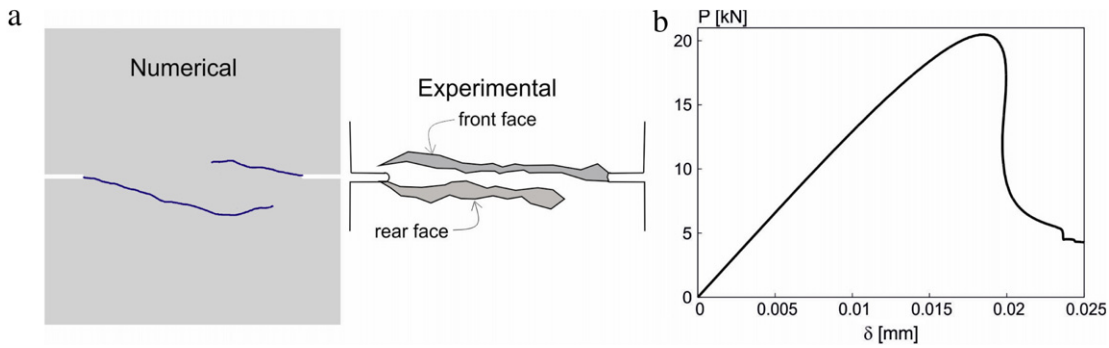

Fig. 19. Nooru-Mohamed test. Characterization of the structural response. (a) Numerical and experimental crack path; (b) Axial force P as a function of the axial displacement δ.

5. Concluding remarks

Along this work, a new approach to two-scale modeling of material failure, based on computational homogenization (FE^2), has been presented. The specific features of the approach rely on two main aspects: (a) the adopted

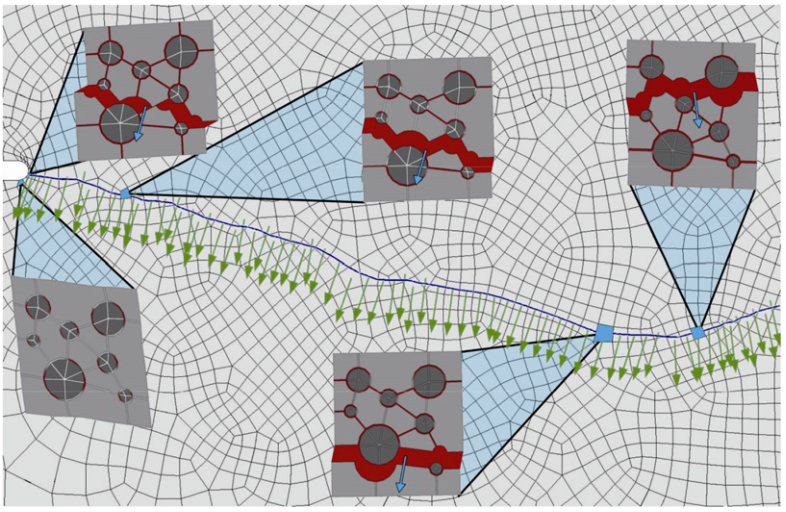

Fig. 20. Nooru-Mohamed test. Deformed (amplified) failure cells, for several elements at the macroscale at the end of the analysis, displaying the activated failure mechanism (in red). (For interpretation of the references to color in this figure legend, the reader is referred to the web version of this article.)

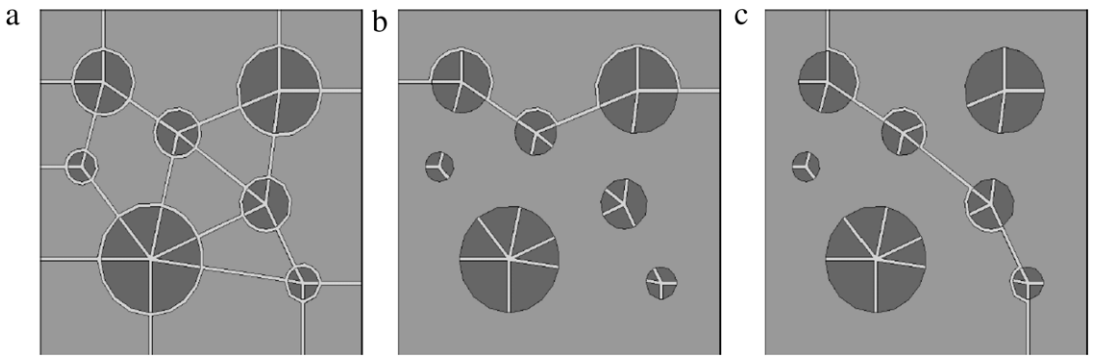

Fig. 21. Nooru-Mohamed test. Mesoscale cells with different cohesive-band patterns. (a) Original failure cell; (b) Failure cell allowing only a quasi-horizontal failure mechanism; (c) Failure cell allowing an oblique failure mechanism.

continuum setting for representation of the fracture, based on the Continuum Strong Discontinuity Approach (CSDA) and developed by the authors in previous works [35], and, (b) a standard (continuum) format of the computational homogenization procedure.

The resulting framework is endowed with the following properties:

(1) Minimally invasive nature with regard to procedures well established in the literature on multiscale modeling of materials.[10] In fact,
- in terms of the *computational homogenization procedure*: the proposed approach displays no substantial difference with respect to the ones used for smooth (continuous) problems. A RVE/failure cell is defined at the lower (micro/meso scale) from which stresses and strains are homogenized in a classical continuum format to obtain a, point-wise defined, stress–strain constitutive model at the macro-scale.
- In terms of *material failure propagation*: existing algorithms for mono-scale crack propagation modeling can be easily extended to the multi-scale case. In this sense, the authors' experience in extending the crack-path-field and strain injection techniques [31] previously developed for the mono-scale case to the present multiscale case, should be extensible to other families of crack-propagation techniques.

[10] In this work, the modern framework of *variational multi-scale formulation* [16,17] has been considered as the best reference.

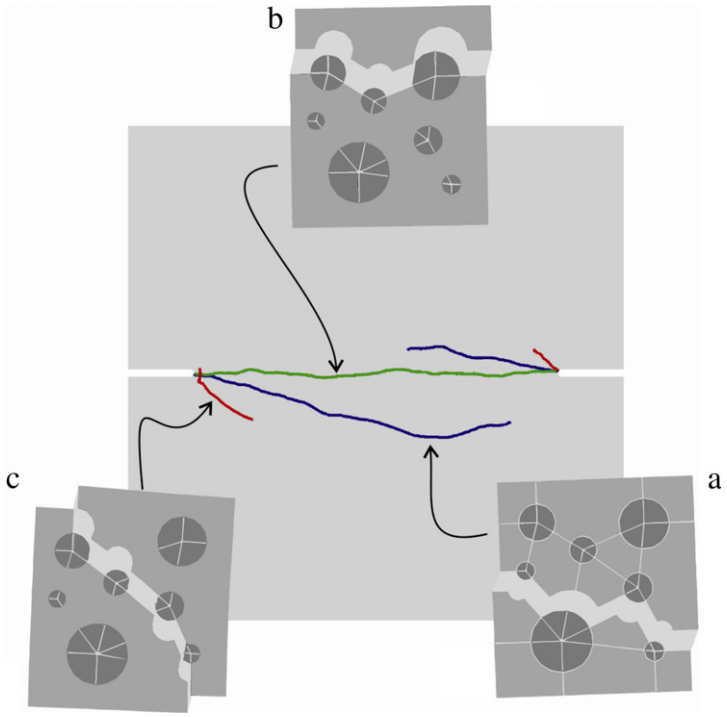

Fig. 22. Nooru-Mohamed test. Crack paths simulated according with the adopted mesoscopic cell.

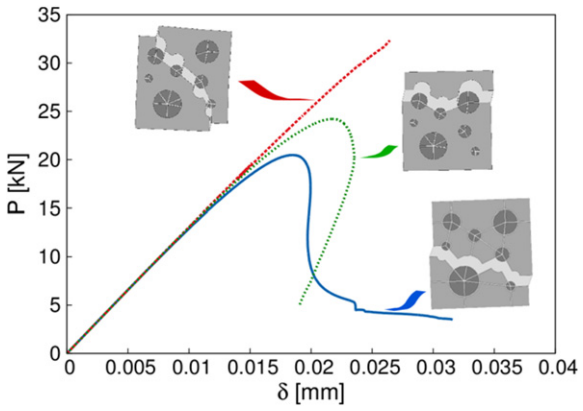

Fig. 23. Nooru-Mohamed test. Structural responses for different meso-cells.

(2) Consistency of the homogenized results. This has been checked by comparison, for a number of representative cases, of the (FE^2) results and the ones obtained by direct numerical simulation (DNS).
(3) Objectivity character (independence) of the results in terms of:
- finite element mesh size and bias, at the macro-scale
- failure-cell (size and shape) at the micro/meso-scale.

A key issue in this achievements is the use of a characteristic length, which naturally emerges from theoretical considerations on the homogenized constitutive model, to regularize the weak/strong discontinuity kinematics at the macro-scale in the context of the CSDA.

The performance of the proposed approach has been assessed by a number of examples. They go beyond the, simple, homogenization-based assessment (focusing only on the obtained homogenized macro-scale constitutive equation), but towards a much more ambitious goal: modeling the fracture onset and propagation at the macro-scale

based on the, simpler, in the physics, but more complex in the morphology, micro-scale representations, and the corresponding structural action–response.

However, the authors are aware that realistic multiscale representations of material failure require the use of more sophisticated microscopic morphologies, allowing complex failure mechanisms at the micro-scale [47]. In this sense, realistic multiscale analysis of material failure, including the extension to 3D cases, face a great challenge: the enormous involved computational cost. It is well known that the algorithmic complexity of multiscale analysis leads to the so-called *tyranny of the scales* [48], which makes computations unaffordable, even by resorting to intensive computation procedures (parallel computing), for relatively crude representations of the material morphology and coarse finite element meshes at the macro-scale. A possible remedy for this drawback could stem from the development and use of high performance reduced order modeling (HPROM) techniques for multiscale problems. In a recent work [49] the authors have developed some specific and efficient algorithms for the smooth (continuous) case. Extension to the, much more challenging, non-smooth cases, like multiscale material failure, is a subject of ongoing research.

Finally, some extensions of the material representation at the micro-scale, beyond the one presented here, seem to fit trivially into the proposed approach at the only cost of the modification of some specific ingredients of the model. For instance:

- Inclusion of non-linear hardening behavior, before the onset of material failure can be trivially included in the considered damage model.
- Consideration of other families of constitutive behavior, like plasticity, rate dependence etc., can be simply done by including these effects in the basic constitutive model.
- The use of cohesive bands to model failure at the micro-scale is neither a compulsory ingredient of the approach. Using other propagating crack models at the micro-scale, either based on continuum strain-localization methods (Continuum Strong Discontinuity Approach, non-local models or gradient-regularized models) or discrete methods (based on cohesive interfaces equipped with traction–separation laws) where the crack onset and propagation is not predefined (just as it is done here at the macro-scale) also fits in the approach at the cost of some additional sophistication.

These and other issues, concerning the extension of the proposed approach, are subject of ongoing research and they will be addressed in future works.

Acknowledgments

The research leading to these results has received funding from the European Research Council under the European Union's Seventh Framework Programme (FP/2007–2013)/ERC Grant Agreement n. 320815, Advanced Grant Project COMP-DES-MAT (Advanced tools for computational design of engineering materials).

The funding received from the Spanish Ministry of Economy and Competitiveness through the National Research Plan 2014 project: MAT2014-60919-R is also gratefully acknowledged.

Appendix A. Removal of spurious failure modes

When the fundamental localized solution is perturbed, in terms of the micro-fluctuations in Eq. (22)(a), by increments

$$\dot{\tilde{\mathbf{u}}}^{*}_{\mu}(\mathbf{y}) = \mathcal{H}_{\mathcal{B}_{\mu,coh}}(\mathbf{y})\,\dot{\boldsymbol{\beta}}^{*}_{\mu}(\mathbf{y}); \quad \dot{\tilde{\mathbf{u}}}_{\mu}(\mathbf{y}) \in \boldsymbol{\mathcal{V}}_{\mu} \tag{63}$$

(see Eq. (16)), $\dot{\boldsymbol{\beta}}^{*}_{\mu}(\mathbf{y},t)$ fulfilling

$$\begin{aligned} &\dot{\boldsymbol{\beta}}_{\mu}(\mathbf{y}) \neq \mathbf{0} \quad \text{for some } \mathbf{y} \in \mathcal{S}_{\mu} && \text{(a)} \\ &\dot{\boldsymbol{\varepsilon}}^{(i)}(\mathbf{x},t) = \frac{1}{\ell_{\mu}}\overline{(\dot{\boldsymbol{\beta}}_{\mu}(\mathbf{x},\mathbf{y}) \otimes^{s} \mathbf{n}_{\mu}(\mathbf{x},\mathbf{y}))}^{\mathcal{S}_{\mu}} = \mathbf{0} && \text{(b)} \end{aligned} \tag{64}$$

a bifurcation in the solution space $\boldsymbol{\sigma}$–$\boldsymbol{\varepsilon}$, may appear. Indeed, in this case, the fundamental branch is characterized by the rate equation (see Eq. (30)(a)):

$$\dot{\boldsymbol{\sigma}}^{(1)}(\mathbf{x},t) = \overline{\boldsymbol{\mathcal{C}}} : [\dot{\boldsymbol{\varepsilon}}(\mathbf{x},t) + \dot{\boldsymbol{\chi}}(\mathbf{x},t) - \dot{\boldsymbol{\varepsilon}}^{(i)}(\mathbf{x},t)] = \boldsymbol{\mathcal{C}}^{tang}_{hom}(\boldsymbol{\varepsilon}) : \dot{\boldsymbol{\varepsilon}}(\mathbf{x},t). \tag{65}$$

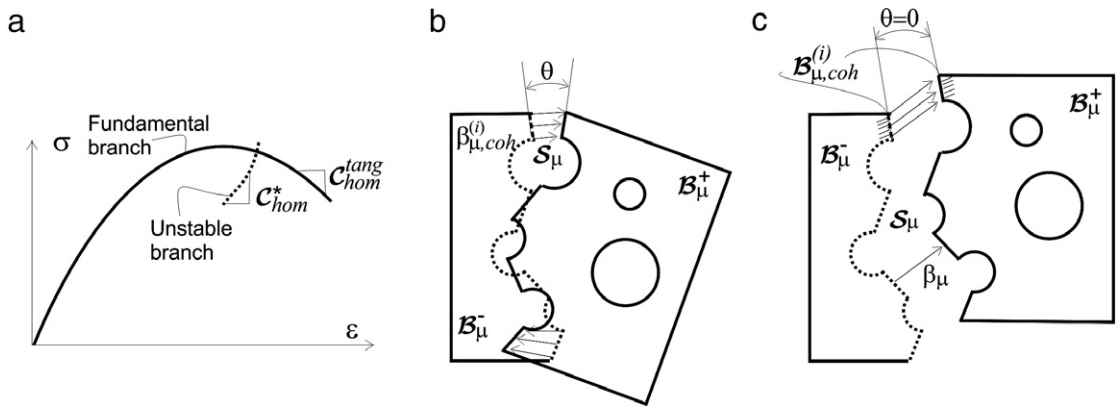

Fig. 24. (a) Instability of the homogenized, **σ**–**ε**, solution, (b) unstable failure mechanism at the micro-scale, and (c) stabilized failure mechanism, restraining rotation.

On the other hand, the perturbed solution, $\dot{\boldsymbol{\sigma}}^{(2)}(\mathbf{x},t)$, is characterized by Eqs. (64); therefore, $\dot{\boldsymbol{\varepsilon}}^{(i)}(\mathbf{x},t)=\mathbf{0}$ so that substitution in Eq. (30)(a) yields:

$$\dot{\boldsymbol{\sigma}}^{(2)}(\mathbf{x},t)=\overline{\boldsymbol{\mathcal{C}}}:(\dot{\boldsymbol{\varepsilon}}(\mathbf{x},t)+\dot{\boldsymbol{\chi}}^{*}(\mathbf{x}))=\underbrace{\overline{\boldsymbol{\mathcal{C}}}:[\mathbf{I}+\mathcal{M}(\boldsymbol{\varepsilon})]}_{\boldsymbol{\mathcal{C}}^{*}_{hom}}:\dot{\boldsymbol{\varepsilon}}(\mathbf{x},t)=\boldsymbol{\mathcal{C}}^{*}_{hom}:\dot{\boldsymbol{\varepsilon}}(\mathbf{x},t). \tag{66}$$

Therefore, the fundamental and perturbed solutions in Eqs. (65) and (66) are characterized by different tangent moduli, $\boldsymbol{\mathcal{C}}^{tang}_{hom}\neq\boldsymbol{\mathcal{C}}^{*}_{hom}$ (see Fig. 24(a)).

Typically, this situation arises when the perturbation, $\dot{\tilde{\mathbf{u}}}^{*}_{\mu}(\mathbf{y})$ in Eq. (63), consists of a rigid body motion of $\mathcal{B}^{+}_{\mu}$ with respect to $\mathcal{B}^{-}_{\mu}$ (see Fig. 24(b)) i.e.:

$$\dot{\tilde{\mathbf{u}}}^{*}_{\mu}(\mathbf{y})=\mathcal{H}_{\mathcal{B}_{\mu,k}}(\mathbf{a}+\boldsymbol{\Omega}(\boldsymbol{\theta})\cdot\mathbf{y})\in\boldsymbol{\mathcal{V}}_{\mu} \tag{67}$$

where $\mathbf{a}(t)$ stands for a, spatially constant, shift and $\boldsymbol{\Omega}(\boldsymbol{\theta}(t))$ is a, skew-symmetric, rotation tensor with axial vector $\boldsymbol{\theta}(t)$. From Eqs. (16) and (67):

$$\begin{aligned}\int_{\Gamma_{\mu}}(\dot{\tilde{\mathbf{u}}}^{*}_{\mu}\otimes\mathbf{v}_{\mu})^{S}d\Gamma&=\int_{\Omega_{\mu}}\boldsymbol{\nabla}\otimes^{S}\dot{\tilde{\mathbf{u}}}^{*}_{\mu}(\mathbf{y},t)d\Omega_{\mu}\\&=\int_{\Omega_{\mu}}\mathcal{H}_{\mathcal{B}_{\mu,k}}\underbrace{(\boldsymbol{\Omega}+\boldsymbol{\Omega}^{T})}_{=\mathbf{0}}d\Omega_{\mu}+\int_{\mathcal{S}_{\mu}(\mathbf{x})}\mathbf{n}_{\mu}(\mathbf{y})\otimes^{S}(\mathbf{a}+\boldsymbol{\Omega}(\boldsymbol{\theta})\cdot\mathbf{y})\,d\mathcal{S}_{\mu}=0.\end{aligned} \tag{68}$$

Eq. (68) is a homogeneous system of linear equations in the unknowns $\{\mathbf{a},\boldsymbol{\theta}\}$, which can be written as:

$$\begin{aligned}&\underbrace{\int_{\mathcal{S}_{\mu}(\mathbf{x})}\mathbf{n}_{\mu}(\mathbf{y})d\mathcal{S}_{\mu}}_{\mathbf{r}(\mathcal{S}_{\mu})}\otimes^{S}\mathbf{a}-\underbrace{\int_{\mathcal{S}_{\mu}(\mathbf{x})}(\mathbf{n}_{\mu}(\mathbf{y})\otimes^{S}\mathbf{y})d\mathcal{S}_{\mu}}_{\mathbf{L}(\mathcal{S}_{\mu})}\times\boldsymbol{\theta}=\mathbf{0}\qquad\text{(a)}\\&\rightarrow\mathbf{r}(\mathcal{S}_{\mu})\otimes^{S}\mathbf{a}+\mathbf{L}(\mathcal{S}_{\mu})\times\boldsymbol{\theta}=\mathbf{0}\qquad\text{(b)}\end{aligned} \tag{69}$$

which can be rephrased as:

$$[\mathbf{G}(\mathcal{S}_{\mu})]\cdot[\mathbf{a},\boldsymbol{\theta}]^{T}=\{\mathbf{0}\} \tag{70}$$

where $[\mathbf{G}(\mathcal{S}_{\mu})]$ is the corresponding matrix of coefficients, depending on the corresponding activated failure mechanism $\mathcal{S}_{\mu}$. If $[\mathbf{G}(\mathcal{S}_{\mu})]$ is rank deficient, Eq. (70) has non-trivial solutions, $\mathbf{a}^{*},\boldsymbol{\theta}^{*}$, each one characterizing an unstable mode $\dot{\tilde{\mathbf{u}}}^{*}_{\mu}(\mathbf{y})$ in Eq. (67). Inspection of Eq. (69) reveals that if the rotation angle is imposed to be zero ($\boldsymbol{\theta}=\mathbf{0}$)

then, the equation becomes

$$\begin{cases} \mathbf{r}(\mathcal{S}_\mu) \otimes^S \mathbf{a} = \mathbf{0} \\ \mathbf{r}(\mathcal{S}_\mu) = \displaystyle\int_{\mathcal{S}_\mu(\mathbf{x})} \mathbf{n}_\mu(\mathbf{y}) d\mathcal{S}_\mu \neq \mathbf{0} \end{cases} \Rightarrow \mathbf{a} = \mathbf{0} \tag{71}$$

and system (70) possesses only the trivial solution $\mathbf{a}^* = \mathbf{0}, \boldsymbol{\theta}^* = \mathbf{0}$. This result is exploited in the proposed technique to remove those modes described next.

Consistently with the fundamental result in Remark 2.6 ($\dot{\boldsymbol{\beta}}_\mu(\mathbf{x},\mathbf{y},t) = \dot{\boldsymbol{\beta}}_\mu(\mathbf{x},t),\ \forall t \geq t_B$) we impose on a selected set, $\mathcal{B}_{\mu,restr} = \bigcup_{i=1}^{n_{rest}} \mathcal{B}^{(i)}_{\mu,restr}$, $\mathcal{B}_{\mu,restr} \subset \mathcal{B}_{\mu,coh}$, of n_{restr} cohesive bands (see Fig. 2) the following restriction:

$$\dot{\boldsymbol{\beta}}^{(i)}_\mu(\eta(\mathbf{y}),t)\Big|_{\mathbf{y}\in\mathcal{B}^{(i)}_{\mu,restr}\subset\mathcal{B}_{\mu,restr}} \equiv [\![\dot{\tilde{\mathbf{u}}}_\mu(\xi(\mathbf{y}),\eta(\mathbf{y}),t)]\!]^+_- = \dot{\boldsymbol{\beta}}^{(i)}_\mu(t) \quad i=\{1,..,n_{restr}\};\ \forall t \geq t_B. \tag{72}$$

In Eq. (72) notation $[\![(\cdot)(\xi,\eta)]\!]^+_- \equiv (\cdot)(\xi,\eta)|_{\xi=k} - (\cdot)(\xi,\eta)|_{\xi=0}$ stands for the *apparent jump* between both sides of the cohesive band, see Fig. 2. Restriction in Eq. (72) translates into *clamping* (precluding rotation but allowing a constant fluctuation jump) domain $\mathcal{B}^+_\mu$ with respect to domain $\mathcal{B}^-_\mu$, by means of the restriction on the cohesive band $\mathcal{B}^{(i)}_{\mu,coh}$ (see Fig. 24(c)). This is enough to *remove* the instability modes *for any failure mechanism containing the cohesive band* $\mathcal{B}^{(i)}_{\mu,coh}$.[11]

Moreover, for practical purposes, and due to the small bandwidth k of the bands, Eq. (65) is imposed at the beginning of the analysis, and in total (non-rate) form, without substantial consequences in the results, i.e.:

$$\boldsymbol{\beta}^{(i)}_\mu(\eta(\mathbf{y}),t)\Big|_{\mathbf{y}\in\mathcal{B}^{(i)}_{\mu,coh}\subset\mathcal{B}_{\mu,restr}} \equiv [\![\tilde{\mathbf{u}}_\mu(\xi(\mathbf{y}),\eta(\mathbf{y}),t)]\!]^+_- = \boldsymbol{\beta}^{(i)}_\mu(t) \quad i=\{1,..,n_{restr}\};\ \forall t. \tag{73}$$

In this context, it can be readily proven that if any activated failure mechanism contents, at least, one of the cohesive bands of set $\mathcal{B}_{\mu,restr}$ in Eq. (73), than Eq. (53)(b) has only the trivial solution $\dot{\boldsymbol{\beta}}_\mu(\mathbf{y}) = 0$ and the instability does not appear. From the authors' experience, to prevent instabilities for any possible failure mechanism it is sufficient to include in the set $\mathcal{B}_{\mu,restr}$ *all cohesive bands intersecting the boundary of the failure cell* $\mathcal{B}_\mu$.[12]

As for the implementation of Eq. (73), the restriction can be *strongly imposed*, as an internal constraint in the elemental nodes, or *weakly imposed* via a penalty formulation. From the authors' experience, results are the same for both cases, though the second method turns out to be less code-invasive than the first one.

Appendix B. Strain injection techniques in multiscale problems

B.1. Weak discontinuity injection. Constant stress/discontinuous strain mode

B.1.1. Dipole generalized function

Let us denote $\chi_{\mathcal{S}}(\mathbf{x})$ as the *dipole generalized function* (generalized derivative of the Dirac's delta function) fulfilling

$$\int_{\mathcal{B}} \chi_{\mathcal{S}}\, \phi(\mathbf{x}) d\mathcal{B} = \int_{\mathcal{S}} [\![\phi]\!] d\mathcal{S} \tag{74}$$

for any sufficiently regular function, $\phi(\mathbf{x})$ exhibiting a jump, $[\![\phi]\!]$, across the discontinuity path, $\mathcal{S}$. Let us also define a two-parameter (h,k) sequence, $\chi^{h,k}_{\mathcal{S}}(\mathbf{x})$, in a band of thickness ℓ as:

$$\chi^{h,k}_{\mathcal{S}}(\mathbf{x}) = \begin{cases} -\dfrac{1}{h-k} & \mathbf{x} \in \mathcal{B}_{reg} \\ \dfrac{1}{k} & \mathbf{x} \in \mathcal{B}_{sing} \\ 0 & \text{otherwise} \end{cases} \tag{75}$$

[11] If quadrilateral finite elements are used for modeling the cohesive bands, Eq. (72) is equivalent to impose the fluctuation jump $[\![\dot{\tilde{\mathbf{u}}}_\mu(\xi,\eta)(\mathbf{y}_j,t)]\!]^+_-$ to be the same for all nodes, j, placed in the η direction of the selected element (see Fig. 6).

[12] The fact that any failure mechanism intersects the boundary of the failure cell is exploited for this statement.

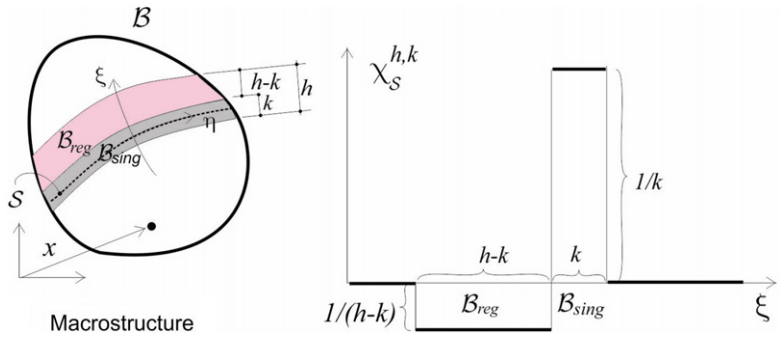

Fig. 25. Regularized dipole function $\chi_{\mathcal{S}}^{h,k}$.

which is sketched, for the 2D case, in Fig. 25. It can be readily checked that $\chi_{\mathcal{S}}^{h,k}(\mathbf{x})$ fulfills Eq. (74) in the limit $h \to 0$, $k \to 0$, so that it can be considered *a regularized sequence converging to the dipole function* in Eq. (74).

A very important property of the regularized dipole function $\chi_{\mathcal{S}}^{h,k}(\mathbf{x})$, to be exploited for subsequent purposes, is (see Fig. 25),

$$\int_{\mathcal{B}} \chi_{\mathcal{S}}^{h,k} d\mathcal{B} = 0. \tag{76}$$

B.1.2. Injection of a constant-stress/discontinuous-strain mode in quadrilateral elements

Let us consider the microscopic instantaneous density of dissipation, $\mathcal{D}_\mu(\mathbf{y}, t)$, at the micro-scale:

$$\mathcal{D}_\mu(\mathbf{y}, t) := \boldsymbol{\sigma}_\mu : \dot{\boldsymbol{\varepsilon}}_\mu - \dot{\psi}_\mu \geq 0 \tag{77}$$

where $\psi_\mu(\mathbf{y}, t)$ stands for the microscopic free energy density of the corresponding constitutive model. From Eq. (77), and taking into account the Hill–Mandel equation (17), the *macroscopic instantaneous density of dissipation*, $\mathcal{D}(\mathbf{x}, t)$, can be written as:

$$\begin{aligned} \mathcal{D}(\mathbf{x}, t) &:= \frac{1}{\Omega_\mu} \int_{\Omega_\mu} \mathcal{D}_\mu(\mathbf{y}, t)\, dV = \boldsymbol{\sigma} : \dot{\boldsymbol{\varepsilon}} - \dot{\psi} \geq 0 \quad \text{(a)} \\ \psi(\mathbf{x}, t) &:= \frac{1}{\Omega_\mu} \int_{\Omega_\mu} \psi_\mu(\mathbf{y}, t)\, dV \qquad\qquad \text{(b)} \end{aligned} \tag{78}$$

where $\psi(\mathbf{x}, t)$ is defined, through Eq. (78)(b), as the averaged (macroscopic) density of free energy, ψ_μ, at the microscale.

Then, considering a finite element discretization of the domain, $\mathcal{B}$, in quadrilateral elements, $\mathcal{B}^{(e)}$; $\mathcal{B} = \bigcup_{e=1}^{e=n_{elem}} \mathcal{B}^{(e)}$, the *injection domain*, $\mathcal{B}_{inj}$, is defined as

$$\mathcal{B}_{inj}(t) := \left\{ \bigcup_e \mathcal{B}^{(e)};\ \mathcal{D}(\mathbf{x}_c^{(e)}, t) > 0 \right\} \tag{79}$$

where $\mathbf{x}_c^{(e)}$ stands for the barycenter of element (e). Eq. (79) defines $\mathcal{B}_{inj}(t)$ as the locus, at time t, of the elements of the macroscale experiencing inelastic behavior at the corresponding microscale level (evaluated at their barycenter $\mathbf{x}_c^{(e)}$). A subset of the injection domain, the *weak discontinuity domain* $\mathcal{B}_{wd}(t)$ is now defined as:

$$\mathcal{B}_{wd}(t) := \left\{ \bigcup_e \mathcal{B}^{(e)};\ \mathcal{B}^{(e)} \subset \mathcal{B}_{inj}(t);\ t \leq t_B(\mathbf{x}_c^{(e)}) \right\}. \tag{80}$$

Eq. (80) characterizes $\mathcal{B}_{wd}(t)$ as the set of elements of the injection domain $\mathcal{B}_{inj}(t)$ whose barycenter has not yet bifurcated, according to the definition of the bifurcation time, t_B, in Eq. (38).

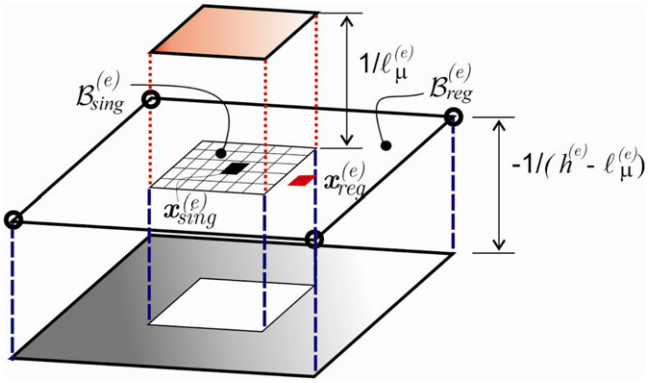

Fig. 26. Injected weak discontinuity mode. Elemental regularized dipole function $\chi_{\mathcal{S}}^{h^{(e)},\ell_{\mu}^{(e)}}$.

The points of $\mathcal{B}_{wd}$ are now endowed a weak discontinuity kinematics, by resorting to the assumed enhanced strain concept [50,51]. The rate of strain, injected in rate form at the typical element, e, with n_{node} nodes, is the following:

$$\dot{\boldsymbol{\varepsilon}}^{(e)}(\mathbf{x},t) \equiv \dot{\boldsymbol{\varepsilon}}_t^{(e)}(\mathbf{x}) = \underbrace{\sum_{i=1}^{i=n_{node}} \boldsymbol{\nabla} \mathrm{N}_i(\mathbf{x}) \otimes \dot{\mathbf{d}}_i(t)}_{(regular)} + \underbrace{\chi_{\mathcal{S}}^{h^{(e)},\ell_{\mu}^{(e)}}(\mathbf{x})\, \dot{\boldsymbol{\gamma}}^{(e)}(t)}_{(singular)} \quad \forall \mathcal{B}^{(e)} \subset \mathcal{B}_{wd}(t) \tag{81}$$

where N_i are the standard shape functions, $\dot{\mathbf{d}}_i(t)$, the nodal displacements, and $\chi_{\mathcal{S}}^{h^{(e)},\ell_{\mu}^{(e)}}$ is the element "e" counterpart of the regularized dipole-function in Eq. (75), for $k \equiv \ell_{\mu}^{(e)} = \ell_{\mu}(\mathbf{x}_c^{(e)})$, fulfilling (see Fig. 26):

$$\chi_{\mathcal{S}}^{h^{(e)},\ell_{\mu}^{(e)}}(\mathbf{x}) = \begin{cases} -\dfrac{1}{h^{(e)} - \ell_{\mu}^{(e)}} & \mathbf{x} \in \mathcal{B}_{reg}^{(e)} \\ \dfrac{1}{\ell_{\mu}^{(e)}} & \mathbf{x} \in \mathcal{B}_{sing}^{(e)} \\ 0 & \text{otherwise} \end{cases} \tag{82}$$

$$h^{(e)} = \frac{\Omega^{(e)}}{L^{(e)}}; \quad \Omega^{(e)} = meas(\mathcal{B}^{(e)}); \quad L^{(e)} = meas(\mathcal{S}^{(e)})$$

where $h^{(e)}$ is a characteristic element width, defined in terms of the measure (area/volume) of the element, $\Omega^{(e)}$, and the measure (length/area), $L^{(e)}$, of the element crack path $\mathcal{S}^{(e)}$. Notice that, by construction, the element dipole function, $\chi_{\mathcal{S}}^{h^{(e)},\ell_{\mu}^{(e)}}$, defined in Eq. (82) fulfills, at element level, the condition in Eq. (76), i.e.:

$$\int_{\mathcal{B}^{(e)}} \chi_{\mathcal{S}}^{h^{(e)},\ell_{\mu}^{(e)}}\, d\mathcal{B} = 0. \tag{83}$$

The second term in Eq. (81) injects, by means of the mode $\chi_{\mathcal{S}}^{h^{(e)},\ell_{\mu}^{(e)}}$, a discontinuous strain field, intensified by the elemental strains $\dot{\boldsymbol{\gamma}}^{(e)}(t)$.

Notice that Eq. (81) can be rewritten as

$$\begin{cases} \dot{\boldsymbol{\varepsilon}}_t^{(e)}(\mathbf{x}) = \underbrace{\sum_{i=1}^{i=n_{node}} \boldsymbol{\nabla} \mathrm{N}_i(\mathbf{x}) \otimes^s \dot{\mathbf{d}}_i(t)}_{(compatible\ strains)} + \underbrace{\dot{\tilde{\boldsymbol{\gamma}}}_t^{(e)}(\mathbf{x})}_{(enhanced\ strains)} \quad \forall \mathcal{B}^{(e)} \subset \mathcal{B}_{wd}(t) \\ \dot{\tilde{\boldsymbol{\gamma}}}_t^{(e)} \equiv \dot{\tilde{\boldsymbol{\gamma}}}^{(e)}(\mathbf{x},t) = \chi_{\mathcal{S}}^{h^{(e)},\ell_{\mu}^{(e)}}(\mathbf{x})\, \dot{\boldsymbol{\gamma}}_t^{(e)} \end{cases} \tag{84}$$

where the enhanced strains, $\dot{\tilde{\boldsymbol{\gamma}}}_t^{(e)}(\mathbf{x})$, fulfill (in view of Eq. (76)) the condition:

Table 3
Sampling values for the regularized dipole function, $\chi_{\mathcal{S}}^{h^{(e)},\ell_\mu^{(e)}}$, Dirac's delta function $\delta_{\mathcal{S}}^{\ell_\mu^{(e)}}$, and integration weights at the injection sampling points (s.p.).

Sampling point	Sampling value ($\chi_{\mathcal{S}}^{h^{(e)},\ell_\mu^{(e)}}$)	Sampling value ($\delta_{\mathcal{S}}^{\ell_\mu^{(e)}}$)	Weight
Regular s.p.: $\mathbf{x}_{reg}^{(e)}$	$\begin{cases} -1/(h^{(e)}-\ell_\mu^{(e)}) \\ h^{(e)} = \dfrac{\Omega^{(e)}}{L^{(e)}} \end{cases}$	0	$\Omega^{(e)} - \ell_\mu^{(e)}\ L^{(e)}$
Singular s.p.: $\mathbf{x}_{sing}^{(e)}$	$1/\ell_\mu^{(e)}$	$1/\ell_\mu^{(e)}$	$\ell_\mu^{(e)}\ L^{(e)}$

$$\int_{\mathcal{B}^{(e)}} \dot{\tilde{\boldsymbol{\gamma}}}_t^{(e)}(\mathbf{x})\, d\mathscr{B} = \mathbf{0} \quad \forall \mathcal{B}^{(e)} \tag{85}$$

this defining a specific class of assumed–enhanced strain elements [50]. Notice also the role of the characteristic length $\ell_\mu^{(e)} \equiv \ell_\mu(\mathbf{x}_c^{(e)})$, imported from the lower scale at the element barycenter, in the definition in (82) and (84), in accordance with Remark 2.4.

A subsequent refinement of the weak discontinuity injection in Eq. (81) consists of the sub-integration, at the element barycenter, of the first term of the right-hand-side of Eqs. (84). This can be interpreted as a *complementary injection of an element-wise constant strain field* for describing the compatible-strain part in Eq. (74). The resulting mixed finite-element problem in Box 3.2 can be solved in closed form, resulting [44]:

$$\begin{aligned}
&\dot{\boldsymbol{\varepsilon}}_t(\mathbf{x}) = \sum_{\forall \mathcal{B}^{(e)} \in \mathcal{B}_{wd}(t)} \phi^{(e)} \Big(\underbrace{\dot{\bar{\boldsymbol{\varepsilon}}}^{(e)}(t)}_{\substack{(regular,\ constant,\\ strains)}} + \underbrace{\dot{\tilde{\boldsymbol{\gamma}}}^{(e)}(\mathbf{x},t)}_{\substack{(singular,\ enhanced\\ strains)}} \Big) \\
&\dot{\bar{\boldsymbol{\varepsilon}}}^{(e)}(t) = \sum_{i=1}^{i=n_{node}} \boldsymbol{\nabla} \mathrm{N}_i(\mathbf{x}_c^e) \otimes^s \dot{\mathbf{d}}_i(t) \\
&\dot{\tilde{\boldsymbol{\gamma}}}^{(e)}(\mathbf{x},t) = \chi_{\mathcal{S}}^{h^{(e)},\ell_\mu^{(e)}}(\mathbf{x})\, \dot{\tilde{\boldsymbol{\gamma}}}_t^{(e)}
\end{aligned} \tag{86}$$

where $\phi^{(e)}(\mathbf{x})$ is the characteristic function of element e ($\phi^{(e)}(\mathbf{x}) = 1\ \forall \mathbf{x} \in \mathcal{B}^{(e)},\ \phi^{(e)}(\mathbf{x},t) = 0\ \forall \mathbf{x} \notin \mathcal{B}^{(e)}$).

It is well known that, for the considered quadrilateral elements, sub-integration of the compatible strains, may translate into violation of the inf–sup conditions [37] and the subsequent appearance of zero-energy modes polluting the solution (hourglass modes). However, it has to be emphasized that, in Eq. (86) *reduced integration is restricted to just a portion of the whole domain* (the weak discontinuity domain $\mathcal{B}_{wd}(t) \subset \mathcal{B}$ defined in Eq. (80)). This fact dramatically changes, in a favorable sense, the stability properties of the resulting formulation. *The possible hourglass modes do not appear whenever a sufficient portion of the domain is fully integrated* [31].

The resulting injection procedure is summarized in Box A1. It provides a finite element formulation, highly sensitive to propagation of localized strain fields. In spite that the actual kinematics of a strong discontinuity, fulfilling Eq. (3), is not included, and, therefore, some degree of stress locking could still appear [52] the resulting element provides reliable information for the crack path field problem in Box 3.1. Therefore, it is used as a first ingredient of the proposed crack-propagation algorithm.

B.1.3. Stress sampling and integration rule

The standard (four) Gauss quadrature rule, corresponding to full integration of two-dimensional quadrilaterals, is complemented with two additional sampling points (placed at the center of the element), see Figs. 26 and 27. They are termed the *singular sampling point*, denoted $\mathbf{x}_{sing}^{(e)}$, and *the regular sampling point*, denoted $\mathbf{x}_{reg}^{(e)}$ and sampling the rest of the element. Entities to be sampled (typically the stresses) are then additionally stored at these additional sampling points as it is done for regular sampling points.

Therefore, for the weak-discontinuity injected element, numerical integration (typically, evaluation of the incremental internal forces in terms of the stresses), is based on those two *injection-sampling points*, by defining the weights indicated in Table 3.

Box A1.
Weak-discontinuity injection variational problem (in rate form)

Problem.

$$
\begin{aligned}
&\textit{GIVEN}:\\
&\hat{\mathcal{V}}_t := \left\{ \boldsymbol{\eta}_t(\mathbf{x}) = \sum_{i=1}^{n_{node}} N_i(\mathbf{x})\boldsymbol{\eta}_i \in [H^1(\mathcal{B})]^{n_{\dim}};\ \boldsymbol{\eta}_t(\mathbf{x})|_{\partial_u\mathcal{B}} = \dot{\mathbf{u}}^*(\mathbf{x},t) \right\}\\
&\hat{\mathcal{V}}_0 := \{\boldsymbol{\eta}(\mathbf{x}) \in H^1(\mathcal{B});\ \boldsymbol{\eta}(\mathbf{x})|_{\partial_u\mathcal{B}} = \mathbf{0}\}\\
&\hat{\mathcal{E}} := \left\{ \delta\boldsymbol{\mu} = \sum_{e=1}^{n_{elem}} \phi^{(e)}(\mathbf{x})\,\delta\boldsymbol{\mu}^{(e)};\ \delta\boldsymbol{\mu}^{(e)} \in \mathbb{S}^{n_{\dim}\times n_{\dim}} \right\}\\
&\tilde{\Gamma} := \left\{ \delta\tilde{\boldsymbol{\gamma}} = \sum_{e=1}^{n_{elem}} \chi_{\mathcal{S}}^{h^{(e)},\ell_\mu^{(e)}}(\mathbf{x})\ \delta\tilde{\boldsymbol{\gamma}}^{(e)};\ \delta\tilde{\boldsymbol{\gamma}}^{(e)} \in \mathbb{S}^{n_{\dim}\times n_{\dim}} \right\}\\
&\textit{FIND}\\
&\dot{\mathbf{u}}_t(\mathbf{x}) \equiv \dot{\mathbf{u}}(\mathbf{x},t) : \mathcal{B}\times[0,T] \to \mathbb{R}^{n_{\dim}};\quad \dot{\mathbf{u}}_t \in \hat{\mathcal{V}}_t\\
&\dot{\bar{\boldsymbol{\varepsilon}}}_t(\mathbf{x}) \equiv \dot{\bar{\boldsymbol{\varepsilon}}}(\mathbf{x},t) : \mathcal{B}\times[0,T] \to \mathbb{S}^{n_{\dim}\times n_{\dim}};\quad \dot{\bar{\boldsymbol{\varepsilon}}}_t \in \hat{\mathcal{E}}\\
&\dot{\tilde{\boldsymbol{\gamma}}}_t(\mathbf{x}) \equiv \dot{\tilde{\boldsymbol{\gamma}}}(\mathbf{x},t) : \mathcal{B}\times[0,T] \to \mathbb{S}^{n_{\dim}\times n_{\dim}};\quad \dot{\tilde{\boldsymbol{\gamma}}}_t \in \tilde{\Gamma}
\end{aligned}
\tag{87}
$$

FULFILLING:

$$
\int_{\mathcal{B}} \boldsymbol{\nabla}^s\boldsymbol{\eta} : \dot{\boldsymbol{\sigma}}_t\, d\mathcal{B} - W^{ext}(\boldsymbol{\eta}, \dot{\mathbf{b}}, \dot{\mathbf{t}}^*) = 0 \quad \forall\boldsymbol{\eta} \in \hat{\mathcal{V}}_0 \tag{a}
$$

$$
\begin{cases}
\displaystyle\int_{\mathcal{B}} \delta\boldsymbol{\mu} : (\dot{\bar{\boldsymbol{\varepsilon}}}_t - \boldsymbol{\nabla}^S\dot{\mathbf{u}}_t(\mathbf{x}))\, d\mathcal{B} = 0 \quad \forall\delta\boldsymbol{\mu} \in \hat{\mathcal{E}}\\
\dot{\boldsymbol{\varepsilon}}_t(\mathbf{x},t) = \dot{\bar{\boldsymbol{\varepsilon}}}_t(\mathbf{x}) + \dot{\tilde{\boldsymbol{\gamma}}}_t(\mathbf{x})\\
\begin{cases}
\dot{\bar{\boldsymbol{\varepsilon}}}_t(\mathbf{x}) = \displaystyle\sum_{e=1}^{n_{elem}} \phi^{(e)}(\mathbf{x})\,\dot{\bar{\boldsymbol{\varepsilon}}}_t^{(e)} \rightarrow \textit{assumed (regular) strain}\\
\dot{\tilde{\boldsymbol{\gamma}}}_t(\mathbf{x}) = \displaystyle\sum_{e=1}^{n_{elem}} \chi_{\mathcal{S}}^{h^{(e)},\ell_\mu^{(e)}}(\mathbf{x})\,\dot{\tilde{\boldsymbol{\gamma}}}_t^{(e)} \in \tilde{\Gamma} \rightarrow \textit{enhanced (singular) strain}
\end{cases}
\end{cases}
\tag{b}
$$

$$
\begin{cases}
\displaystyle\int_{\mathcal{B}} \delta\tilde{\boldsymbol{\gamma}} : \dot{\boldsymbol{\sigma}}_t d\mathcal{B} = \sum_{e=1}^{n_{elem}} \delta\tilde{\boldsymbol{\gamma}}^{(e)} \int_{\mathcal{B}^{(e)}} \chi_{\mathcal{S}}^{h^{(e)},\ell_\mu^{(e)}}(\mathbf{x}) : \dot{\boldsymbol{\sigma}}_t^{(e)} d\mathcal{B}\\
= \displaystyle\sum_{e=1}^{n_{elem}} \int_{\mathcal{S}^{(e)}} \delta\boldsymbol{\gamma}^{(e)} : [\![\dot{\boldsymbol{\sigma}}_t]\!]_{\mathcal{S}^{(e)}}\, d\Gamma = 0 \quad \forall\delta\boldsymbol{\gamma}^{(e)} \in \mathbb{S}^{n_{\dim}\times n_{\dim}}
\end{cases}
\tag{c}
$$

$$
\dot{\boldsymbol{\sigma}}(\mathbf{x},t) \equiv \dot{\boldsymbol{\sigma}}_t(\mathbf{x}) = \dot{\boldsymbol{\Sigma}}(\dot{\boldsymbol{\varepsilon}}_t(\mathbf{x})) \rightarrow \textit{constitutive equation} \tag{d}
$$

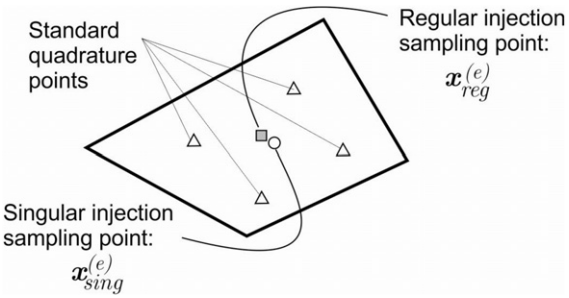

Fig. 27. Sampling points involved in the numerical integration.

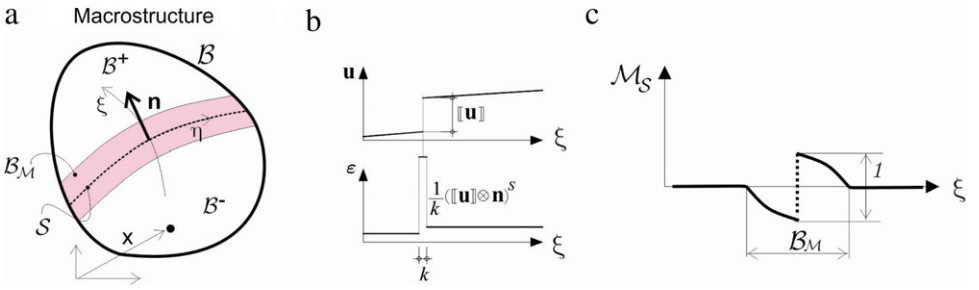

Fig. 28. (a) Body exhibiting a strong discontinuity. (b) Strong discontinuity kinematics (c) Unit jump function.

Replacement of the integration rule, in Table 3, into Eq. (88)(b)–(c) yields the element-wise equation

$$
\begin{aligned}
&\int_{\mathcal{S}^{(e)}} \delta\gamma^{(e)} : [\![\dot{\boldsymbol{\sigma}}_t]\!]^{(e)}\, d\Gamma = 0 \Rightarrow && \text{(a)}\\
&[\![\dot{\boldsymbol{\sigma}}_t]\!]^{(e)} \equiv \dot{\boldsymbol{\sigma}}_t(\mathbf{x}^{(e)}_{\ell_\mu}) - \dot{\boldsymbol{\sigma}}_t(\mathbf{x}^{(e)}_h) = \mathbf{0} \Rightarrow && \text{(b)}\\
&\begin{cases} \dot{\boldsymbol{\Sigma}}_{sing}\left(\dot{\bar{\boldsymbol{\varepsilon}}}^{(e)}_t + \dfrac{\dot{\bar{\gamma}}^{(e)}_t}{\ell^{(e)}_\mu}\right) = \dot{\boldsymbol{\Sigma}}_{reg}\left(\dot{\bar{\boldsymbol{\varepsilon}}}^{(e)}_t - \dfrac{\dot{\bar{\gamma}}^{(e)}_t}{h^{(e)} - \ell^{(e)}_\mu}\right) \\ \dot{\bar{\boldsymbol{\varepsilon}}}^{(e)}_t = \displaystyle\sum_{i=1}^{i=4} \boldsymbol{\nabla}\mathrm{N}_i(\mathbf{x}^e_c) \otimes^s \dot{\mathbf{d}}_i(t) \end{cases} && \text{(c)}
\end{aligned}
\tag{89}
$$

where $\boldsymbol{\Sigma}_{sing}$ and $\boldsymbol{\Sigma}_{reg}$ stand for the stress-evaluation via the continuum constitutive model at the regular and singular sampling points, respectively, as stated by the continuum strong discontinuity approach. Typically, $\boldsymbol{\Sigma}_{sing}$ is made inelastic with strain softening (the softening modulus is regularized with the characteristic length, ℓ_μ), and $\boldsymbol{\Sigma}_{reg}$ is enforced to be instantaneously elastic (for both loading and unloading).

Eq. (89)(b) states that the (incremental) stress field is constant all over the element, in spite of the imposed discontinuous strain field in Fig. 26. In addition, Eq. (89)(c) supplies an elementary-uncoupled additional equation for solving the strain jump, $\dot{\bar{\gamma}}^{(e)}_t$, in terms of the regular elemental strain, $\dot{\bar{\boldsymbol{\varepsilon}}}^{(e)}_t = \sum_{i=1}^{i=4} \boldsymbol{\nabla}\mathrm{N}_i(\mathbf{x}^e_c) \otimes^s \dot{\mathbf{d}}_i(t)$. Therefore, the additional degrees of freedom, $\dot{\bar{\gamma}}^{(e)}_t$, corresponding to the enhanced strain can be condensed at element level following standard procedures [50,53,54].

B.2. Injection of a propagating strong discontinuity

In a second stage, a propagating strong discontinuity is injected in the following domain:

$$
\mathcal{B}_{sd}(t) := \left\{ \bigcup_e \mathcal{B}^{(e)};\ \mathcal{B}^{(e)} \subset \mathcal{B}_{inj}(t);\ t > t_B(\mathbf{x}^{(e)}_c) \right\}. \tag{90}
$$

Comparing Eqs. (90), (79) and (80) one realizes that *the strong discontinuity injection takes place as soon as a weak-discontinuity-injected element bifurcates* according to the problem in Eq. (37). In other words, as soon as the homogenized strain field at the upper scale is compatible with a strong discontinuity kinematics (see Eqs. (37) and (40)).

Let us now consider the continuum body, $\mathcal{B}$, (see Fig. 28(a)) split by the strong discontinuity path $\mathcal{S}$ into two parts, $\mathcal{B}^+$ and $\mathcal{B}^-$. Across $\mathcal{S}$, the rate of displacement field, $\dot{\mathbf{u}}(\mathbf{x})$, experiences a jump $[\![\dot{\mathbf{u}}]\!] = \dot{\mathbf{u}}|_{\mathbf{x}\in(\partial\mathcal{B}^+\cap\mathcal{S})} - \dot{\mathbf{u}}|_{\mathbf{x}\in(\partial\mathcal{B}^-\cap\mathcal{S})}$.

The kinematic description of the displacement field in $\mathcal{B}$, (see Fig. 28(a)) reads:

$$
\dot{\mathbf{u}} = \dot{\bar{\mathbf{u}}} + \mathcal{H}_{\mathcal{S}}\, [\![\dot{\mathbf{u}}]\!] \tag{91}
$$

where $\dot{\bar{\mathbf{u}}}$ stands for the smooth part of the displacement field, $\dot{\boldsymbol{\beta}} \equiv [\![\dot{\mathbf{u}}]\!] = \dot{\mathbf{u}}|_{\mathbf{x}\in(\partial\mathcal{B}^+\cap\mathcal{S})} - \dot{\mathbf{u}}|_{\mathbf{x}\in(\partial\mathcal{B}^-\cap\mathcal{S})}$ stands for the displacement jump and $\mathcal{H}_{\mathcal{S}}$ is the Heaviside (step) function, shifted to $\mathcal{S}$. Due to computational reasons, related to the imposition of the essential boundary conditions, it is convenient to re-formulate Eq. (91) as the following equivalent

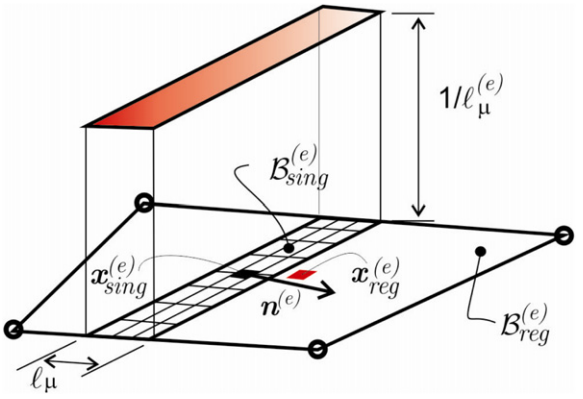

Fig. 29. Injected strong discontinuity mode. Elemental regularized Dirac's delta function $\delta_{\mathcal{S}}^{\ell_\mu^{(e)}}$.

expression, see [36] for further details,

$$\dot{\mathbf{u}} = \underbrace{\dot{\hat{\mathbf{u}}} - \varphi[\![\dot{\mathbf{u}}]\!]}_{\dot{\tilde{\mathbf{u}}}} + \mathcal{H}_{\mathcal{S}}[\![\dot{\mathbf{u}}]\!] = \dot{\hat{\mathbf{u}}} + \underbrace{(\mathcal{H}_{\mathcal{S}} - \varphi)}_{\mathcal{M}_{\mathcal{S}}}\dot{\boldsymbol{\beta}} \tag{92}$$

where $\dot{\hat{\mathbf{u}}}$ fulfills the Dirichlet boundary conditions of the problem, φ is a continuous, in principle arbitrary, function fulfilling:

$$\varphi(\mathbf{x}) = \begin{cases} 0 & \forall \mathbf{x} \in (\mathcal{B} \setminus \mathcal{B}_{\mathcal{M}})^{-} \\ 1 & \forall \mathbf{x} \in (\mathcal{B} \setminus \mathcal{B}_{\mathcal{M}})^{+}. \end{cases} \tag{93}$$

In Eq. (93) $\mathcal{M}_{\mathcal{S}}(\mathbf{x}) = \mathcal{H}_{\mathcal{S}} - \varphi(\mathbf{x})$ is the *unit jump function*, whose support is $\mathcal{B}_{\mathcal{M}}$ and exhibits a unit jump across $\mathcal{S}$, see Fig. 28. In Eq. (93), $\varphi(\mathbf{x})$ is the so-called *indicatrix function* [31]. The (infinitesimal) strain field corresponding to Eq. (92) reads:

$$\dot{\boldsymbol{\varepsilon}} = \boldsymbol{\nabla}^S \dot{\mathbf{u}} = \underbrace{\boldsymbol{\nabla}^S \dot{\hat{\mathbf{u}}} + (\mathcal{M}_{\mathcal{S}} \otimes \boldsymbol{\nabla}\dot{\boldsymbol{\beta}})^S - (\boldsymbol{\nabla}\varphi \otimes \dot{\boldsymbol{\beta}})^S}_{\dot{\hat{\boldsymbol{\varepsilon}}}\ (regular)} + \underbrace{\delta_{\mathcal{S}}(\mathbf{n} \otimes \dot{\boldsymbol{\beta}})^S}_{(singular)} = \dot{\hat{\boldsymbol{\varepsilon}}} + \delta_{\mathcal{S}} \left(\mathbf{n} \otimes \dot{\boldsymbol{\beta}}\right)^S. \tag{94}$$

In the present multiscale context, the proposed injection procedure consists of the incremental injection of *the elemental strong discontinuity mode*,

$$\begin{aligned} \dot{\boldsymbol{\varepsilon}}_t^{(e)} &= \underbrace{\dot{\bar{\boldsymbol{\varepsilon}}}^{(e)}(t)}_{\substack{(regular,\ constant,\\ strains)}} + \underbrace{\dot{\bar{\gamma}}^{(e)}(\mathbf{x}, t)}_{\substack{(singular,\ enhanced\\ strains)}} \quad \forall \mathcal{B}^{(e)} \in \mathcal{B}_{sd}(t) \\ \dot{\bar{\boldsymbol{\varepsilon}}}^{(e)}(t) &= \sum_{i=1}^{i=4} \boldsymbol{\nabla} \mathrm{N}_i(\mathbf{x}_c^e) \otimes^s \dot{\mathbf{d}}_i(t) \\ \dot{\bar{\gamma}}_t^{(e)} &\equiv \dot{\bar{\gamma}}^{(e)}(\mathbf{x}, t) = \delta_{\mathcal{S}}^{\ell_\mu^{(e)}} (\dot{\boldsymbol{\beta}}^{(e)} \otimes^S \mathbf{n}^{(e)})(\mathbf{x}) \end{aligned} \tag{95}$$

in terms of the $\ell_\mu^{(e)}$-regularized Dirac's delta function, $\delta_{\mathcal{S}}^{\ell_\mu^{(e)}}$, displayed in Fig. 29, and Table 3, fulfilling

$$\delta_{\mathcal{S}}^{\ell_\mu^{(e)}} = \begin{cases} \dfrac{1}{\ell_\mu^{(e)}} & \mathbf{x} \in \mathcal{B}_{sing}^{(e)} \\ 0 & \mathbf{x} \in \mathcal{B}_{reg}^{(e)}. \end{cases} \tag{96}$$

Notice the directional, and placement-dependent, character of the injected mode in Eqs. (95)–(96) and Fig. 29, in contrast with the *isotropic* weak-discontinuity mode in Eqs. (86) and Fig. 26. Precise information of this placement, ensuring the spatial continuity of the injected crack-path is a fundamental requirement in the method. The direction

Box A2.
Strong-discontinuity injection variational problem (in rate form)

Problem.

$$
\begin{aligned}
&\textit{GIVEN}:\\
&\hat{\mathcal{V}}_t := \left\{ \boldsymbol{\eta}_t(\mathbf{x}) = \sum_{i=1}^{n_{node}} N_i(\mathbf{x})\, \boldsymbol{\eta}_i \in [H^1(\mathcal{B})]^{n_{\rm dim}};\ \boldsymbol{\eta}_t(\mathbf{x})|_{\partial_u \mathcal{B}} = \dot{\mathbf{u}}^*(\mathbf{x},t) \right\}\\
&\hat{\mathcal{V}}_0 := \{ \boldsymbol{\eta}(\mathbf{x}) \in H^1(\mathcal{B});\ \boldsymbol{\eta}(\mathbf{x})|_{\partial_u \mathcal{B}} = \mathbf{0} \}\\
&\hat{\mathcal{E}} := \left\{ \delta\boldsymbol{\mu} = \sum_{e=1}^{n_{elem}} \phi^{(e)}(\mathbf{x})\, \delta\boldsymbol{\mu}^{(e)};\ \delta\boldsymbol{\mu}^{(e)} \in \mathbb{S}^{n_{\rm dim}\times n_{\rm dim}} \right\}\\
&\tilde{\Gamma} := \left\{ \delta\tilde{\boldsymbol{\gamma}} = \sum_{e=1}^{n_{elem}} \delta_{\mathcal{S}}^{\ell_\mu^{(e)}}(\mathbf{x})\, (\delta\boldsymbol{\beta}^{(e)} \otimes^S \mathbf{n}^{(e)});\ \delta\boldsymbol{\beta}^{(e)} \in \mathbb{R}^{n_{\rm dim}} \right\}\\
&\textit{FIND}\\
&\dot{\mathbf{u}}_t(\mathbf{x}) \equiv \dot{\mathbf{u}}(\mathbf{x},t) : \mathcal{B}\times[0,T] \to \mathbb{R}^{n_{\rm dim}};\quad \dot{\mathbf{u}}_t \in \hat{\mathcal{V}}\\
&\dot{\bar{\boldsymbol{\varepsilon}}}_t(\mathbf{x}) \equiv \dot{\bar{\boldsymbol{\varepsilon}}}(\mathbf{x},t) : \mathcal{B}\times[0,T] \to \mathbb{S}^{n_{\rm dim}\times n_{\rm dim}};\quad \dot{\bar{\boldsymbol{\varepsilon}}}_t \in \hat{\mathcal{E}}\\
&\dot{\boldsymbol{\beta}}_t(\mathbf{x}) \equiv \dot{\boldsymbol{\beta}}(\mathbf{x},t) : \mathcal{B}\times[0,T] \to \mathbb{R}^{n_{\rm dim}};\quad \dot{\boldsymbol{\beta}}_t \in \mathbb{R}^{n_{\rm dim}}
\end{aligned}
\tag{97}
$$

FULFILLING:

$$
\begin{aligned}
&\int_{\mathcal{B}} \boldsymbol{\nabla}^s \boldsymbol{\eta} : \dot{\boldsymbol{\sigma}}_t\, d\mathcal{B} - W^{ext}(\boldsymbol{\eta}, \dot{\mathbf{b}}, \dot{\mathbf{t}}^*) = 0 \quad \forall \boldsymbol{\eta} \in \hat{\mathcal{V}}_0 \qquad \text{(a)}\\
&\begin{cases}
\displaystyle\int_{\mathcal{B}} \delta\boldsymbol{\mu} : [\dot{\bar{\boldsymbol{\varepsilon}}}_t - \nabla^S \dot{\hat{\mathbf{u}}}(\mathbf{x}) - (\nabla\varphi(\mathbf{x}) \otimes^s \dot{\boldsymbol{\beta}}_t(\mathbf{x}))]\, d\mathcal{B} = 0 \quad \forall \delta\boldsymbol{\mu} \in \hat{\mathcal{E}}\\
\dot{\boldsymbol{\varepsilon}}_t(\mathbf{x},t) = \dot{\bar{\boldsymbol{\varepsilon}}}_t(\mathbf{x}) + \dot{\tilde{\boldsymbol{\gamma}}}_t(\mathbf{x})\\
\quad \begin{cases}
\dot{\bar{\boldsymbol{\varepsilon}}}_t(\mathbf{x}) = \displaystyle\sum_{\forall \mathcal{B}^{(e)} \subset \mathcal{B}_{sd}(t)} \phi^{(e)}(\mathbf{x})\, \dot{\bar{\boldsymbol{\varepsilon}}}_t^{(e)} \to \textit{assumed (regular) strain} \qquad \text{(b)}\\
\dot{\tilde{\boldsymbol{\gamma}}}_t(\mathbf{x}) = \displaystyle\sum_{\forall \mathcal{B}^{(e)} \subset \mathcal{B}_{sd}(t)} \delta_{\mathcal{S}}^{\ell_\mu^{(e)}}\, (\dot{\boldsymbol{\beta}}_t^{(e)} \otimes^S \mathbf{n}^{(e)})(\mathbf{x}) \in \tilde{\Gamma} \to \textit{assumed (singular) strain}
\end{cases}
\end{cases}\\
&\begin{cases}
\displaystyle\int_{\mathcal{B}} (\delta\dot{\boldsymbol{\beta}} \otimes^S \mathbf{n}^{(e)}) : \chi_{\mathcal{S}}^{h,\ell_\mu} \dot{\boldsymbol{\sigma}}_t d\mathcal{B} = \sum_{e=1}^{n_{elem}} (\delta\boldsymbol{\beta}^{(e)} \otimes^S \mathbf{n}^{(e)}) : \int_{\mathcal{B}^{(e)}} \chi_{\mathcal{S}}^{h,\ell_\mu^{(e)}}(\mathbf{x}) \dot{\boldsymbol{\sigma}}_t^{(e)} d\mathcal{B}\\
= \displaystyle\sum_{e=1}^{n_{elem}} \int_{\mathcal{S}^{(e)}} \delta\boldsymbol{\beta}^{(e)}\, [\![\dot{\boldsymbol{\sigma}}_t \cdot \mathbf{n}^{(e)}]\!]_{\mathcal{S}^{(e)}}\, d\Gamma = 0 \quad \forall \delta\boldsymbol{\beta}^{(e)} \in \mathbb{R}^{n_{\rm dim}}
\end{cases}\\
&\dot{\boldsymbol{\sigma}}(\mathbf{x},t) \equiv \dot{\boldsymbol{\sigma}}_t(\mathbf{x}) = \dot{\boldsymbol{\Sigma}}(\dot{\boldsymbol{\varepsilon}}_t(\mathbf{x})) \to \textit{constitutive equation}
\end{aligned}
\tag{98}
$$

of the element normal, $\mathbf{n}^{(e)}$, is provided by the solution, $\mathbf{n}$, of the discontinuous bifurcation problem in Eq. (38), evaluated at the center of the element $\mathbf{x}_c^{(e)}$ and at the bifurcation time $t_B(\mathbf{x}_c^{(e)})$. The resulting injection procedure is summarized in Box A2. The integration rule is the one displayed in Table 3 and Fig. 27.

B.3. Space and time integration

As commented above, injection of weak-discontinuity and strong-discontinuity modes, in Sections 1 and 2, requires, in principle, specific integration rules in space, i.e.: a standard four-point Gauss quadrature rule, $\mathbf{x}_i,\ i = (1,2,3,4)$, in $\mathcal{B} \setminus \mathcal{B}_{inj}(t)$, and the two additional sampling/injection points, $\mathbf{x}_{sing}^{(e)}$ and $\mathbf{x}_{reg}^{(e)}$, for injected elements, $\mathcal{B}^{(e)} \subset \mathcal{B}_{wd}(t)$ and $\mathcal{B}^{(e)} \subset \mathcal{B}_{sd}(t)$ so that $\mathcal{B}_{inj} = \mathcal{B}_{wd} \cup \mathcal{B}_{sd}$ (see Table 3, Figs. 25 and 26).

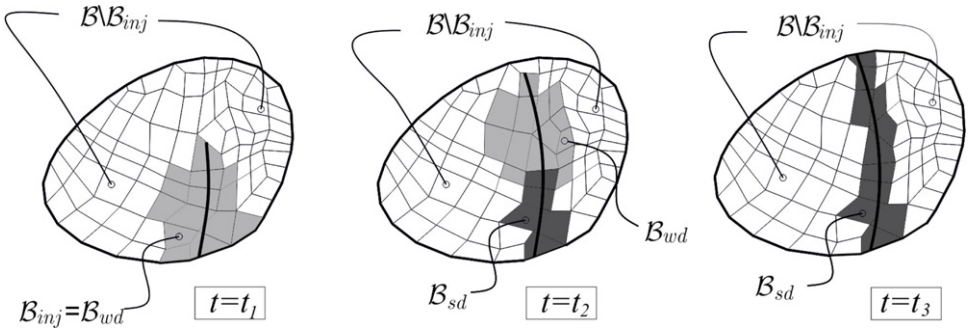

Fig. 30. Evolution of the injection domains for three typical stages of the discontinuity propagation ($t_1 < t_2 < t_3$).

This domain-specific integration rule can become cumbersome in two senses:

(1) Domains $\mathcal{B} \setminus \mathcal{B}_{inj}(t)$, $\mathcal{B}_{wd}(t)$ and $\mathcal{B}_{sd}(t)$ change with time (see Fig. 30). This poses, in principle, some additional problems on the time-integration of the resulting rate of the mechanical balance of forces.

(2) The implementation of those specific integration rules in a standard finite element code becomes code-invasive.

These flaws can be readily overcome by the following procedure. After standard manipulations, the discrete (finite element) version of problem in Eqs. (60)(a), (88)(a) and (98)(a) reads:

$$\begin{aligned}\dot{\boldsymbol{R}}_{mech}(\dot{\mathbf{d}}(t)) = &\int_{\mathcal{B}\backslash\mathcal{B}_{inj}(t)} \mathbf{B}^T(\mathbf{x}) \cdot \{\dot{\boldsymbol{\sigma}}(\mathbf{x}, \dot{\mathbf{d}}(t))\} d\mathcal{B} \\ &+ \int_{\mathcal{B}_{wd}(t)} \mathbf{B}^T(\mathbf{x}) \cdot \{\dot{\boldsymbol{\sigma}}(\mathbf{x}, \dot{\mathbf{d}}(t))\} d\mathcal{B} + \int_{\mathcal{B}_{sd}(t)} \mathbf{B}^T(\mathbf{x}) \cdot \{\dot{\boldsymbol{\sigma}}(\mathbf{x}, \dot{\mathbf{d}}(t))\} d\mathcal{B} - \dot{\mathbf{F}}^{ext}(t) = \mathbf{0}\end{aligned} \tag{99}$$

where, $\boldsymbol{R}_{mech}(\mathbf{d}(t))$ stands for the mechanical residue (unbalanced forces), $\mathbf{d}(t)$ is the vector of nodal displacements, $\mathbf{B}(\mathbf{x})$ stands for the classical deformation matrix, $\{\boldsymbol{\sigma}^h(\mathbf{x}, \mathbf{d}(t))\}$ are the homogenized stresses (in Voigt's notation) computed in accordance with the corresponding strain injections and $\mathbf{F}^{ext}$ are the external forces. Notice that, dependence on time of the integration domains, $\mathcal{B}_{inj}(t)$, $\mathcal{B}_{wd}(t)$ and $\mathcal{B}_{sd}(t)$, in Eq. (99), makes time integration of the residue equation ($\dot{\boldsymbol{R}}(t);\ t \in [0, t_{n+1}] \rightarrow \boldsymbol{R}(t_{n+1}) = \mathbf{0}$) a sensitive issue.

However, this issue can be easily solved by appropriately rephrasing the integral kernels in Eq. (99). In [31] it is proven that, by defining some *specific stress entities* (the so called *effective stresses,* $\tilde{\boldsymbol{\sigma}}(\mathbf{x}_i, t)$) at the standard Gauss points, the spatial integration in Eq. (99) *can be rephrased to* a standard four Gauss points integration rule in *the whole integration domain* $\mathcal{B}$ (and, therefore, not time dependent) i.e.

$$\dot{\boldsymbol{R}}_{mech}(t) \equiv \dot{\boldsymbol{R}}_{mech,t} = \int_{\mathcal{B}} \mathbf{B}^T(\mathbf{x}) \cdot \{\dot{\tilde{\boldsymbol{\sigma}}}(\mathbf{x}, \dot{\mathbf{d}}(t))\} d\mathcal{B} - \dot{\mathbf{F}}^{ext}(t) = \mathbf{0}. \tag{100}$$

Now, Eq. (100) can be exactly integrated[13] along the time interval $[0, t_{n+1}]$ as:

$$\begin{aligned}\boldsymbol{R}_{mech}(\mathbf{d}_{n+1}) &= \int_{\mathcal{B}} \mathbf{B}^T(\mathbf{x}) \cdot \{\tilde{\boldsymbol{\sigma}}_{n+1}(\mathbf{x}, \mathbf{d}_{n+1})\} d\mathcal{B} - \mathbf{F}^{ext}(t) \\ &= \sum_{\forall \mathcal{B}^{(e)} \subset \mathcal{B}} \int_{\mathcal{B}^{(e)}} \mathbf{B}^{(e)^T}(\mathbf{x}) \cdot \{\tilde{\boldsymbol{\sigma}}^{(e)}_{n+1}(\mathbf{x})\} d\mathcal{B} - \mathbf{F}^{ext}_{n+1} = \mathbf{0}\end{aligned} \tag{101}$$

which returns the classical format for the unbalanced residual forces at the current time t_{n+1}. The specific rules for updating the effective stresses, $\tilde{\boldsymbol{\sigma}}^{(e)}_{n+1}$ appearing in Eq. (101), in terms of the homogenized stresses, $\boldsymbol{\sigma}^{(e)}_{n+1}$ at all sampling points, are given in Box A3.

[13] Assuming zero initial balanced forces.

Box A3.
Effective stress evaluation

DATA: $\mu_{n+1}(\mathbf{x})$, $\Delta\hat{\mathbf{u}}_{n+1}(\mathbf{x})$, $\Delta\boldsymbol{\gamma}^{(e)}_{n+1}$, $\Delta\beta^{(e)}_{n+1}$, $\tilde{\boldsymbol{\sigma}}^{(e)}_{n}(\mathbf{x}_i)$, $\boldsymbol{\sigma}^{(e)}_{n}(\mathbf{x}_i)$, $\mathcal{B}_{wd}(t_{n+1})$, $\mathcal{B}_{sd}(t_{n+1})$
OUTPUT: $\tilde{\boldsymbol{\sigma}}^{(e)}_{n+1}(\mathbf{x}_i)$, $\boldsymbol{\sigma}^{(e)}_{n+1}(\mathbf{x}_i)$

(1) *Compute the elemental indicatrix function*:

$$\mu_{n+1}(\mathbf{x}) \rightarrow \varphi^{(e)}_{n+1}(\mathbf{x}) = \sum_{i=1}^{n_{nnode}} N_i(\mathbf{x})\, \varphi^{(e)}_i(\mu_{n+1})$$

(2) *Compute strains*, $\boldsymbol{\varepsilon}^{(e)}_{n+1}$, *at all sampling points*

$$\boldsymbol{\varepsilon}^{(e)}_{n+1}(\mathbf{x}_i) = \boldsymbol{\varepsilon}^{(e)}_{n}(\mathbf{x}_i) + \Delta\boldsymbol{\varepsilon}^{(e)}_{n}(\mathbf{x}_i) \quad \mathbf{x}_i \equiv \mathbf{x}_{G_i}\ (i=1,...,4),\ \mathbf{x}^{(e)}_{reg},\ \mathbf{x}^{(e)}_{sing}$$

$$\Delta\boldsymbol{\varepsilon}^{(e)}_{n+1}(\mathbf{x}^{(e)}_{reg}) = \begin{cases} \nabla^S \Delta\hat{\mathbf{u}}_{n+1}(\mathbf{x}^{(e)}_{reg}) & \mathcal{B}^{(e)} \in \mathcal{B} \setminus (\mathcal{B}_{wd} \cup \mathcal{B}_{sd})(t_{n+1}) \\ \nabla^S \Delta\hat{\mathbf{u}}_{n+1}(\mathbf{x}^{(e)}_{reg}) + \chi^{h^{(e)},\ell^{(e)}_{\mu}}_{\mathcal{S}}(\mathbf{x}^{(e)}_{reg})\, \Delta\boldsymbol{\gamma}^{(e)}_{n+1} & \mathcal{B}^{(e)} \in \mathcal{B}_{wd}(t_{n+1}) \\ \nabla^S \Delta\hat{\mathbf{u}}_{n+1}(\mathbf{x}^{(e)}_{reg}) - (\boldsymbol{\nabla}\varphi^{(e)}_{n+1}(\mathbf{x}^{(e)}_{reg}) \otimes \Delta\boldsymbol{\beta}^{(e)}_{n+1})^S & \mathcal{B}^{(e)} \in \mathcal{B}_{sd}(t_{n+1}) \end{cases}$$

$$\Delta\boldsymbol{\varepsilon}^{(e)}_{n+1}(\mathbf{x}^{(e)}_{sing}) = \begin{cases} \nabla^S \Delta\hat{\mathbf{u}}_{n+1}(\mathbf{x}^{(e)}_{sing}) & \mathcal{B}^{(e)} \in \mathcal{B} \setminus (\mathcal{B}_{wd} \cup \mathcal{B}_{sd})(t_{n+1}) \\ \nabla^S \Delta\hat{\mathbf{u}}_{n+1}(\mathbf{x}^{(e)}_{sing}) + \chi^{h^{(e)},\ell^{(e)}_{\mu}}_{\mathcal{S}}(\mathbf{x}^{(e)}_{sing})\, \Delta\boldsymbol{\gamma}^{(e)}_{n+1} & \mathcal{B}^{(e)} \in \mathcal{B}_{wd}(t_{n+1}) \\ \nabla^S \Delta\hat{\mathbf{u}}_{n+1}(\mathbf{x}^{(e)}_{sing}) + \left[\dfrac{\mathbf{n}^{(e)}}{\ell^{(e)}_{\mu}} - (\boldsymbol{\nabla}\varphi^{(e)}_{n+1}(\mathbf{x}^{(e)}_{sing})\right] \otimes \Delta\boldsymbol{\beta}^{(e)}_{n+1})^S & \mathcal{B}^{(e)} \in \mathcal{B}_{sd}(t_{n+1}) \end{cases}$$

(3) *Compute regular stresses*, $\boldsymbol{\sigma}^{(e)}_{n+1}$, *at all sampling points*

$$\boldsymbol{\sigma}^{(e)}_{n+1}(\mathbf{x}_i) = \boldsymbol{\Sigma}[\boldsymbol{\varepsilon}^{(e)}_{n+1}(\mathbf{x}_i)], \quad \mathbf{x}_i \equiv \mathbf{x}_{G_i}\ (i=1,...,4)$$
$$\boldsymbol{\sigma}^{(e)}_{n+1}(\mathbf{x}^{(e)}_{reg}) = \boldsymbol{\Sigma}_{reg}[\boldsymbol{\varepsilon}^{(e)}_{n+1}(\mathbf{x}^{(e)}_{reg})]$$
$$\boldsymbol{\sigma}^{(e)}_{n+1}(\mathbf{x}^{(e)}_{sing}) = \boldsymbol{\Sigma}_{sing}[\boldsymbol{\varepsilon}^{(e)}_{n+1}(\mathbf{x}^{(e)}_{sing})]$$

(4) *Update effective stresses*, $\tilde{\boldsymbol{\sigma}}^{(e)}_{n+1}$, *at standard (Gauss) sampling points* $\rightarrow \mathbf{x}_i \equiv \mathbf{x}_{G_i}\ (i=1,...,4)$

$$\tilde{\boldsymbol{\sigma}}^{(e)}_{n+1}(\mathbf{x}_i) = \tilde{\boldsymbol{\sigma}}^{(e)}_{n}(\mathbf{x}_i) + \Delta\tilde{\boldsymbol{\sigma}}^{(e)}_{n+1}(\mathbf{x}_i)$$

$$\Delta\tilde{\boldsymbol{\sigma}}^{(e)}_{n+1}(\mathbf{x}_i) = \begin{cases} \boldsymbol{\sigma}^{(e)}_{n+1}(\mathbf{x}_i) - \boldsymbol{\sigma}^{(e)}_{n}(\mathbf{x}_i) & \mathcal{B}^{(e)} \subset \mathcal{B} \setminus (\mathcal{B}_{wd} \cup \mathcal{B}_{sd})(t_{n+1}) \\ \boldsymbol{\sigma}^{(e)}_{n+1}(\mathbf{x}^{(e)}_{reg}) - \boldsymbol{\sigma}^{(e)}_{n}(\mathbf{x}^{(e)}_{reg}) & \mathcal{B}^{(e)} \subset \mathcal{B}_{wd}(t_{n+1}) \\ \begin{cases} \xi[\boldsymbol{\sigma}^{(e)}_{n+1}(\mathbf{x}^{(e)}_{sing}) - \boldsymbol{\sigma}^{(e)}_{n}(\mathbf{x}^{(e)}_{sing})] \\ \quad + (1-\xi)[\boldsymbol{\sigma}^{(e)}_{n+1}(\mathbf{x}^{(e)}_{reg}) - \boldsymbol{\sigma}^{(e)}_{n}(\mathbf{x}^{(e)}_{sing})] \\ \xi = \dfrac{\ell^{(e)}_{\mu}}{h^{(e)}} \end{cases} & \mathcal{B}^{(e)} \subset \mathcal{B}_{sd}(t_{n+1}) \end{cases}$$

B.4. Staggered resolution of the coupled propagation–injection problem

The crack-path-field problem defined in Box 3.1 is stated in terms of $\alpha(\mathbf{x}, t)$ (the localized strain-like internal variable, which depends directly on the solution, nodal displacements, $\mathbf{d}_{n+1}$, of the non-linear mechanical problem in Eq. (101)). On the other hand, this mechanical problem also depends on the crack path, $\mu(\mathbf{x}, t)$, obtained from the crack path field problem in Box 3.1 (see Fig. 31).

Thus, both problems are coupled, and two sets of discretized, in time and space, equations can be written in terms of the corresponding residues:

$$\begin{aligned} &\boldsymbol{R}_{mech}(\mathbf{d}_{n+1}, \boldsymbol{\mu}_{n+1}) = \mathbf{0}, \quad \text{(a)} \\ &\boldsymbol{R}_{prop}(\mathbf{d}_{n+1}, \boldsymbol{\mu}_{n+1}) = \mathbf{0}, \quad \text{(b)} \end{aligned} \tag{102}$$

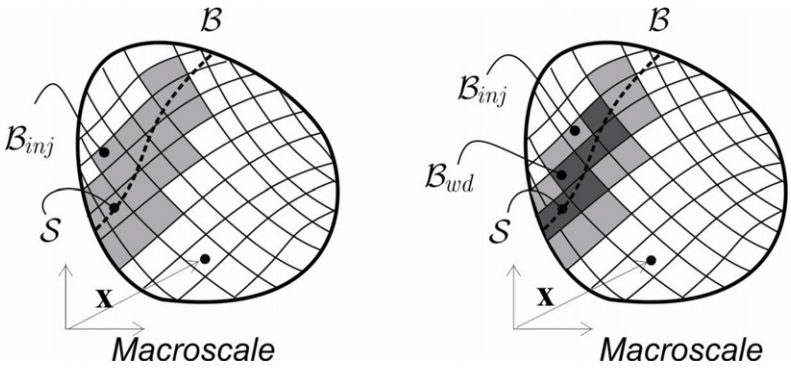

Fig. 31. Coupled propagation (crack-path field) and mechanical (strain injection) problems.

where $\boldsymbol{R}_{prop}$ stands for the residue of the crack propagation problem[14] in Box 3.1 and $\boldsymbol{\mu}_{n+1}$ is the vector of nodal values of the crack-path field $\mu(\mathbf{x}, t_{n+1})$.

As for the strain injection procedure, it can be noticed that, at the initial stages of the non-linear loading process $\mathcal{B}_{inj} = \varnothing$, no discontinuity is injected and, therefore, the problem in Eq. (102) is uncoupled in the sense propagation-problem → mechanical-problem. In this case Eq. (102)(a) can be first directly solved for $\mathbf{d}_{n+1}$ and then, Eq. (102)(b) can be solved for $\boldsymbol{\mu}_{n+1}$:

$$\begin{aligned} &\boldsymbol{R}_{mech}(\mathbf{d}_{n+1}) = \mathbf{0} \rightarrow \mathbf{d}_{n+1} && \text{(a)} \\ &\boldsymbol{R}_{prop}(\mathbf{d}_{n+1}, \boldsymbol{\mu}_{n+1}) = \boldsymbol{R}^{*}_{prop}(\boldsymbol{\mu}_{n+1}) = \mathbf{0} \rightarrow \boldsymbol{\mu}_{n+1}. && \text{(b)} \end{aligned} \tag{103}$$

As soon as at least one element belongs to $\mathcal{B}_{inj}$, the problem becomes coupled in both senses.

However, numerical experience shows that this coupling is weak. In fact, the dependence of the mechanical problem on the variable $\boldsymbol{\mu}_t(\mathbf{x})$ is only through the instantaneous position of the discontinuity path, $\mathcal{S}_t$, to determine the indicatrix function φ and the sets $\mathcal{B}_{inj}$ (see Fig. 31), so that the coupling between $\mathbf{d}_{n+1}$ and $\boldsymbol{\mu}_{n+1}$ in the term $\boldsymbol{R}_{mech}(\mathbf{d}_{n+1}, \boldsymbol{\mu}_{n+1})$ can be considered weak. This suggests the use of a staggered simplified procedure, replacing $\boldsymbol{\mu}_{n+1}$ by $\boldsymbol{\mu}_n$ in Eq. (102)(a), leading to the set of uncoupled equations

$$\begin{aligned} &\boldsymbol{R}_{mech}(\mathbf{d}_{n+1}, \boldsymbol{\mu}_{n}) = \boldsymbol{R}^{*}_{mech}(\mathbf{d}_{n+1}) = \mathbf{0} \rightarrow \mathbf{d}_{n+1} && \text{(a)} \\ &\boldsymbol{R}_{prop}(\mathbf{d}_{n+1}, \boldsymbol{\mu}_{n+1}) = \boldsymbol{R}^{*}_{prop}(\boldsymbol{\mu}_{n+1}) = \mathbf{0} \rightarrow \boldsymbol{\mu}_{n+1}. && \text{(b)} \end{aligned} \tag{104}$$

The staggered resolution of the coupled problem that leads to the uncoupled equations (104) allows envisaging the crack-path-field problem in Box 3.1 as *a post-processing procedure* (typically a double smoothing) of the localizing variable $\alpha_n(\mathbf{x})$ in the mechanical problem. *The crack propagation problem can then be interpreted as a local* (element-wise based) *tracking algorithm that can be straightforwardly, implemented in a finite element code in a non-invasive manner.*

References

[1] R. Hill, Elastic properties of reinforced solids: some theoretical principles, J. Mech. Phys. Solids 11 (5) (1963) 357–372.
[2] P. Germain, The method of virtual power in continuum mechanics. Part 2: Microstructure, SIAM J. Appl. Math. 25 (3) (1973) 556–575.
[3] E. Sanchez-Palencia, Comportements local et macroscopique d'un type de milieux physiques heterogenes, Internat. J. Engrg. Sci. 12 (4) (1974) 331–351.
[4] E. Sanchez-Palencia, Non-Homogeneous Media and Vibration Theory, 1980.
[5] J. Michel, H. Moulinec, et al., Effective properties of composite materials with periodic microstructure: a computational approach, Comput. Methods Appl. Mech. Engrg. 172 (1–4) (1999) 109–143.
[6] S. Nemat-Nasser, Averaging theorems in finite deformation plasticity, Mech. Mater. 31 (8) (1999) 493–523.
[7] K. Terada, M. Hori, et al., Simulation of the multi-scale convergence in computational homogenization approaches, Internat. J. Solids Struct. 37 (16) (2000) 2285–2311.

[14] Which, unlike the mechanical problem, can be proven to be a linear problem.

[8] C. Miehe, Strain-driven homogenization of inelastic microstructures and composites based on an incremental variational formulation, Internat. J. Numer. Methods Engrg. 55 (11) (2002) 1285–1322.
[9] J. Dolbow, M.A. Khaleel, et al. Multiscale mathematics initiative: a roadmap. Pacific Northwest National Laboratory, 2004.
[10] C. Miehe, C. Bayreuther, On multiscale FE analyses of heterogeneous structures: from homogenization to multigrid solvers, Internat. J. Numer. Methods Engrg. 71 (10) (2007) 1135–1180.
[11] F. Vernerey, W.K. Liu, et al., Multi-scale micromorphic theory for hierarchical materials, J. Mech. Phys. Solids 55 (12) (2007) 2603–2651.
[12] Z. Yuan, J. Fish, Towards realization of computational homogenization in practice1, Internat. J. Numer. Methods Engrg. 73 (2008) 361–380.
[13] Y. Efendiev, T.Y. Hou, Multiscale Finite Element Methods: Theory and Applications, Springer Verlag, 2009.
[14] J. Fish, Multiscale Methods: Bridging the Scales in Science and Engineering, Oxford Univ. Pr., 2009.
[15] M.G.D. Geers, V. Kouznetsova, et al., Multi-scale computational homogenization: Trends and challenges, J. Comput. Appl. Math. 234 (7) (2010) 2175–2182.
[16] E.A. de Souza Neto, R.A. Feijóo, Variational foundations of multi-scale constitutive models of solids: small and large strain kinematical formulation. LNCC Research & Development Report 16, 2006.
[17] E.A. de Souza Neto, R.A. Feijoo, On the equivalence between spatial and material volume averaging of stress in large strain multi-scale solid constitutive models, Mech. Mater. 40 (10) (2008) 803–811.
[18] J. Oliver, A.E. Huespe, Theoretical and computational issues in modelling material failure in strong discontinuity scenarios, Comput. Methods Appl. Mech. Engrg. 193 (27–29) (2004) 2987–3014.
[19] I. Gitman, H. Askes, et al., Representative volume: Existence and size determination, Eng. Fract. Mech. 74 (16) (2007) 2518–2534.
[20] Z.P. Bazant, Can multiscale-multiphysics methods predict softening damage and structural failure? Int. J. Multiscale Comput. Eng. 8 (1) (2010) 61–67.
[21] V. Kouznetsova, W. Brekelmans, et al., An approach to micro–macro modeling of heterogeneous materials, Comput. Mech. 27 (1) (2001) 37–48.
[22] V. Kouznetsova, M. Geers, et al., Multi-scale second-order computational homogenization of multi-phase materials: a nested finite element solution strategy, Comput. Methods Appl. Mech. Engrg. 193 (48–51) (2004) 5525–5550.
[23] T. Belytschko, J.H. Song, Coarse-graining of multiscale crack propagation, Internat. J. Numer. Methods Engrg. 81 (5) (2010) 537–563.
[24] V.P. Nguyen, O. Lloberas-Valls, et al., On the existence of representative volumes for softening quasi-brittle materials—a failure zone averaging scheme, Comput. Methods Appl. Mech. Engrg. (2010).
[25] E.W.C. Coenen, V.G. Kouznetsova, et al., A multi-scale approach to bridge microscale damage and macroscale failure: a nested computational homogenization-localization framework, Int. J. Fract. 178 (1–2) (2012) 157–178.
[26] P.J. Sánchez, P.J. Blanco, et al., Failure-oriented multi-scale variational formulation: Micro-structures with nucleation and evolution of softening bands, Comput. Methods Appl. Mech. Engrg. 257 (2013) 221–247.
[27] S. Toro, P.J. Sanchez, et al., A two-scale failure model for heterogeneous materials: numerical implementation based on the finite element method, Internat. J. Numer. Methods Engrg. 97 (5) (2014) 313–351.
[28] J. Oliver, Modelling strong discontinuities in solid mechanics via strain softening constitutive equations. Part 1: Fundamentals, Internat. J. Numer. Methods Engrg. 39 (21) (1996) 3575–3600.
[29] J. Oliver, A.E. Huespe, Continuum approach to material failure in strong discontinuity settings, Comput. Methods Appl. Mech. Engrg. 193 (30–32) (2004) 3195–3220.
[30] J.F. Unger, An FE2-X-1 approach for multiscale localization phenomena, J. Mech. Phys. Solids 61 (4) (2013) 928–948.
[31] J. Oliver, I.F. Dias, et al., Crack-path field and strain-injection techniques in computational modeling of propagating material failure, Comput. Methods Appl. Mech. Engrg. 274 (2014) 289–348.
[32] J. Oliver, A.E. Huespe, et al., Stability and robustness issues in numerical modeling of material failure with the strong discontinuity approach, Comput. Methods Appl. Mech. Engrg. 195 (2006) 7093–7114.
[33] J. Oliver, Continuum modelling of strong discontinuities in solid mechanics using damage models, Comput. Mech. 17 (1–2) (1995) 49–61.
[34] R. Faria, J. Oliver, et al., A strain-based plastic viscous-damage model for massive concrete structures, Internat. J. Solids Struct. 35 (14) (1998) 1533–1558.
[35] J. Oliver, A.E. Huespe, et al., From continuum mechanics to fracture mechanics: The strong discontinuity approach, Eng. Fract. Mech. 69 (2) (2002) 113–136.
[36] J. Oliver, On the discrete constitutive models induced by strong discontinuity kinematics and continuum constitutive equations, Internat. J. Solids Struct. 37 (48–50) (2000) 7207–7229.
[37] O.C. Zienkiewicz, R.L. Taylor, The Finite Element Method. Volumes 1 and 2, McGraw-Hill, 1994.
[38] T. Belytschko, S. Loehnert, et al., Multiscale aggregating discontinuities: a method for circumventing loss of material stability, Internat. J. Numer. Methods Engrg. 73 (6) (2008) 869–894.
[39] I. Stakgold, Green's Functions and Boundary Value Problems, Wiley, New York, 1998.
[40] J.C. Michel, P. Suquet, Nonuniform transformation field analysis, Internat. J. Solids Struct. 40 (25) (2003) 6937–6955.
[41] J.C. Michel, P. Suquet, Computational analysis of nonlinear composite structures using the nonuniform transformation field analysis, Comput. Methods Appl. Mech. Engrg. 193 (48–51) (2004) 5477–5502.
[42] K. Willam, N. Sobh, Bifurcation analysis of tangential material operators, in: G.N. Pande, J. Middleton (Eds.), Transient/Dynamic Analysis and Constitutive Laws for Engineering Materials. Vol. 2, Martinus-Nijhoff Publishers, 1987, pp. 1–13.
[43] N.S. Ottosen, K. Runesson, Properties of discontinuous bifurcation solutions in elasto-plasticity, Internat. J. Solids Struct. 27 (4) (1991) 401–421.
[44] J. Oliver, A.E. Huespe, et al., On the numerical resolution of the discontinuous material bifurcation problem, Internat. J. Numer. Methods Engrg. 83 (6) (2010) 786–804.
[45] P.J. Blanco, P.J. Sánchez, et al., Variational foundations and generalized unified theory of RVE-based multiscale models, Arch. Comput. Methods Eng. (2014) 1–63.

[46] N.B. Nooru-Mohamed, Mixed-mode fracture of concrete: an experimental approach y, Delft University of Technolog, 1992.
[47] E. Roubin, A. Vallade, et al., Multi-scale failure of heterogeneous materials: A double kinematics enhancement for Embedded Finite Element Method, Internat. J. Solids Struct. 52 (0) (2015) 180–196.
[48] C. Oskay, J. Fish, Eigendeformation-based reduced order homogenization for failure analysis of heterogeneous materials, Comput. Methods Appl. Mech. Engrg. 196 (7) (2007) 1216–1243.
[49] J.A. Hernández, J. Oliver, A.E. Huespe, M.A. Caicedo, J.C. Cante, High-performance model reduction techniques in computational multiscale homogenization, Comput. Methods Appl. Mech. Engrg. 276 (2014) 149–189.
[50] J.C. Simo, M.S. Rifai, A class of mixed assumed strain methods and the method of incompatible modes, Internat. J. Numer. Methods Engrg. 29 (8) (1990) 1595–1638.
[51] J. Simo, J. Oliver, A new approach to the analysis and simulation of strong discontinuities. Fracture and Damage in Quasi-brittle Structures, $ &$ FN Spon, 1994.
[52] J. Oliver, A.E. Huespe, et al., Strain localization, strong discontinuities and material fracture: Matches and mismatches, Comput. Methods Appl. Mech. Engrg. 241–244 (2012) 323–336.
[53] J. Oliver, Modelling strong discontinuities in solid mechanics via strain softening constitutive equations. Part 2. Numerical simulation, Internat. J. Numer. Methods Engrg. 39 (21) (1996) 3601–3623.
[54] J.E. Dolbow, A. Devan, Enrichment of enhanced assumed strain approximations for representing strong discontinuities: addressing volumetric incompressibility and the discontinuous patch test, Internat. J. Numer. Methods Engrg. 59 (1) (2004) 47–67.